UNIVERSITÀ
DI PARMA

## DEPARTMENT OF CHEMISTRY, LIFE SCIENCES AND ENVIRONMENTAL SUSTAINABILITY

Doctoral Programme in Material Science and Technology

XXXIII Cycle

# MODELING SUPRAMOLECULAR ELECTROSTATIC INTERACTIONS IN COMPLEX SYSTEMS

Coordinator:
**Prof. Enrico Dalcanale**
Tutor:
**Prof. Anna Painelli**

PhD student:
**Mattia Anzola**

**2017-2020**

# Contents

# Introduction

Every known interaction between objects or particles can be ascribed to one of the so called four fundamental forces: strong, weak, gravitational, and electromagnetic. They are separated according to the average strength of the force, the kind of particles involved in the interactions, and the range of effectiveness. The eletromagnetic force, and specifically electrostatic force in chemistry, represents undoubtedly the most important. Almost the totality of transformations involving atoms and molecules, from the freezing of water to complex energy transfer mechanisms, obey its rules. Electrostatic interactions depend on attractive or repulsive forces between atoms or molecules generated by their electrical charges. This interaction is also known as Coulomb interaction, named after physicist Charles-Augustin de Coulomb, who first characterized it in 1785.[1]. Even though the majority of non-bonded forces are electrostatic, chemists usually discriminate between them on the basis of the types of charges involved. Charged particles are responsible for the strongest non-bonded forces, and include electron-nucleus, ion-ion and ion-dipole interactions. Conversely, weaker electrostatic forces manifest between non-charged objects, such as polar or polarizable molecules, and comprehend, among many others, dipole-dipole interactions, Van der Waals and London dispersion forces.

In this work we will focus on intermolecular interactions that play a major role in the definition of properties in molecular materials. The study of novel molecular materials provides great opportunities to solve a large amount of needs. A careful arrangement of molecules at the nanoscale can lead to the formation of systems with unique optical, electrical and magnetic properties. Molecules arranged in supramolecular aggregates interact through weak non-covalent forces, giving rise to collective electronic states that radically change spectroscopic features of these systems. A large variety of fields exploit this high versatility, from organic solar cell [2, 3, 4] to OLED technology.[5, 6, 7] Another noticeable example that leverages intermolecular electrostatic interactions is made up of the so called light harvesting complexes, acting in the very firsts step of photosynthesis, in which solar light is absorbed and efficiently carried as excitation energy through resonant energy transfer.[8, 9] These systems have been investigated for a long time since their artificial replications find numerous applications as power sources, sensor systems and nanofabricated devices.[10, 11, 12, 13]

Of crucial importance in researching new materials, as well as in developing new features in existing one, is the theoretical modeling of these systems and the rationalization of their spectroscopic properties. Purpose of this thesis is the study and integration of novel methodologies to get a deep understanding of intermolecular electrostatic interactions in complex nanosized systems. In Chapter 1 we investigate Förster RET for a pair of dyes linked to a calixarene scaffold. In systems where the geometry of the chromophore pair is not known a priori, the rate of energy transfer is estimated considering two limiting regimes, static and dynamic, offering an oversimplified view of the mechanism. For this reason, we make extensive use of MD simulations in two different solvents to describe the effect of solvation and conformational motions on the rate of energy transfer. Moreover, we develop a fully dynamical model, based on Monte Carlo method, to analyze the characteristic timescales of such processes and compare them with the experimental picture. Subsequent chapters are all focused on molecular aggregates. In Chapter 2, we examine spectroscopic properties of molecular aggregates, testing new approaches and approximation schemes for polar and non-polar supramolecular assemblies. The first part is focused on the discussion of aggregates of polar and polarizable dyes, improving already existent models to account for vibrational coupling and hence for spectral band-shapes. We then turn attention to aggregates of non-polar chromophores, addressing the reliability of the Heitler-London approximation and presenting a model for two dimensional aggregates. Chapters 3 and 4 are focused on chiral aggregates. In Chapter 3 we investigate aggregates formed by dicyanostilbenes decorated with chiral pendants. Through the use of an hybrid approach, involving MD simulations and exciton modeling, we are able to get a deep understanding on both aggregation and spectroscopic features of these system, questioning the effectiveness of widely adopted rules to assess the system chirality from Circular Dichroism (CD) spectra. In Chapter 4 we focus attention on non-symmetric squaraine aggregates. An extensive theoretical work is discussed, devoted to the study of spectroscopic features of squaraine assemblies in solution. While the possibility of these system to form stable Charge Transfer (CT) states has already been extensively discussed,[14, 15, 16] literature lacks of a methodology able to describe rotatory power induced by CT transitions. We here present a new model for the calculation of absorption and CD spectra of squaraine complexes using a delocalized electrons approach, taking into account for both intra- and intermolecular charge transfer mechanisms.

During my thesis period I spent 3 months at the International Centre for Theoretical Physics in Trieste under the guidance of Dr. Ali Hassanali and 3 months at the Ruđer Bošković Institute in Zagreb under the supervision of Dr. Luca Grisanti where I learnt and mastered all the Molecular Dynamics techniques implemented in this essay.

# Chapter 1

# Resonant Energy Transfer: a dynamical approach

## 1.1 Introduction and plan of the work

Resonant Energy Transfer (RET) is arguably the best known and most widely studied process where energy flows from a molecule, called the energy donor, D, to a nearby molecule, the energy acceptor, A. The process, schematically illustrated in the Jablonsky diagram in Fig. 1.1, is called *resonant* because the excitation of A and deexcitation of D occur simultaneously without energy dissipation. RET is a non-radiative process that competes with other relaxation pathways of the donor, such as radiative or non-radiative decay. When Energy Transfer occurs, D is deexcited while A gets promoted to a resonant excited state, so that, if the acceptor is a fluorescent species, one eventually observes emission from the acceptor while exciting the donor.

$$\begin{aligned} D + h\nu &\rightarrow D^* \\ D^* + A &\xrightarrow{RET} D + A^* \\ A^* &\rightarrow A + h\nu' \end{aligned} \tag{1.1}$$

For this reason, a common approach used to detect RET consists in exciting a sample containing both D and A molecules with radiations of frequencies matching the D absorption spectrum, and detecting light emitted at frequencies matching the A emission spectrum. A different strategy measures the decrease of the fluorescence lifetime of D in the presence of A.

A first model for RET was suggested by Förster[17] in 1948, and is still widely adopted. Specifically, RET occurs between pairs of molecules that are far enough to neglect the overlap between the orbitals on D and A moieties (Dexter energy transfer is negligible) but whose distance is shorter than the wavelength of the photon needed to excite A or deexcite D, so that the radiative energy exchange is irrelevant. In this regime, intermolecular interactions are electrostatic in nature and can be considered as a perturbation on the states of the non-interacting DA system. The Fermi golden rule then gives the RET probability as follows:

$$k_{RET} = \frac{2\pi}{\hbar}|V_{DA}|^2\delta(\omega_D - \omega_A) \tag{1.2}$$

where $V_{DA} = \langle D^*A|H_{int}|DA^*\rangle$ and $\omega_D$ and $\omega_A$ are the frequencies of the $D \to D^*$ and $A \to A^*$ processes. The main merit of Förster theory was to express Eq. 1.2 in term of experimentally accessible data. The first observation is that RET is typically a slow process if compared with internal relaxation that is usually completed in the first few hundreds femtosecond following excitation. So RET occurs from the relaxed D* state, the same state responsible for D fluorescence. Moreover, if intermolecular electrostatic interactions are described in the point dipole approximation, the squared interaction can be written as:

$$|V_{DA}|^2 = |\frac{1}{4\pi\varepsilon_0\eta^2 r^3}[(\vec{\mu}_D \cdot \vec{\mu}_A) - \frac{3}{r^2}(\vec{\mu}_D \cdot \vec{r})(\vec{\mu}_A \cdot \vec{r})]|^2 = \frac{1}{(4\pi\varepsilon_0)^2}\frac{\kappa^2}{\eta^4 r^6}|\mu_D|^2|\mu_A|^2 \tag{1.3}$$

where $\vec{\mu}_{D/A}$ are the transition dipole moments associated with the D fluorescence and A absorption, $\vec{r}$ is the intermolecular distance and $\eta$ is the medium refractive index. In the second equality the squared interaction term is factorized into a term that contains (a) the squared amplitude of the two transition dipole moments, that can be estimated from the integrated intensity of absorption transitions in the isolated D and A molecule, (b) the intermolecular distance that enters at the sixth power in the denominator and (c) a geometrical factor $\kappa^2$ that only depends on the mutual orientation of the two dipoles and ranges from 0 to 0.4. Finally, the Dirac-$\delta$ in Eq. 1.2, ensuring energy conservation,

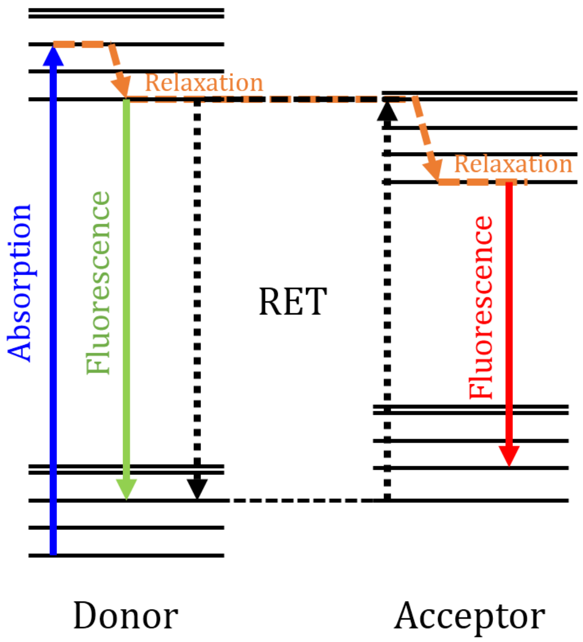

Figure 1.1: Schematic representation of RET mechanism: processes indicated with continuous arrows imply the involvement of a photon; non-radiative processes are depicted with dashed lines: in orange vibrational relaxations and in black the RET mechanism.

can be approximated as the overlap $J$ between the (normalized) fluorescence spectrum of D and the absorption spectrum of A. The final expression for the RET probability then reads:

$$k_{RET} = (\hbar^2 c)^{-1} |V_{DA}|^2 J \tag{1.4}$$

where $J = \int_0^\infty F_D(\tilde{\nu}) A_A(\tilde{\nu}) d\tilde{\nu}$ is the spectral overlap between the donor absorption spectrum and the acceptor emission spectrum, each normalized to unit area, expressed in cm and $c$ is the speed of light in cm$\cdot$s$^{-1}$. The RET velocity in Eq. 1.4 can be translated into a RET-efficiency once the velocities of competing processes are known:

$$\Phi_{RET} = \frac{k_{RET}}{k_{rad}^D + k_{nr}^D + k_{RET}} \tag{1.5}$$

where $k_{rad}^D$ and $k_{nr}^D$ are the probability of D$^*$ radiative and non-radiative decay, respectively. Eq. 1.4 relates the RET rate to the geometry of the RET pair and to experimentally accessible quantities, opening the way to exploit RET as a *molecular ruler*. The price to be paid is the description of intermolecular electrostatic interactions in the point-dipole approximation, a crude approach for large molecules at short distances, as extensively discussed in recent literature [18, 19, 20, 21]. In this respect, more sophisticated approaches have been proposed exploiting transition point-charges,[21] transition cube electron densities[22] or transition density matrices,[23] with further control on the accuracy of $V_{DA}$ depending on the level of theory. [24]. A delicate issue arises in systems where the geometry of the RET pair is not known or not constrained. In these situations $\kappa^2$ is typically averaged assuming an isotropic distribution of D and A orientations. Two estimates of $\kappa^2$ are adopted in the static and dynamic regimes, corresponding to the two limiting cases where the mutual orientation of the pairs has a very slow or very fast dynamics with respect to the intrinsic RET dynamics.[25] However, the factorization of the distance $r$ and of the orientational factor $\kappa^2$ is not always accurate,[26] and, more generally, closed expressions for $\kappa^2$ are not available for systems in constrained geometry. Some of these issues have been dealt with MD, to calculate average $\kappa^2$ values when closed analytical expressions for the orientational averages are not possible [26, 27, 2, 28].

There is also an additional important factor involving the interplay between RET dynamics and the dynamics of the chromophoric units and their environment. Indeed, $V_{DA}$, depending on the intermolecular distance and on the mutual orientation of the two chromophores, is strongly affected by the dynamics of the system, that, depending on specific conditions, may occur on comparable timescales as RET, leading to a complex interplay of different decay pathways.[29, 30, 31] Here, we exploit molecular dynamics (MD) numerical simulations to describe the dynamics of the system at hand. The intermolecular interactions, $V_{DA}$, is calculated in the point dipole approximation, using the transition dipole moments obtained from quantum chemical calculations on the isolated D and A species. Following the MD trajectories, $V_{DA}$ acquires therefore a precise time-dependence that is explicitly accounted for in the calculation of the system dynamics. The dynamical treatment of RET is similar to the approach recently proposed by Hoefling et al. [32, 33], but our study allows to make a direct connection, through MD, between results of quantum chemical calculations and RET dynamics and efficiency for a DA pair in solution.

In spite of a large body of literature, simulating RET is not an easy task, since in experimental systems many factors enter into play, including solvent effects, conformational motion, thermal fluctuations and the competition of all these factors with the intrinsic relaxation dynamics of involved molecules. The aim of this work is to probe slow degrees of freedom, especially connected with molecular motion and thermal fluctuations, that are relevant to RET. For our purpose we selected a bound system, in which the D and A dyes are linked to a common scaffold. Specifically, 4-amino-1-nitrobenzoxadiazole (**NBD**) is our D species and Nile Red (**NR**) the A unit. Both dyes are connected through an amide linker to a calix[4]arene molecule (Fig. 1.2). For this system, a large amount of experimental data collected in different solvents is available.[34] Specifically, the RET dynamics evolves on a wide temporal window ranging from 1 ps to a few ns. Attempts to relate the different timescales to $V_{DA}$ obtained via TD-DFT for different configurations

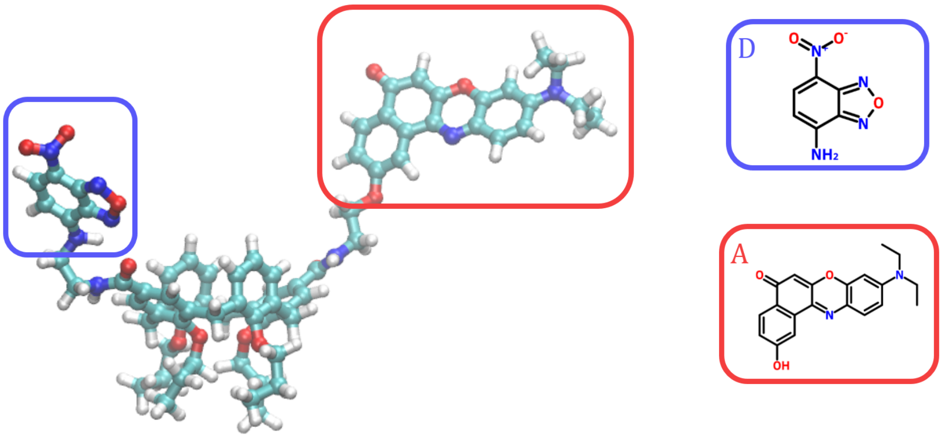

Figure 1.2: Left: ball and stick representation of the system studied; right: isolated Donor and Acceptor.

of the system were unsuccessful, with theoretically estimated timescales ranging from a few tenths to a few hundreds fs.[34] Here, while adopting the same approach to the $V_{DA}$ estimate, we are able to properly simulate RET timescales thanks to our fully dynamical approach to RET. We will demonstrate that the RET process is governed by a complex interplay between different competing dynamical processes that include not just the D radiative and non-radiative relaxation, but also the conformational and solvation degrees of freedom of the system that, modulating $V_{DA}$ on similar timescales as RET, cannot be neglected in the description of this dynamical phenomenon.

We can summarize our roadmap as follows:

- build a computationally reliable dynamical system for the D,A molecules in the presence of the calixarene (clx) scaffold
- develop a fully dynamical model for the energy transfer process and how this compare with experimental picture
- analyze the characteristics timescales for such processes to understand the role of different physical components

## 1.2 Force Field validation

Because of the complexity of the system, we decided to study first the two free dyes in water (a very well studied solvent for MD). Then we proceeded according to the following scheme:

**(DA-c)** *D* and *A* unbound pair in chloroform

**(clx-DA-c)** *D* and *A* connected to calix-[4]-arene in chloroform

**(clx-DA-d)** *D* and *A* connected to calix-[4]-arene in DMSO

A reliable computational model of the above systems can be built by taking advantage of MD. In a MD simulations, atoms mutually interact, accounting for attractive and repulsive forces as well as for chemical bonds constraints, generating a potential field.

The numerical solution of the Newton's equations of motion generates a trajectory, showing the dynamic evolution of the system. See Appendix B for more details.

The first step in any MD investigation is the definition of an optimal Force Field (FF) for the system at hand. Typically, non-biological organic molecules of moderate size are modelled using force fields that includes all atoms and describe their interactions, starting from ab-initio optimized geometries. Commonly adopted FF are GROMOS, CHARMM and GAFF. GAFF will prove the most appropriate choice for our system. A specific requirement for our work is a good representation of the donor dye both in the ground state, $D$ and in the relaxed excited state $D^*$. Different charge distributions for the same molecule in the two different states can be readily converted into GAFF topologies, enabling a fine tuning of parameters.

### 1.2.1 NBD

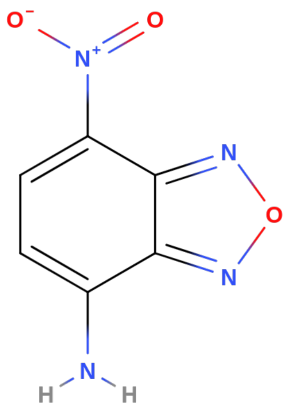

Figure 1.3: 4-amino-1-nitrobenzoxadiazole, NBD

The donor molecule of our system, NBD, is a small molecule with a fairly rigid structure. However, some geometrical parameters must be monitored to ensure a realistic behaviour during simulations. We specifically investigate the geometry of *amino* and *nitro* groups. After topology files were created for each FF, three different simulations at constant number of molecules, volute and temperature (NVT ensamble, see Appendix B) simulations were performed in a $5 \times 5 \times 5\ nm^3$ water box. To test the goodness of the topology the Radial Distribution Function (RDF) of water oxygens around the nitro and amine nitrogen atoms is calculated (Fig. 1.4). RDF describes how the density of surrounding atoms varies as a function of distance from a point. It is usually determined as the number of atoms A (in our case water oxygens) at a distance $r$ from a given atom B (nitro and amino nitrogen), normalized for the density of A atoms in the system:

$$g_{AB}(r) = \frac{1}{\rho(A)} \langle \sum_{A} \delta(\vec{r}_A - \vec{r}_B) \rangle \tag{1.6}$$

RDF results for GROMOS differ from those obtained by other FFs, giving an incorrect distribution of water oxygens around the amino nitrogen, while CHARMM and GAFF results are comparable (Fig. 1.4).

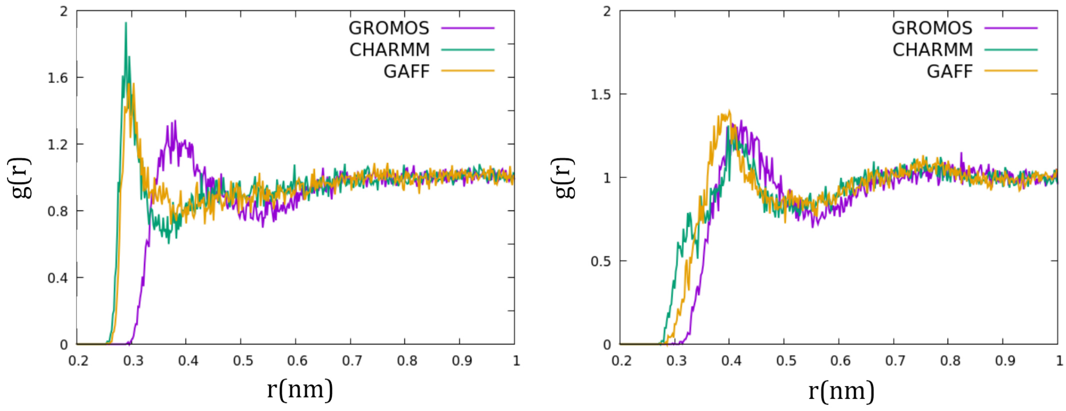

Figure 1.4: Left: radial distribution function of water oxygens around amino N; right: radial distribution function of water oxygens around nitro N.

We modified some parameters in GAFF topology file of the NBD molecule in order to improve the consistency of results obtained with different force fields. We expect the dyhedral angle distribution of both the nitro and amino groups to be peaked at 0°, since

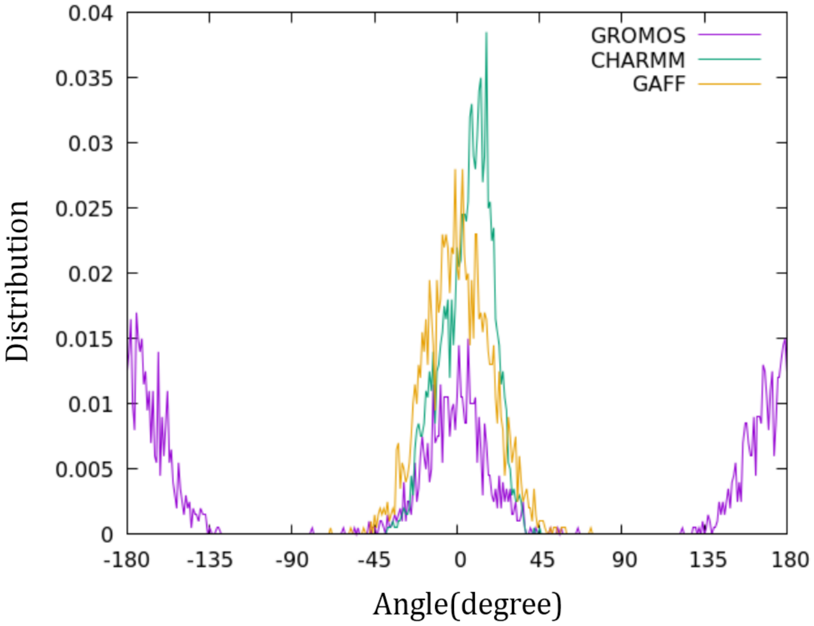

Figure 1.5: H-N-C-C dihedral angle distribution for different FFs.

the strong donor/acceptor character of the $NH_2/NO_2$ groups ensures conjugation and hence planarity. While the H-N-C-C dihedral (shown in Fig. 1.5) already satisfies our predictions, the O-N-C-C dihedral distribution presents a minimum at 0° (Fig. 1.6 left). For this reason we increased the relevant force constant, from 2.51 to 4.4 $Kcal{\cdot}mol^{-1}{\cdot}\AA^{-2}$ (i.e. setting it to the same value as for the H-N-C-C force constant). The resulting distribution obtained properly peaks at 0°, as shown in the right side of Fig. 1.6.

### 1.2.2 NR

For NR we run analogous simulations as described for NBD. As shown in the left panel of Fig. 1.8, the magnitude of the dipole moment shows different time profiles depending on the adopted FF. A correlation is observed between the oscillations of the dipole magnitude and the orientation of the methoxy group (see Fig. 1.8). In GROMOS, where the methoxy group is confined in the $[-45°, 45°]$ region, dipole module is fixed around

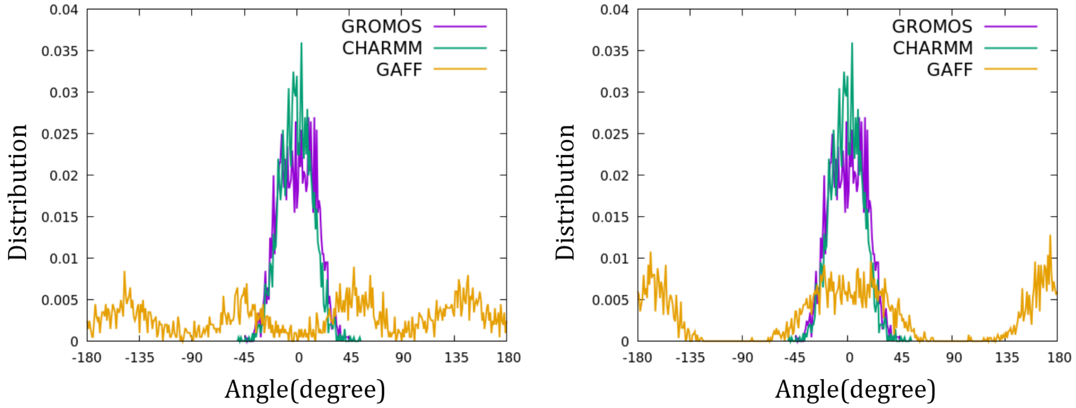

Figure 1.6: Distribution of dihedral angle O-N-C-C in different Force Fields. Left: before correction; right: after correction.

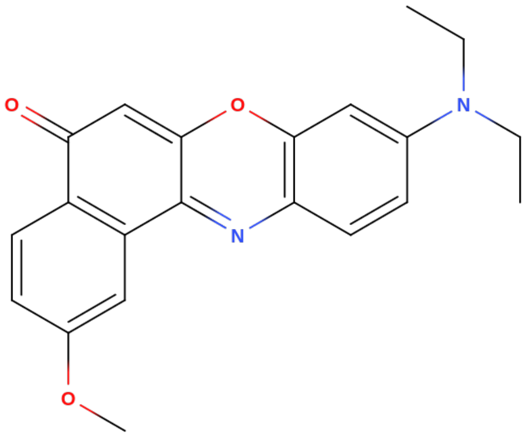

Figure 1.7: methoxy-Nile Red, NR

6.7 D, while it strongly oscillates when the methoxy group can interchange between "open" and "closed" conformations (defined respectively as conformations where the $O-CH_3$ group is in "cis" or "trans" configuration with respect to the carbonyl group). We performed two different Quantum Mechanical (QM) calculation (b3lyp/6-31g(d,p), frozen geometry) on the "closed" and "open" conformation of the methoxy group to

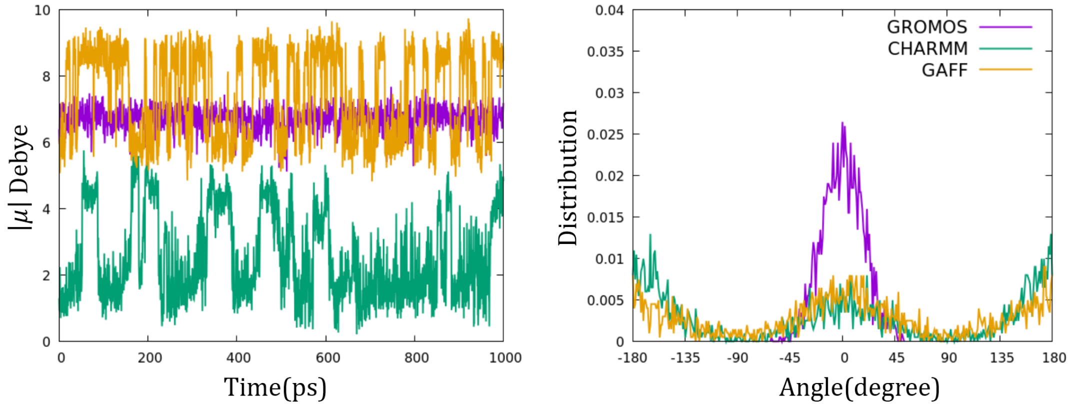

Figure 1.8: Left: NR dipole moment magnitude as a function of time. Right: methoxy group dihedral distribution.

assess the magnitude of the electric dipole in the two conformers. We obtain 6.2899 $D$ in the closed confirmation and 7.8773 $D$ in the open conformation, in good agreement with MD results. The good agreement with DFT supported our choice of GAFF as the reference force field, with the minor correction of the force constant relevant to the OMe group that we set to 9.17 $kJmol^{-1}nm^{-2}$, to be compared with the orginal value 3.77. With this new constraint the methoxy group is still able to rotate but the distribution is more pronounced in the 0° and 180° region (Fig. 1.9), consistently with chemical intuition.

### 1.2.3 Parametrization of the excited state FF: QM calculations

For the D molecule we need also a FF for the excited D* state. Working with excited states in classical molecular dynamics would in principle require a full reparametrization of the FF. This is a non-trivial task and definitely beyond the scope of our work. Therefore we adopted an empirical approach using the same GAFF parametrization defined for the ground state, but replacing the ground state equilibrium geometry and charge distribution with those relative to the Kasha state (the lowest vibrationally relaxed excited state). Indeed very minor conformational changes, are observed, as expected for

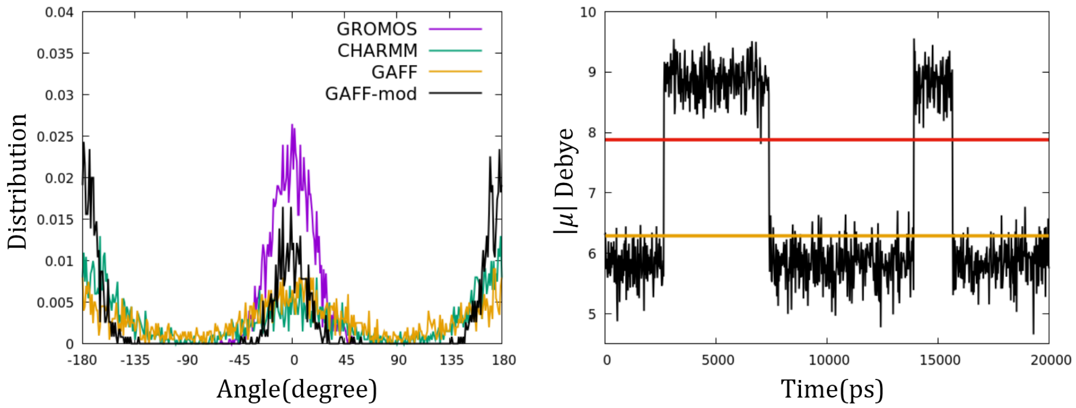

Figure 1.9: Left: comparison between methoxy dihedral distribution in modified-GAFF with FFs in Fig. 1.8; right: dipole magnitude oscillation of the modified GAFF force field compared with “closed” (orange) and “open” (red) conformation dipole magnitude as obtained from DFT calculations.

NBD, a planar and rigid molecule.

For excited state calculations we tested few levels of theory. We used standard HF as well as TD-DFT with two different functionals, with 6-31G(d,p) basis set. Calculations were run both in vacuum (**vac**) and in chloroform (**clf**, PCM). Table 1.1 show relevant results.

The diagram in Fig.1.10 schematizes the process to extract the proper topology from the result of the ab-initio calculation. Molecular dynamics simulations address slow

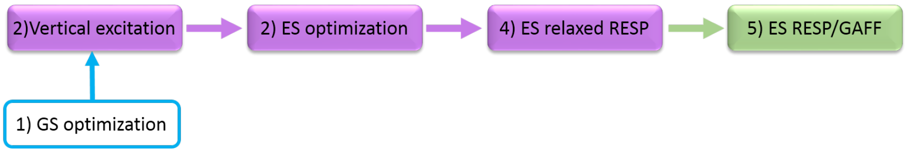

Figure 1.10: Calculation performed to obtain excited state charges on isolated chromophores

| **NBD** | CIS-HF<br>clf (vac) | B3LYP<br>clf (vac) | CAM-B3LYP<br>clf (vac) | Exp. |
|---|---|---|---|---|
| Trans. En. (Abs)$^{a}$ | 4.11 (4.35) | 3.14 (3.32) | 3.39 (3.60) | 2.73 |
| $\mu_t$ (Abs) | 5.978 (4.272) | 3.964(2.222) | 4.894 (2.885) | |
| Trans. En. (Emi) | 3.70 (3.96) | 2.56 (2.75) | 2.91 (3.12) | 2.38 |
| $\mu_t$ (Emi) | 5.972 (4.186) | 2.682 (1.501) | 4.289 (2.401) | |

Table 1.1: Calculated absorption and emission energies (eV) and transition dipole moments (atomic units, a.u.) relevant to the lowest excited state NBD. Last column shows experimental transition energies from Ref. [34].

degrees of freedom, such as conformational changes and diffusion within the solvent, much slower than molecular electronic and vibrational degrees of freedom. Therefore the excitation is simulated by simply switching the molecular topology file from the one relevant to the ground state to that relevant to the relaxed excited state. As shown in the diagram above, we start from the optimized ground state, focus on the first excited state, relax its geometry, calculate restrained electrostatic potentials (RESP charges) and finally transfer this information to GAFF topology.

Since best results for ground state calculations were obtained with B3LYP functional in vacuum, the same functional is adopted in steps 2 and 3. For step 4 instead, we adopted the HF-CIS functional, the one most suitable with RESP charges. The basis set is maintained as 6-31 G(d,p) in all calculations. Table 1.2 report the difference between ground and excited state electric dipole (both in magnitude $\Delta|\mu|$ and orientation $\theta_\mu$), calculated for different levels of theory. Along with them, we listed the variation in charge upon excitation for a few atoms.

| **NBD** | |
|---|---|
| $\Delta\|\mu\|$ D | 1.15 |
| $\theta_\mu$ deg. | 12.65 |
| $O-NO$ $\Delta q$ | 0.031 |
| $NO_2$ $\Delta q$ | -0.074 |
| $NH_2$ $\Delta q$ | 0.053 |

Table 1.2: Ground and excited state RESP charge distribution. Magnitude and orientation changes in electric dipole moment are shown along with charge differences for most relevant atoms.

## 1.3 Molecular Dynamics simulations

### 1.3.1 The free DA pair in chloroform

As a first step, we address MD simulations of the unbound DA pair in chloroform. We focus on two different systems:

- $D-A$
- $D^*-A$

We first generated a $5 \times 5 \times 5$ $nm^3$ chloroform box with the two dyes randomly placed in it. We then proceeded with a 1 ns simulation at fixed molecule number, pressure and temperature (NPT simulation), followed by a preliminary NVT run of 10 ns and a final NVT run of 100 ns. The Potential of Mean Force (PMF) curve is defined as the free energy surface along a chosen coordinate. Specifically, PMF $\mathcal{P}$, along a generic coordinate $\xi$, can be defined as[35]:

$$\mathcal{P}(\xi) = \mathcal{P}(\xi_0) - RTln\frac{D(\xi)}{D(\xi_0)} \tag{1.7}$$

where $R$ is the universal gas constant , $T$ the temperature $\xi_0$ is an arbitrary reference point. The function $D(\xi)$, the distribution function along the coordinate $\xi$, is obtained directly from the MD trajectory.

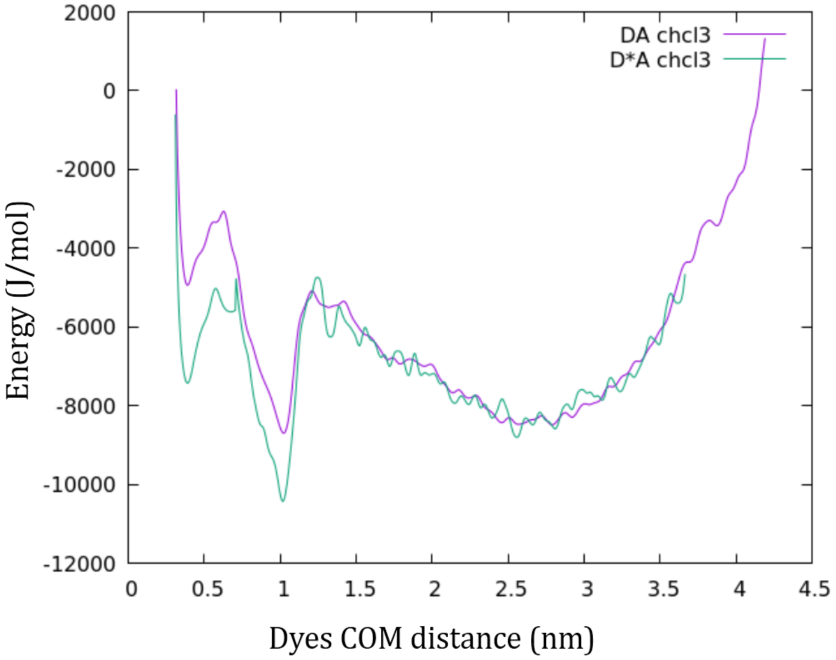

Figure 1.11: PMF extracted from a 100 ns NVT simulation in chloroform for DA, D*A and DA*.

PMFs shown in Fig. 1.11 (and all the others) were elaborated from the distributions $D(d)$ of the distance ($d$) between the D and A center of mass (COM), calculated over long dynamical runs (at least 100 ns, see Appendix B for further details). The PMF profiles in Fig. 1.11 show a very broad minimum at 2.58 nm, which is however an artifact due to periodic boundary conditions (the box dimension is 5.16 nm). The peak at 0.39 nm corresponds instead to a $\pi - \pi$ configuration (Fig. 1.12 left). A second peak at 1 nm acorresponds (Fig. 1.12 right) to a configuration characterized by a strong H-bond between the amino hydrogen of NBD with the quinonoid oxygen of NR.

### Umbrella Sampling

For our purpose, since RET is strongly affected by the D-A distance, we must ensure that all possible distances are properly sampled. Therefore the PMF curve obtained

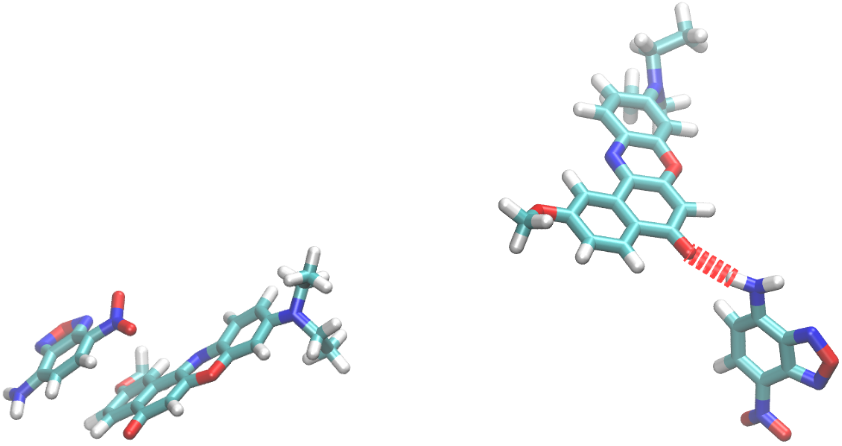

Figure 1.12: Structures corresponding to the 2 minima in the PMF curves in Fig. 1.11. Left panel: $\pi - \pi$ stacking; right panel: H-bond

from Eq. 1.7 is compared with results obtained with umbrella sampling (see Appendix B) to confirm converged results.

To properly use US, the narrowest minimum in the PMF is searched and fitted with a quadratic curve, in order to roughly estimate the largest force constant. At this point a larger force constant is introduced. Setting the equilibrium position of that force at different values of the target coordinate, the system is forced to explore the whole configuration space (with reference to the relevant coordinate). The force used for this purpose is $K_{US} = 1800.00\frac{KJ}{mol}$. Results from US simulations in chloroform, reported in Fig. 1.13, confirm the presence of two main peaks at 0.39 and 1 nm. The difference in the relative height of the peaks lies in the change in charge distribution, that affects the H-bond strength. Furthermore, we proved the artificial nature of the broad peak, that is completely absent in US simulations.

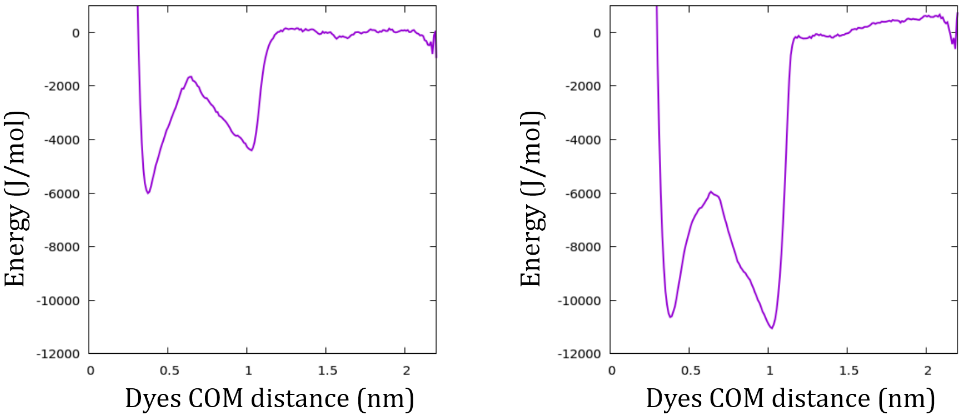

Figure 1.13: PMF calculated with Umbrella Sampling simulations in chloroform. Left: DA, right: D*A.

### 1.3.2 The bound DA pair in chloroform

We use the same protocol as in the previous section to set up a long MD simulation of clx-DA and clx-D*A systems in chloroform. The relevant PMFs are shown in Fig. 1.14. The conformational space available to the two dyes is much reduced with respect to the unbound DA pair discussed above. Therefore the scan of the configurational space is fast and there is no need to implement enhanced sampling techniques. PMF curves for clx-DA an clx-DA* both show three minima. The first minimum corresponds to a $\pi - \pi$ arrangement of the two dyes. The second and third minima can be both attributed to a strong H-bond between the $N - H$ group of the NBD residue and the amidic $C = O$ of the NR linker. While those two complementary groups interact, the bulky chromophore can lie on the same side of the donor, or in opposite direction, shaping the PMF into two well-distinct potential wells.

### 1.3.3 The bound DA pair in DMSO

The same computational approach described above for the clx-DA dynamics in chloroform was also adopted for simulations in DMSO. The calculated PMF curves, in Fig.

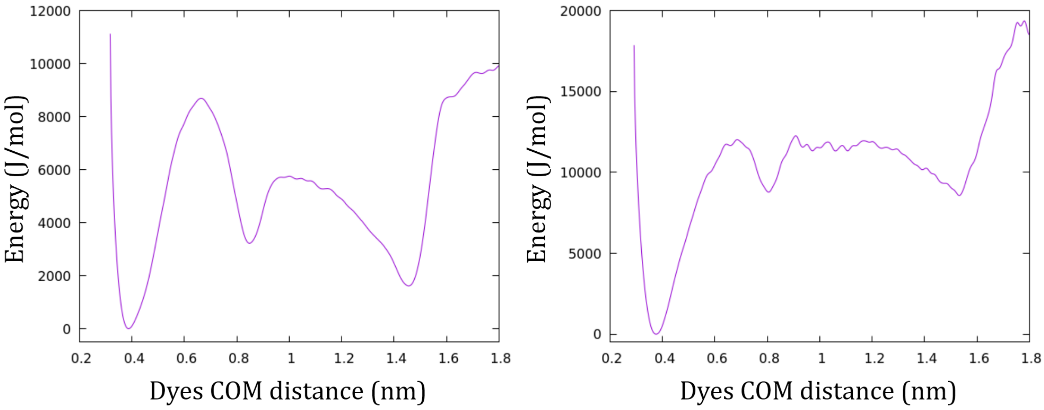

Figure 1.14: PMF curve for NVT simulation in chloroform of clx-DA (left), clx-D*A (right).

1.15, show the presence of a narrow minimum in the $\pi - \pi$ stacking region. Interestingly, we note that, instead of the two distinct minima observed in chloroform, in DMSO a broad plateau is found in the 1.2-2.2 nm region. This pronounced difference in PMF curve is ascribed to the strong H-bond formed between the carbonyl group in the solvent (a strong H-bond acceptor) and the amide hydrogens of the chromophores linkers (Fig. 1.16).

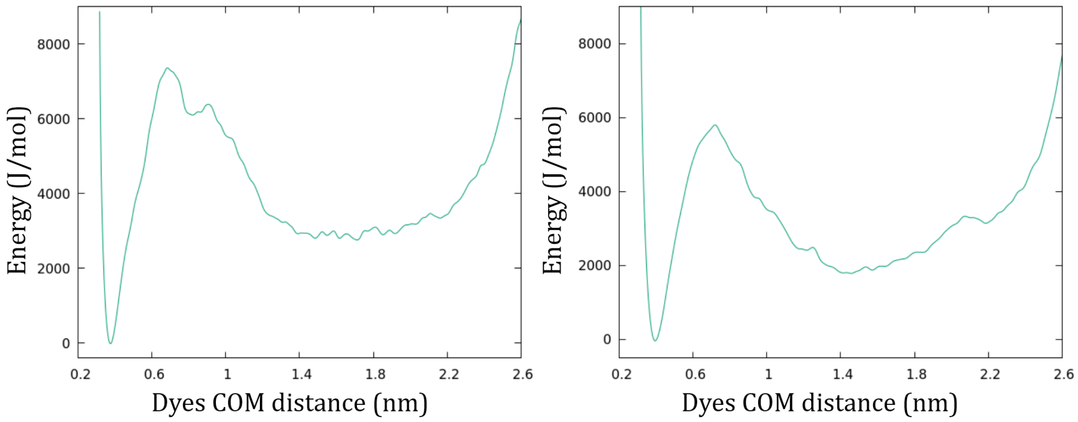

Figure 1.15: PMF curve for NVT simulation in DMSO of the systems clx-DA (left), clx-D*A (right).

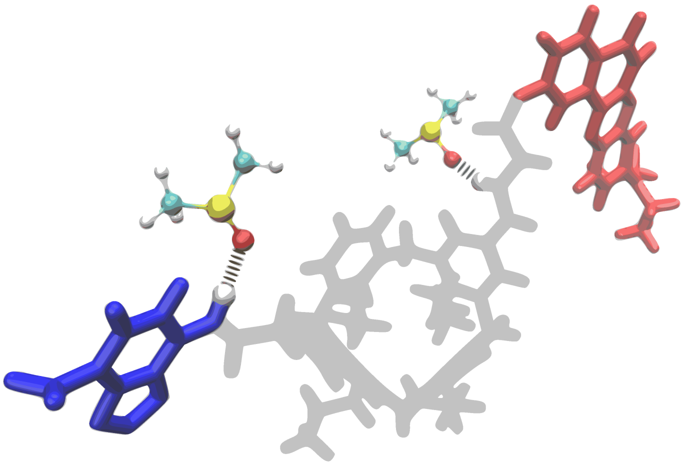

Figure 1.16: Strong *solvent-linker* H-bond in DMSO stabilizing “open” calixarene conformation.

### 1.3.4 Conformational Analysis

To better characterize the system and better understand the interactions occurring during the simulation we investigate different geometrical parameters. Since $k_{RET}$ depends largely on distance between dyes and their mutual orientation, we focus on the distance between the COM of the two dyes, $d$ and on the two angles (shown in Fig. 1.17):

1. $\theta_\mu$, the angle between permanent dipole moments of the two dyes
2. $\theta_\pi$, the angle between the vectors normal to chromophore planes

For comparison purposes Fig. 1.18 shows bidimensional histograms calculated for the the unbound DA pair in chloroform. The histograms point to the presence of a $\pi - \pi$ stacking, with the peak at 0.39 nm. Two additional high density regions are also observed. The first one, fairly sharp, shows a little correlation in the $\theta_\mu$ over distance panel, and is ascribed to the H-bond conformation, in which molecules are held together at a distance of approximately 1 nm without loosing conformational freedom. A third fairly broad region accounts for the dyes freely diffusing in the solvent (the gradient in the distribution, that would have a maximum at 2.58 nm, is an artifact of the finite box size). Results for the calix-bound DA pair show a much limited freedom. In chloroform (Fig. 1.19) the three characteristic minima seen in the PMF curve (Fig. 1.14), are recognized as three peaks in the histograms. The peak at 0.4 nm corresponding to the $\pi - \pi$ aggregation, besides the trivial relation with the $\theta_\pi$ parameter, shows a correlation also with $\theta_\mu$, due to the presence of amidic linkers that limit the dyes motion. The region between 0-7-0.9 nm shows a similar, but less constrictive, correlation: the two chromophoric groups are held close by *linker-linker* and *dye-linker* H-bond interactions. The last region, corresponding to the broad peak in the PMF, indicates a complete loss of correlation: the two dyes are too far away to interact with each other. Results in DMSO reveal more complex relations. The minimum corresponding to the $\pi - \pi$ stacking conformation shows a less constrained orientation of the two chromophore, a behaviour that is also observed for other long-distance arrangements. The analysis confirms again the presence of a $solvent - linker$ H-bond, which competes with intramolecular interactions, loosening their strength. A snapshot from the clx-DA dynamics in DMSO is shown in Fig. 1.16, where the two most notable H-bond interactions are highlighted.

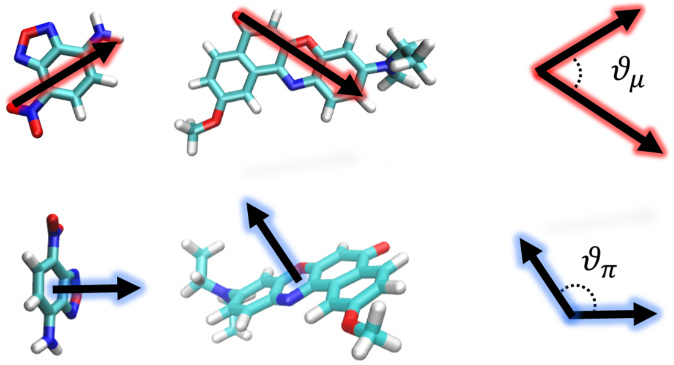

Figure 1.17: Graphical representation of $\theta_\mu$ and $\theta_\pi$

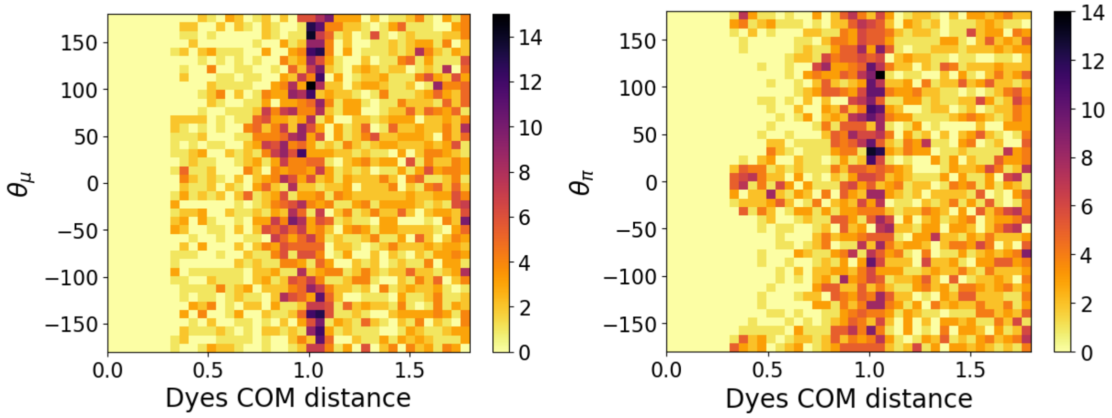

Figure 1.18: Bidimensional histograms of $\theta_\mu$ (left) and $\theta_\pi$ (right) over chromophore center of mass distance for the DA system in chloroform.

### 1.3.5 Charateristics timescales

The time autocorrelation function is a representation of the degree of similarity between a time series and a lagged version of itself. It is mainly used to find patterns of a given variable. The definition of autocorrelation function $AC_f$ for a generic function $f(t)$ is:

$$AC_f(t) = \langle f(\xi) f(\xi + t) \rangle_\xi \tag{1.8}$$

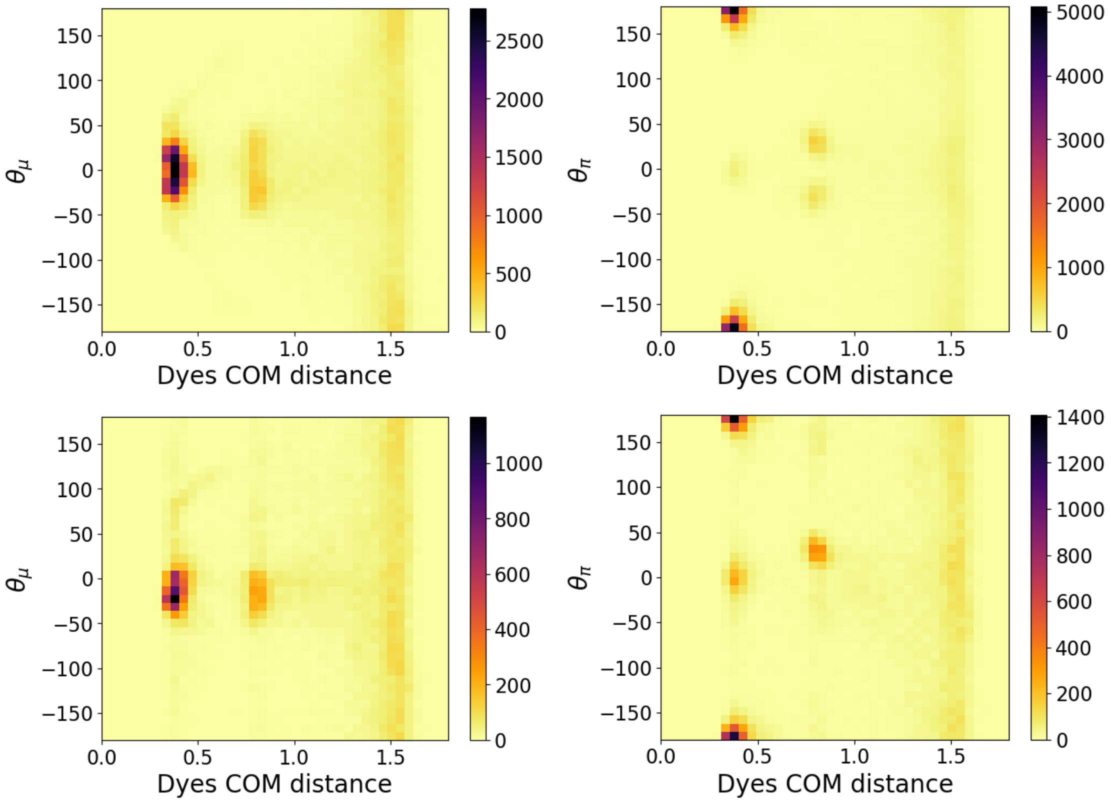

Figure 1.19: Bidimensional histograms of $\theta_\mu$ (left) and $\theta_\pi$ (right) over chromophore center of mass distance in **chloroform**. Top: results for clx-DA. Bottom: results for clx-D*A.

where $\langle ... \rangle_\xi$ indicates the integral over time on the entire dynamics. Since in MD simulations we only have access to discrete data points separated by time intervals $\Delta t$, the integration is substituted by a sum as follows:

$$AC_f(j\Delta t) = \frac{1}{N-j} \sum_{i=0}^{N-1-j} f(i\Delta t) f((i+j)\Delta t)$$

where $i$ and $j$ run over all $N$ frames of the simulations. The variables of interest are the distance, the angle bewteen the vectors normal to the molecular planes and the angle between permanent dipoles ($d$,$\theta_\pi$ and $\theta_\mu$), as defined previously. For each degree of freedom, an autocorrelation curve is calculated and then each $AC(t)$ is fitted with a

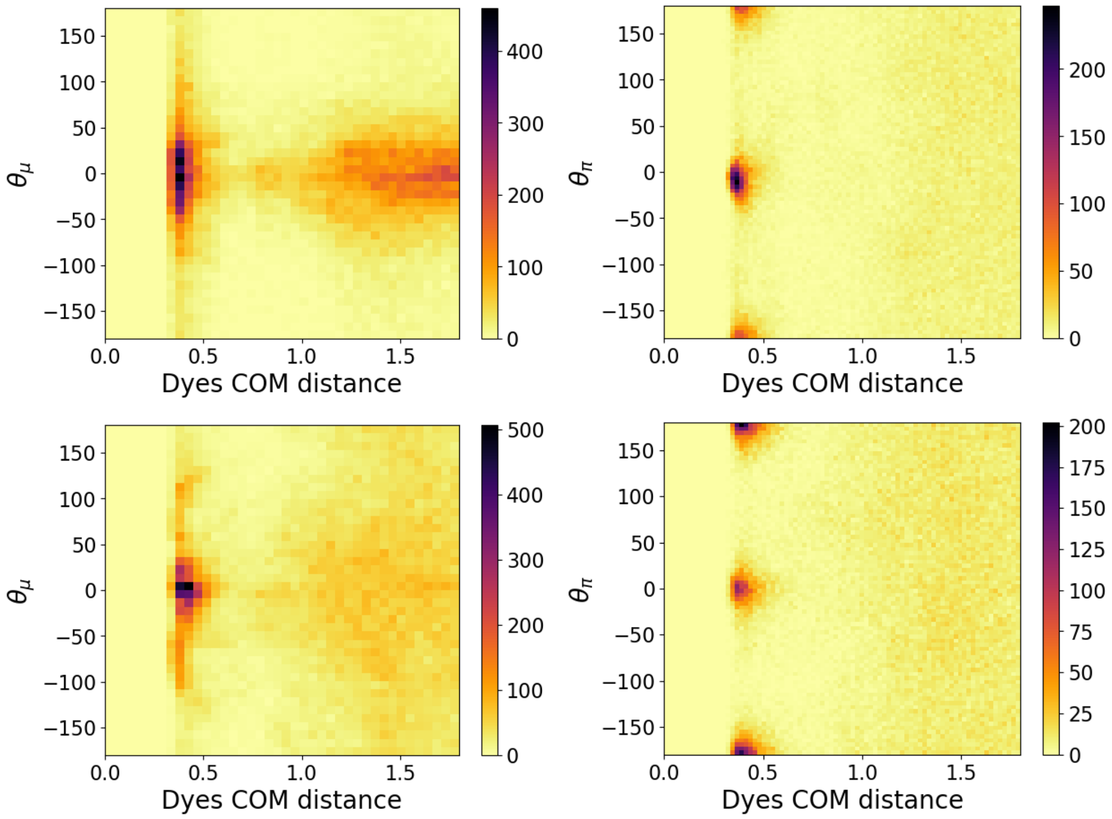

Figure 1.20: Bidimensional histograms of $\theta_\mu$ (left) and $\theta_\pi$ (right) over chromophore center of mass distance in **DMSO**. Top: results for clx-DA. Bottom: results for clx-D*A.

double exponential (Table 1.3) to extract the relevant time-scale that will be compared to the excited state decay in the next section.

$$C_{XX}(t) = a_0 \exp(b_0 t) + (1 - a_0) \exp(b_1 t)$$

with $X = d,\ \theta_\pi, \theta_\mu$.

The results in Fig. 1.22 confirm a strong similarity of behaviour in chloroform for the intermolecular distance and the orientational motions, with all variables dynamically active on a time scale of $\sim$ 10 ns. In contrast, in DMSO the orientational motion occurs on a faster time scale ($\sim 1ns$) than the variation of intermolecular distances ($\sim 5ns$).

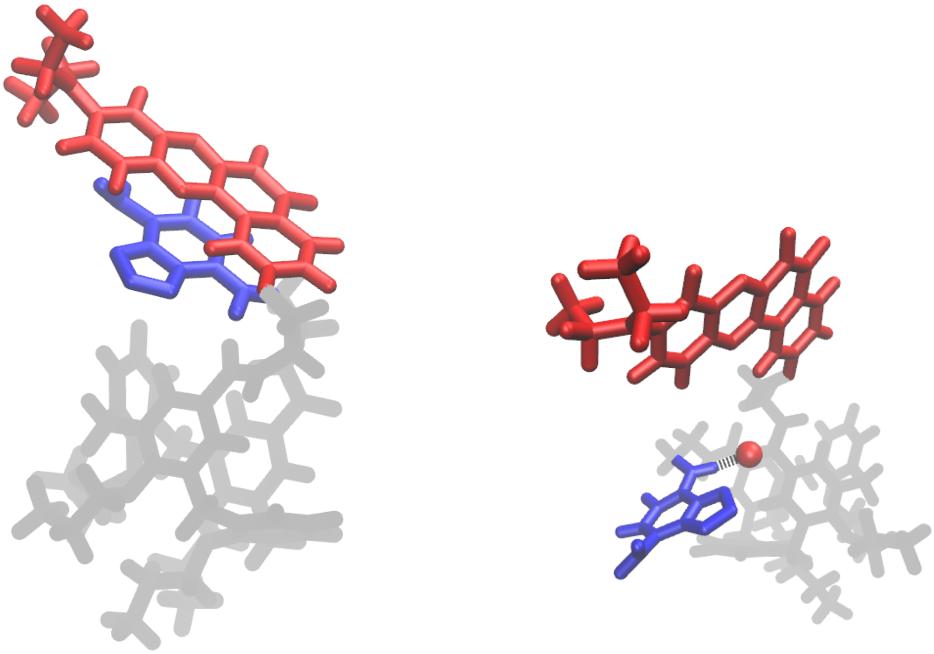

Figure 1.21: MD simulation snapshot of two of the most visited conformations in chloroform: left, $\pi - \pi$ stacking; right, *dye-linker* H-bond

## 1.4 A dynamical model for excited state decay

Simulating the relaxation of D* is quite tricky. In fact, once the donor has been excited, it can decay along different paths:

- Non-radiative decay, with kinetic constant $k_{nr}$
- Radiative decay, fluorescence, with kinetic constant $k_{rad}$
- Energy Transfer, with kinetic constant $k_{RET}$

The first two processes are marginally affected by the system dynamics, while the RET rate, being strongly dependent on the distance and mutual orientation of the dyes, is highly variable. We are particularly interested to understand and model the concurrent dynamics of RET and conformational motion, well beyond standard treatments

| | | $clx - DA$ Chloroform | $clx - DA$ DMSO |
|---|---|---|---|
| $d$ | fit range | :100000 | :100000 |
| | $a_0$ | 0.722 | 0.664 |
| | $b_0^{-1}$ | 11.63 | 5.47 |
| | $b_1^{-1}$ | 1.95 | 0.883 |
| $\theta_\pi$ | fit range | :100000 | :100000 |
| | $a_0$ | 0.678 | 0.748 |
| | $b_0^{-1}$ | 10.87 | 0.747 |
| | $b_1^{-1}$ | 0.37 | 0.052 |
| $\theta_\mu$ | fit range | :100000 | :100000 |
| | $a_0$ | 0.550 | 0.877 |
| | $b_0^{-1}$ | 11.76 | 1.02 |
| | $b_1^{-1}$ | 0.68 | 0.067 |

Sampling frequency: 10 ps.

Table 1.3: Parameters extracted from exponential fitting of autocorrelation functions of $d$, $\theta_\pi$ and $\theta_\mu$. All time constants are in ns.

that typically address two limiting cases. Specifically, if the molecular motion is much slower than the transfer process, dyes orientation is approximated as frozen and the orientational factor $\kappa^2$ is considered constant and set to a value ranging from 0 to 4, depending on the mutual orientation of the dyes. In the opposite case, the donor and acceptor have enough time to explore all their variable-space before exchanging energy, and $\kappa^2 = \frac{2}{3}$. In realistic situations, and especially for bound DA pairs, the situation is actually intermediate and calls for more detailed model, as made possible by MD.

In our approach we convert the rate of each decay path for D* (radiative/non-radiative decay, RET) into a probability. The constant rates for the radiative and non-radiative decay are set to the the experimental values. Instead, the probability decay along the the RET channel is controlled by the instantaneous value of $V_{DA}$. Plotting

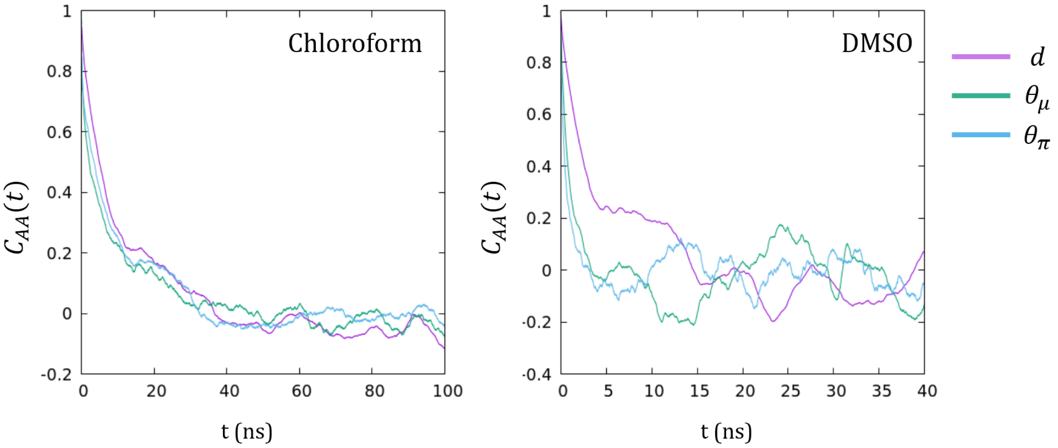

Figure 1.22: . Autocorrelation functions of distance $d$, $\theta_\mu$ and $\theta_\phi$, between D and A for clx-DA in chloroform (left) and DMSO (right)

the value of interaction, along with D-A separation, as a function of time (Fig. 1.23), it is clear how long inter-dyes distance is always related to a negligible magnitude of $V_{DA}$ while, as chromophores get closer, the interaction can assume large values, depending on relative orientation of transition dipole moments. Knowing, for a generic process, the characteristic decay time $\tau$, defined as:

$$\tau(t) = \frac{1}{k_{rad} + k_{nr} + k_{RET}(t)}, \tag{1.9}$$

we can assess an infinitesimal probability $P_{dt}$ to every "instant of time":

$$P_{dt} = \frac{1}{\tau} dt \;\rightarrow\; \int_0^{\tau} P_{dt} = 1 \tag{1.10}$$

Since MD simulation uses numerical integration, we only have access to finite time-steps $\Delta t$, and we need to translate Eqn. 1.10 into a discrete equation:

$$P_{\Delta t} = \frac{1}{\tau} \Delta t \;\rightarrow\; \sum_0^{\tau} P_{\Delta t} = 1 \tag{1.11}$$

In practice, each timestep carries a fraction of the probability for each of the possible paths.

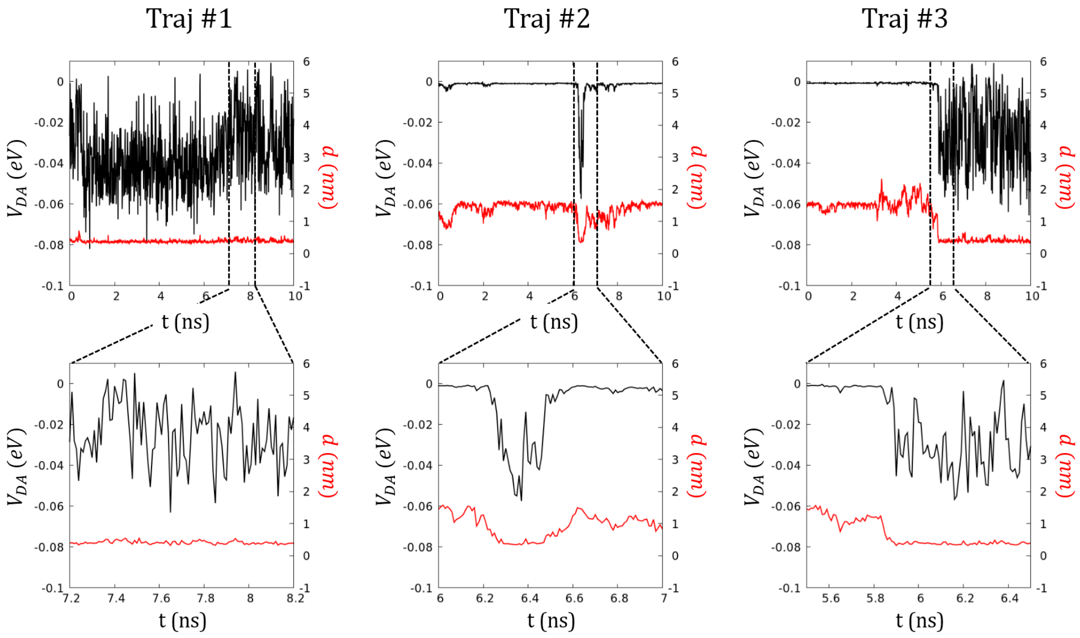

Figure 1.23: D-A interaction $V_{DA}$ (black lines) and Donor Acceptor distance $d$ (red lines) plotted as a function of time for three sample excited state trajecotries. Top panels: full dynamics; bottom panels: magnified sections of the aforementioned trajectories.

Energy transfer rate $k_{RET}$ is easily calculated from Eqn. 1.2, while $k_{rad}$ and $k_{nr}$ are extracted from lifetime ($\tau_D$) and quantum yeld ($\Phi$) experimentally measured on the isolated chromophore:

$$k_{rad} = \frac{1}{\tau_D} \cdot \Phi \quad k_{nr} = \frac{1}{\tau_D} - k_{rad} \tag{1.12}$$

Once $\Delta t$ and $\tau$ are determined relaxation time is calculated as follows:

1. Initialization

   A finite group of chromophores is selected; number of simulation steps is set to $N_{cycle} = -1$ and initial time is defined as $t = \Delta t \cdot N_{cycle}$

2. Time step

   Time is increased by $\Delta t$ ($N_{cycle} = N_{cycle} + 1$)

3. Decays
   For each molecule, a random number $0 \leq R_n < 1$ is generated:
   - if $R_n \leq \frac{1}{\tau}$, a relaxation occur
   - else, nothing happens

4. Continuation
   Relaxed molecules are removed from the initial group, and their decay time ($N_{cycle} \cdot \Delta t$) is saved; remaining chromophores are sent back to Step 2

5. End
   When all molecules are relaxed, the simulation stops

A graphical representation is shown in Fig. 1.24. In this example a generic step $N$ for an ideal system is illustrated. Remembering the relation between lifetime and rate constants (Eq.1.9), $P_{\Delta t}$ can be written as:

$$P_{\Delta t} = (k_{rad} + k_{nr} + k_{RET}) \cdot \Delta t = 3.5ns^{-1} \cdot 0.1ns = 0.35 \tag{1.13}$$

Each time step is represented by a box with $N_b = 200$ balls, of different colours. The colour of each ball represents the "action" pursued by the excited moiety for each timestep, as depicted in Fig. 1.24. Red, green and cyan balls all represent a de-excitation event, respectively RET, radiative decay and non-radiative decay, while the black balls accounts for timesteps in which the donor stays in the excited state. The portion of balls of each colour are directly related to the probability the excited donor has to take that path. The simulation consists in consecutively extracting a ball from each box, starting from box number 0, until a non-black ball is picked. The output of the simulation is a distribution of relaxation times, one for each molecule. Plotting the fraction of molecules in the excited state per time, an exponential profile is obtained. Moreover, being able to discriminate between the three different paths of relaxation, our model allows to determine the energy transfer efficiency for each system as the ratio between molecules relaxing through RET channel over all the decayed molecules:

$$\Phi_{RET} = \frac{N_{RET}}{N_{tot}} \tag{1.14}$$

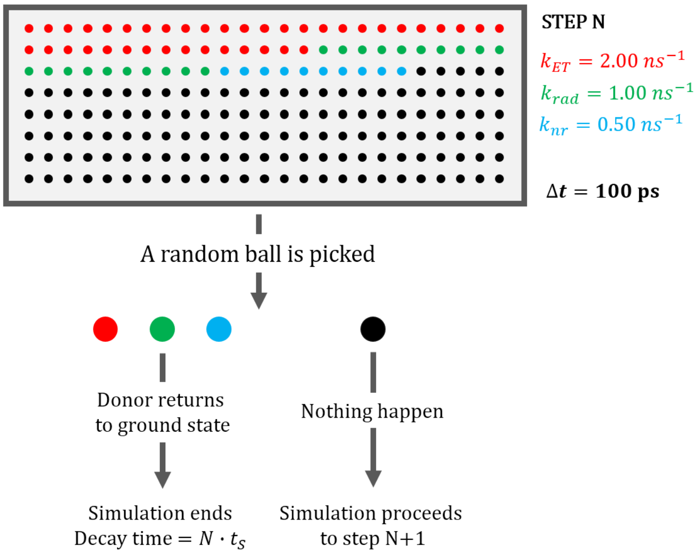

Figure 1.24: A simple graphic representing a generic step in the simulation.

### 1.4.1 Decay Times

To start with, we consider the isolated D*, setting $k_{RET} = 0$. The experimental lifetime of the free donor is $\tau = \frac{1}{k_{nr}+k_{rad}} = 7.0ns$. We selected a population of $10^5$ molecules and set the time step for the simulation to $\Delta t = 10ps$. In absence of RET the decay probability is $P_{\Delta t} = 1.429 \cdot 10^{-3}$ and we obtain quite naturally an exponential decay profile. The calculated distribution of decay-times is shown in Fig. 1.25. The cumulative difference over the histogram, generated subtracting to the total excited state population the number of molecule relaxing at each timestep, gives the characteristic exponential decay shown in the right panel. We now turn on the donor-acceptor interaction, and hence RET. Since the interaction between the chromophores depends on the separation and relative orientation between chromophores, that vary during dynamics, the new probability will be itself function of time ($P_{\Delta t}(t)$). We run a long clx-DA simulation ($1\mu s$) to have a statistically relevant number of configurations, and from this set we randomly select 1000 configurations, making sure that the subset gives a good replica of the original distribution (Fig. 1.26). For each configuration a 10 ns NVT dynamics

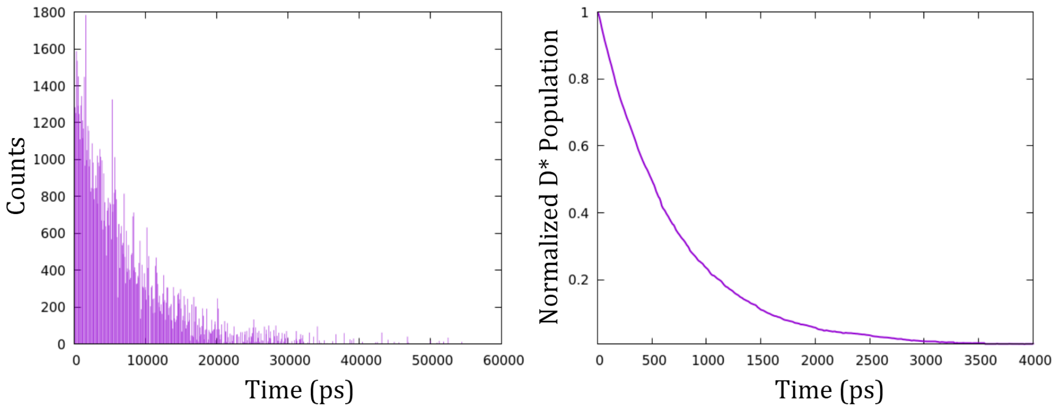

Figure 1.25: Left: distribution of relaxation times for $\tau = 7.0ns$; right: normalized excited population as function of time for the same system.

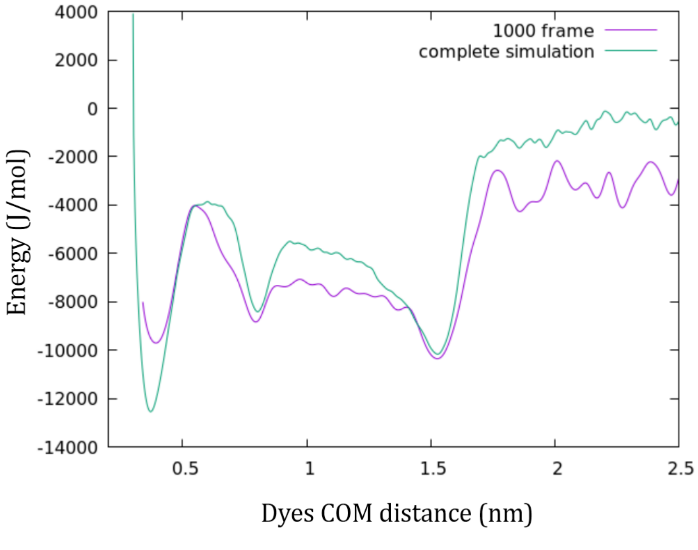

Figure 1.26: PMF curves calculated from the 1000 frames used to RET analysis (violet) and distribution calculated for all frames in the trajectory (green).

| **Fragment** | $\mu^t_x$ | $\mu^t_y$ | $\mu^t_z$ | $\lvert\mu^t\rvert$ | atom 1 | atom 2 |
|---|---|---|---|---|---|---|
| **Free NBD** | -1.1920 | 0.2826 | 0.0000 | 1.23 | N1 | N4 |
| **Free NR** | -3.0375 | 0.5667 | 0.0783 | 3.09 | C51 | C62 |

Table 1.4: Transition dipole moment components for the two chromophores. In MD simulations, the direction is determined by the versor connecting highlighted atoms in Fig. 1.27.

is calculated, simulating the donor excitation by switching the charge distribution with the one of clx-D*A.

The decay times following the instantaneous excitation were estimated calculating $V_{DA}(t)$, using transition dipole moments from the relaxed excited state to the ground state and from the ground state to the bright excited state, for donor and acceptor respectively. We assume that molecular properties, including the transition dipole moments, are marginally affected by the dynamics, so their magnitudes and orientations relative to the corresponding chromophoric units are constant. For each chromophore, two atoms are selected whose distance is parallel to the transition dipole moment orientation evaluated with ab-initio calculations (Table 1.4 and Fig. 1.27). For each instantaneous excitation dynamics, we were able to calculate $k_{RET}(t)$ as follows:

$$k_{RET} = \frac{V_{DA}^2}{\hbar^2 c} J_{DA} \tag{1.15}$$

where $c$ is the speed of light (in $m\ s^{-1}$) and $J_{DA}$ is the spectra overlap between NBD emission spectrum and NIR absorption spectrum, each normalized for unit area, considered constant in our model[34] ($1.95 \cdot 10^{-6}$ m). Following the strategy outlined above, we finally obtain a decay time for each derived trajectory. To further improve statistical accuracy we repeated the calculation 100 times for each dynamics, ending up with $10^5$ decays.

Fig. 1.28 shows the calculated decay of the excited donor, and compares the results of the dynamical calculation for the RET pair with those obtained for the isolated D dye. To fit the exponential decay of D* we used a multiple exponential fitting, with

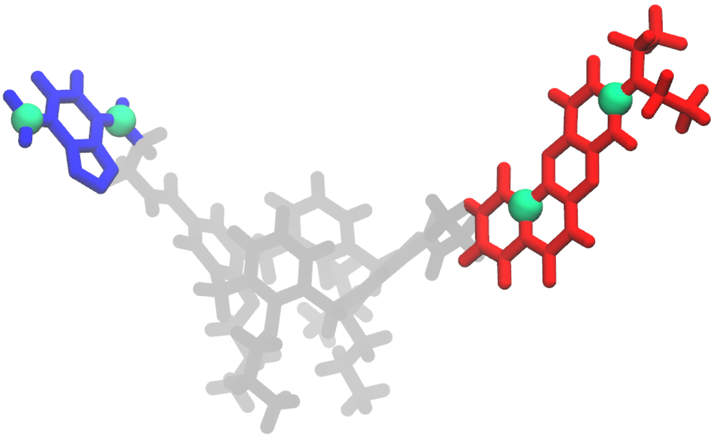

Figure 1.27: Representation of atoms chosen to define transition dipole versors

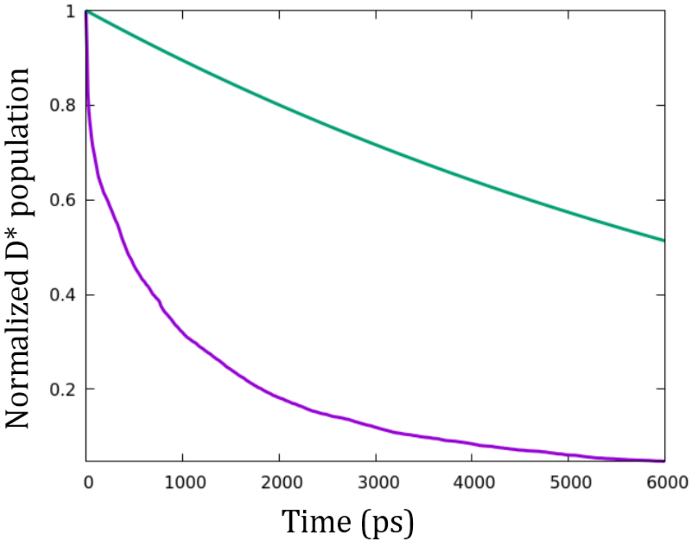

Figure 1.28: Time evolution of the D* population with (violet) and without (green) RET channel in chloroform.

equation:

$$F_{exp}(t) = \sum_i a_i \exp(-\beta_i t) \tag{1.16}$$

with $\sum_i a_i = 1$. Fittings are performed using the maximum number of exponential parameters, $N_{fit}$, so to have $a_{N_{fit}+1} < 0.05$. Of course, the exponential curve calculated when RET decay is not accounted for is fitted with a single parameter $\tau = \frac{1}{\beta} = 6.989ns$, in line with the imposed rates fitting the experimental lifetime of $7.0ns$. In the presence of RET data in Table 1.5 point to 4 different decay times. It is important to specify that the estimated relaxation times are affected by the time step of the MD simulation (and hence of the model): decay times smaller than the time-step are clearly not accessible. Since the fastest time found with fitting is ≈ 16 ps, very close to the lower boundary of 10 ps, we decided to interpolate $V_{DA}(t)$ to obtain a denser sampling (every 1 ps) in order to detect possible faster rates. Results from the four terms exponential fitting are shown in Table 1.6.

|  | **weight (a)** | **kinetic constant ($\beta$) ($ps^{-1}$)** | **Relaxation time ($\frac{1}{\beta} = \tau$) (ps)** |
|---|---|---|---|
| **A** | 0.313 | $6.28 \cdot 10^{-2}$ | 15.92 |
| **B** | 0.176 | $8.48 \cdot 10^{-3}$ | 117.92 |
| **C** | 0.408 | $2.67 \cdot 10^{-3}$ | 374.53 |
| **D** | 0.103 | $8.56 \cdot 10^{-4}$ | 1168.22 |

Table 1.5: Exponential fitting of simulated decays in chloroform: 1000 simulations, 100 iterations, 10 ps timestep.

In the new interpolated decay experiment four relaxation times are observed: the previous populations relaxing at 18 and 117 ps are now rearranged to give decay times of 1.82 and 55.87 ps. Regarding the slower terms ( **C** and **D**), they are in good agreement with the original data.

| | **weight (a)** | **kinetic constant ($\beta$) ($ps^{-1}$)** | **Relaxation time ($\frac{1}{\beta} = \tau$) (ps)** |
|---|---|---|---|
| **A** | 0.227 | $5.48 \cdot 10^{-1}$ | 1.82 |
| **B** | 0.181 | $1.79 \cdot 10^{-2}$ | 55.87 |
| **C** | 0.446 | $3.19 \cdot 10^{-3}$ | 313.48 |
| **D** | 0.146 | $9.66 \cdot 10^{-4}$ | 1035.20 |

Table 1.6: Exponential fitting of simulated decays in chloroform: 1000 simulations, 100 iterations, 1 ps interpolated timestep (from 10 ps real steps).

| | **weight (a)** | **kinetic constant ($\beta$) ($ps^{-1}$)** | **Relaxation time ($\frac{1}{\beta} = \tau$) (ps)** |
|---|---|---|---|
| **A** | 0.289 | $2.82 \cdot 10^{-2}$ | 35.52 |
| **B** | 0.527 | $1.00 \cdot 10^{-3}$ | 997.72 |
| **C** | 0.184 | $1.58 \cdot 10^{-4}$ | 6328.54 |

Table 1.7: Exponential fitting of simulated decays in DMSO: 100 simulations, 100 iterations, 10 ps timestep.

### 1.4.2 Simulations in DMSO

Similar calculation as reported in CHCl3 are performed in DMSO. From the comparison between PMF curves of the system in the two different solvents (Fig. 1.29) and the conformational analysis studies (discussed in Section 1.3.4), it is clear that DMSO promotes chromophore separation at the expense of $\pi - \pi$ stacking conformations. Moreover, under equal chromophore distances, DMSO causes a more diversified orientation between dyes. As a result, as also discussed in ref. [34], we expect a less efficient RET than in chloroform.

In Table 1.7, parameters of the three term exponential fitting are listed. Lifetimes in DMSO are significantly longer compared to the ones in chloroform (Fig. 1.30, with the fastest time at 24.33 ps. With the same protocol used for chloroform, each simulation has been interpolated in order to have a value of $V_{DA}$ every 1 ps. Results from the four

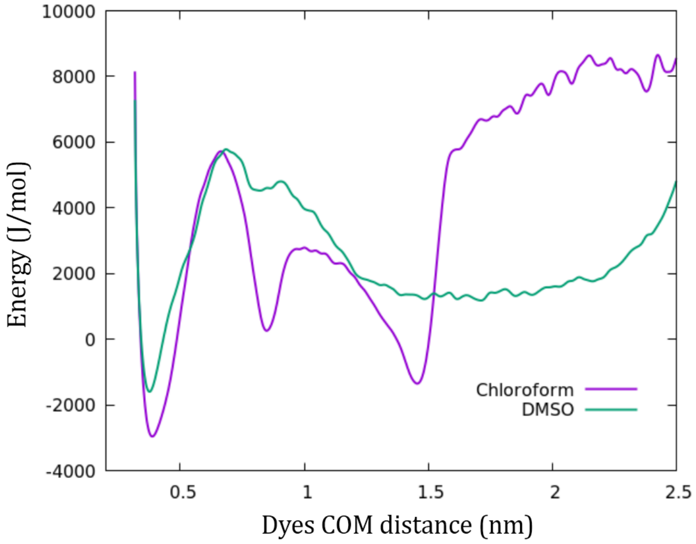

Figure 1.29: PMF curve as a function of dyes center of mass separation in chloroform (violet) and DMSO (green).

term exponential fitting are shown in Table 1.8. From the interpolated dynamics fitting two faster decay, with lifetimes of 4.82 and 23.36 ps, arise. The lifetimes in both organic solvents are compared to decay times calculated experimentally [34] (Table 1.9). The fastest decay times calcuated in both chloroform and DMSO are in perfect agreement with the experimental data, while longer times are underestimated by the exponential fitting.

### 1.4.3 Decay rates in static configurations

Calculations proved that the solvent plays a foundamental role in determining the RET rate due to different solvent-system interactions that strongly affect the distributions of chromophores distance and relative orientation and hence the $V_{DA}$ term. However, in dynamical environments, conformations rapidly change, so that the observed decay rate is governed by a complex interplay between equilibrium distributions and fluctuations. To further investigate the role of dynamic degrees of freedom, for comparison purposes,

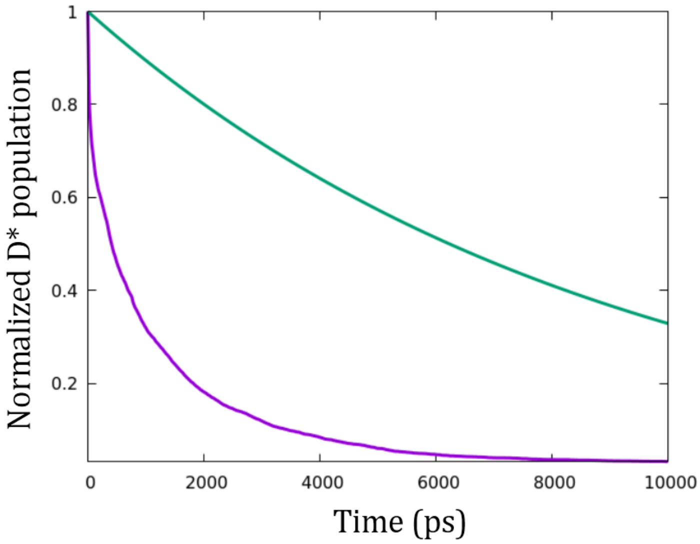

Figure 1.30: Time evolution of the D* population with (violet) and without (green) RET channel in DMSO.

| | **weight (a)** | **kinetic constant ($\beta$) ($ps^{-1}$)** | **Relaxation time ($\frac{1}{\beta} = \tau$) (ps)** |
|---|---|---|---|
| **A** | 0.095 | $1.35 \cdot 10^{-1}$ | 7.38 |
| **B** | 0.164 | $3.02 \cdot 10^{-2}$ | 33.12 |
| **C** | 0.309 | $1.83 \cdot 10^{-3}$ | 545.55 |
| **D** | 0.432 | $4.82 \cdot 10^{-4}$ | 2075.32 |

Table 1.8: Exponential fitting of simulated decays in DMSO: 100 simulations, 100 iterations, 1 ps interpolated timestep (from 10 ps real steps)

| **Chloroform** | | **Experimental Data** | **Molecular Dynamics** |
|---|---|---|---|
| | $t_1$ | 2.0 ps | 1.82 ps |
| | $t_2$ | 17.0 ps | 55.87 ps<br>313.48 ps |
| | $t_3$ | 1.8 ns | 1.04 ns |
| **DMSO** | | **Experimental Data** | **Molecular Dynamics** |
| | $t_1$ | 4.0 ps | 7.38 ps |
| | $t_2$ | 59.0 ps | 33.12 ps<br>545.55 |
| | $t_3$ | 4.5 ns | 2.01 ns |

Table 1.9: Comparison between experimental lifetimes[34] and exponential fittings from MD data

we performed "static" simulations where the decay is calculated maintaining the interaction $V_{DA}$ constant to the value obtained at the initial instant of each non-equilibrium dynamics (Fig. 1.31). Comparing the calculated $D^*A$ relaxation obtained from the fully dynamic calculation (black lines) with the static calculation (red lines) is instructive. It clearly shows that the conformational motion occurring after the excitation affects the interactions in the RET pair and hence RET probabilities. The conformational motion, occuring on comparable time scales as RET itself, strongly affects the relaxation dynamics of the system. Specifically, RET is much faster in a fully dynamical calculation than in a static approach. RET quantum yields are estimated from the fully dynamical calculation as 0.96 and 0.88 for chloroform and DMSO solutions, respectively, and reduce to 0.94 and 0.69 in the static calculation. This can be easily understood: in the dynamical calculation, in fact, the system explores a wider conformational space, including regions with fast RET decay. When these "hot spots" are reached, they offer preferential channels for relaxation. In a static simulation, once the population of these hot spots is depleted, they become ineffective, and RET necessarily occurs along slower channels. On the contrary, in a dynamical model, the population is continuously transferred to replenish these hot spots, so that fast channels stay active all along the process. Quite interestingly, the different results obtained in the static and dynamic calculations cannot be ascribed to different distributions of $k_{RET}$. Indeed the histograms calculated along the static and dynamic trajectories shown in Figure 1.31 are very similar. As the static scenario only refers to a sampling through graound-state MD, while the dynamic one is the results of the excited state (non-equilibrium) dynamics, the similarity of the two distributions suggests that the sources of non-equilibrium effects are actually rather modest.

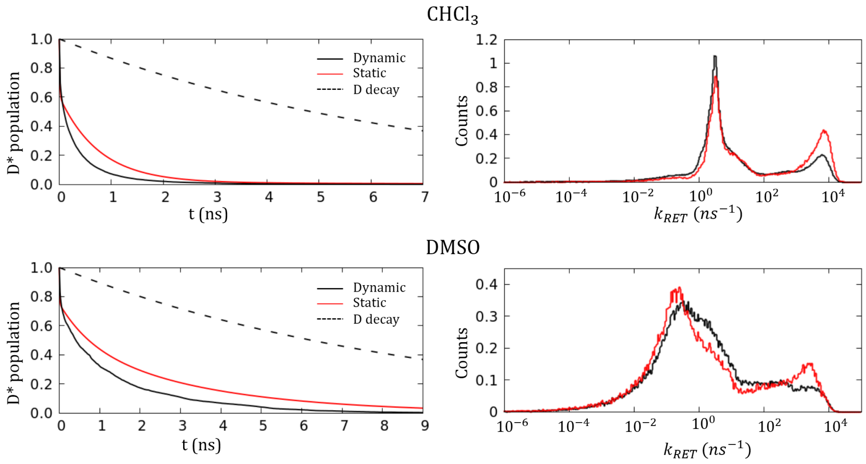

Figure 1.31: Left panels: decay of the $D^*$ population calculated in chloroform (top) and DMSO (bottom). Dashed lines refer to the exponential decay of the isolated D species; red lines show static results (obtained neglecting the conformational motion of the excited RET pair after excitation), and the black lines show the full dynamical result. Right panels show the (area normalized) distributions of the RET rates, resulting from static and dynamic calculations for both solvents

## 1.5 Conclusions

We proposed an original computational protocol for the calculation of the RET dynamics and quantum yields for a donor-acceptor pair in two different solvents, highlighting the importance of conformational fluctuations. The proposed approach is validated against an extensive set of experimental results available for a RET-pair bound via flexible links to a calixarene scaffold. We obtained a very good comparison with the experiment and solved a theoretical problem associated with this system, where estimates of $V_{DA}$ from TD-DFT calculations on few preselected representative configurations of the D-clx-A system underestimated the RET lifetimes by several orders of magnitude.[34]

Our approach combines equilibrium and non-equilibrium MD calculations with TD-DFT results, leading to a detailed description of the concurrent processes: $D^*$ decay, energy transfer and conformational dynamics. The conformational motion modulates $V_{DA}$, the intermolecular interaction responsible for RET. In a fully dynamical picture the system after photoexcitation is allowed to explore conformational regions where $V_{DA}$ is large, then opening fast RET channels and leading to faster RET than in a static picture, where the conformational motion is frozen.

RET in disordered systems is a delicate issue: the standard approach relying on the use of an average $\kappa^2$ value has been questioned in several ways. In the first place the factorization of the $V_{DA}$ interaction in a term $\kappa^2$ that only depends on the intermolecular orientation and in a term that only depends on the intermolecular distance, is incorrect - particularly if the system can explore regions where intermolecular distances are comparatively short. More generally those approaches represent a too crude approximation to describe $DA$ interactions in systems, like the one investigated here, where a complex supramolecular structure poses serious constraints to the mutual arrangements of the $D$ and $A$ moieties. We show that these problems can be easily addressed by ground state MD calculations, that offer reliable information on the conformational heterogeneity of the RET pair. However, we also demonstrated that this is not sufficient in the case investigated here. In such flexible systems, the conformational motion modulates intermolecular interactions on a timescale relevant to RET, leading to important effects that cannot be accounted for through an orientational average in either in the static or ultrafast regime.

# Chapter 2

# Molecular Aggregates

## 2.1 Introduction

Molecular materials are characterized by intermolecular forces much weaker than the chemical bonds inside each individual molecular unit. In spite of that, in molecular materials intermolecular interactions deeply affect optical spectra, that therefore cannot be calculated as the sum of molecular spectra. Intermolecular charge transfer (CT) was early recognized as a source of impressive spectroscopic phenomena in absorption spectra of molecular materials, both in the visible and near-IR spectral regions, where so-called CT absorption bands appear[36, 37]. Vibrational spectra are also affected by CT, with the appearance of strong features due to large charge fluxes driven by molecular vibrations or lattice modes (phonons).[38, 39, 40, 41] In molecular materials with intermolecular distances larger than the sum of Van der Waals radii, electrons are localized within each molecular unit and CT interactions are negligible. Even in these condition, electrostatic intermolecular interactions may have prominent effects, driving resonance energy transfer among different molecular species[17, 42, 43, 44] and energy delocalization among equivalent (or nearly so) molecules in molecular crystals and aggregates.[45, 46, 47] The physics of excitons and of optical spectra in molecular crystals was first addressed in the seminal works of Craig,[48] Davidov[49] and Agranovich[50]. The same physics also applies to molecular aggregates: the ground-breaking discovery of the anomalous spectra of cyanine dyes in poor solvents[51] opened the research field of molecular aggregates, with the seminal theoretical work of Kasha.[52] An enormous body of experimental and theoretical work can be found in the literature, as recently reviewed.[46, 47] Current understanding of optical spectra of molecular aggregates and crystals is mainly based on the so-called exciton model that, only accounting for electrostatic interactions among degenerate states, leads to a large reduction of the basis set. Analytical solutions have been obtained of the electronic problem that offer a reliable basis for understanding spectral properties of molecular aggregates and crystals. The approximations of the exciton model were discussed in the original papers[49, 50] and have been recently addressed in relation with aggregates of polarizable molecules with polar[53, 54, 55] or quadrupolar character.[56, 57, 58, 59]

Molecular vibrations add another layer of complexity to the physics of molecular aggregates and crystals: the deformation of the molecular structure upon excitation is responsible for the Franck-Condon structure of absorption and fluorescence spectra of isolated molecules in solution, but the shape of absorption and fluorescence spectra of molecular aggregates often largely deviates from the Franck-Condon behavior,[60, 46] as first recognized in the narrow and structurless absorption and emission spectra of aggregates of cyanine dyes.[51] Delocalization energies and vibrational energies are often comparable in molecular aggregates and the adiabatic approximation must be abandoned. Treating the electronic and vibrational degrees of freedom on the same foot is a formidable task. Indeed analytical solutions of the coupled electronic and vibrational problem are available for an infinite one-dimensional array of molecules in the exciton approximation and accounting for a single coupled vibration.[60, 61] Most often, approximations schemes have been proposed to treat the problem, whose validity and applicability need a careful discussion.

In this chapter we will address spectral properties of molecular aggregates, discussing first aggregates of polar and polarizable dyes, extending a previous work[53, 62] to account for vibrational coupling and hence for spectral band-shapes. We will then turn attention to aggregates of non-polar, yet polarizable, dyes, addressing the reliability of the Heitler-London approximation. Finally we will briefly address the behavior of two dimensional aggregates. This chapter is based on a published work on aggregates of non polar dyes (Anzola M, Di Maiolo F, Painelli A. Optical spectra of molecular aggregates and crystals: testing approximation schems, PCCP 2019), and a second paper (in preparation) on aggregates of polar and polarizable dyes.

## 2.2 Aggregates of polar and polarizable dyes

### 2.2.1 DA chromophores as polar and polarizable dyes

Conjugated dyes with an electron-donor (D) and acceptor (A) group represent a large family of dyes of interest for several applications, ranging from non-linear optics[63], molecular electronics[64, 65], OLED[5] etc. Interamolecular interactions in aggregates of these dyes considerably alter their spectral properties[54, 55, 66] One of the most widely used approximation to describe DA dyes is the so called Mulliken model[36, 39, 67], in which a dye is described in terms of two electronic states, a neutral ($|DA\rangle$) and a zwitterionic ($|D^+A^-\rangle$) state. The underlying hypothesis is that higher excited states are located at too large energies to be relevant. Indeed the dyes of interest typically have the lowest excited state in the visible region of the spectrum, while higher excited states are in the ultraviolet region. Defining $2z_0$ as the energy difference between the two states and $-\tau$ the mixing matrix element, the Hamiltonian reads

$$\hat{H} = \begin{pmatrix} 0 & -\tau \\ -\tau & 2z_0 \end{pmatrix} = 2z_0\hat{\rho} - \tau\hat{\sigma_x} \tag{2.1}$$

In the following we will set $\tau = 1$ as the energy unit.

The Hamiltonian can be readily diagonalized, giving the eigenvalues $E_g = z_0 - \sqrt{z_0^2 + \tau^2}$ and $E_e = z_0 + \sqrt{z_0^2 + \tau^2}$ and eigenstates

$$\begin{aligned} |g\rangle &= \sqrt{1-\rho}\,|DA\rangle + \sqrt{\rho}\,\left|D^+A^-\right\rangle \\ |e\rangle &= -\sqrt{\rho}\,|DA\rangle + \sqrt{1-\rho}\,\left|D^+A^-\right\rangle \end{aligned} \tag{2.2}$$

where $\rho = \langle g|\hat{\rho}|g\rangle$ measures the weight of the zwitterionic state in the ground state, and hence the molecular polarity. Its dependence on $z_0$ is (see also Fig 2.1a):

$$\rho = \frac{1}{2} - \frac{z_0}{2\sqrt{z_0^2+1}} \tag{2.3}$$

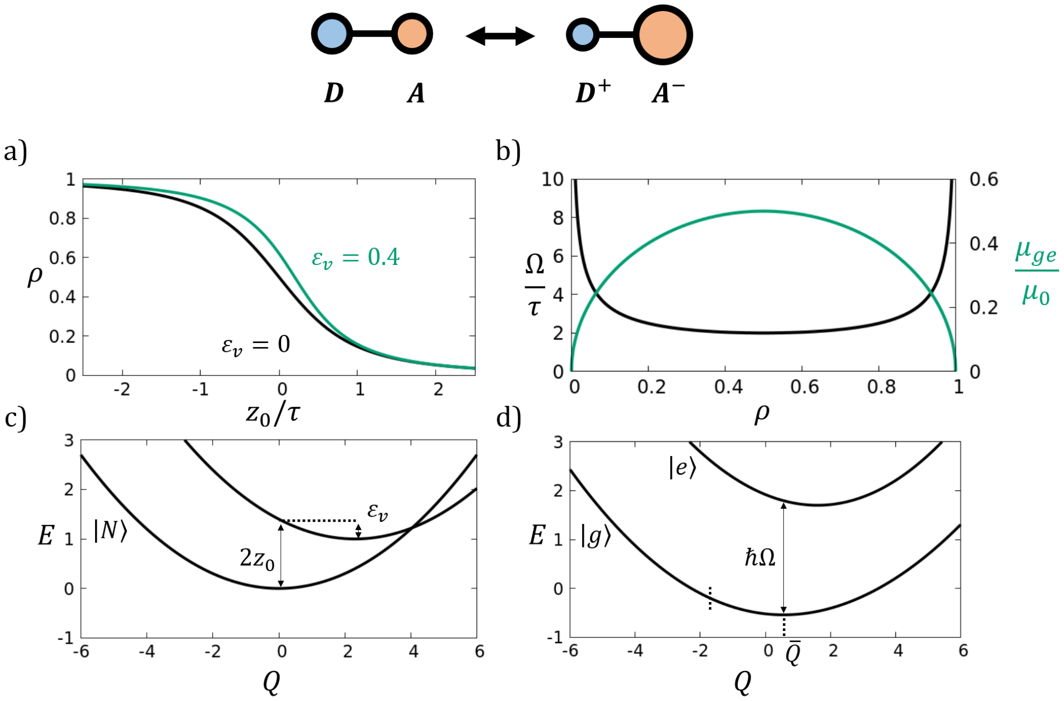

Figure 2.1: The isolated (gas-phase) dye. Top: the two resonating structures. (a) The $\rho$ dependency from $z_0$. (b) the transition energy $\Omega$ and the transition dipole moment as a function of $\rho$. (c) The potential energy surfaces for a system with $\varepsilon_v = 0.4$ and $z_0 = 0.7$. (d) The adiabatic PES calculated for the same system as in panel (c).

To address optical spectra we need a definition of the dipole moment operator ($\hat{\mu}$). Following Mulliken [36], we neglect all matrix elements of the dipole moment operator in the chosen basis but $\mu_0$, the large dipole moment associated with the zwitterionic state. Accordingly, the dipole moment operator reads:

$$\hat{\mu} = \mu_0 \hat{\rho} = \begin{pmatrix} 0 & 0 \\ 0 & \mu_0 \end{pmatrix} \tag{2.4}$$

All spectral properties can be expressed as function of $\rho$. Specifically, the transition energy and the transition dipole moments read:

$$\hbar\Omega = \frac{1}{\rho(1-\rho)} = \frac{1}{\beta} \tag{2.5}$$

$$\langle g|\hat{\mu}|e\rangle = \mu_0 \beta \tag{2.6}$$

and the mesomeric dipole moment, the difference between the permanent dipole moments in the excited and ground states reads

$$\Delta\mu = \mu_0(1-2\rho) = \mu_0\alpha \tag{2.7}$$

The dependence of transition energy and dipole moment on $\rho$ is shown in Fig. 2.1b. The $\Delta\mu(\rho)$ dependence, a straight line, is not shown.

To properly address the shape of optical spectra of polar aggregates, molecular vibration coupled to the electronic system must be taken into account. As sketched in Fig 2.1(c,d), we introduce a single effective vibrational coordinate $Q$, and assign to the two basis states two harmonic potential energy curves with the same curvature and displaced minima. The relevant Hamiltonian reads:

$$\hat{H} = 2z_0\hat{\rho} - \tau\hat{\sigma}_x + \hbar\omega_v(\hat{a}^\dagger\hat{a} + \frac{1}{2}) - g(\hat{a}^\dagger + \hat{a})\hat{\rho}. \tag{2.8}$$

where $\omega_v$ and $g$ are the frequency and the electron-vibration coupling of the effective vibrational mode, respectively (see Fig. 2.1c). The coordinate and its conjugated momentum are expressed in second quantization as follows

$$\begin{aligned} Q &= \sqrt{\frac{\hbar}{2\omega_v}}(\hat{a}_i^\dagger + \hat{a}_i) \\ P &= i\sqrt{\frac{\hbar\omega_v}{2}}(\hat{a}_i^\dagger - \hat{a}_i) \end{aligned} \tag{2.9}$$

The vibrational relaxation energy (see Fig. 2.1c) is $\varepsilon_v = g^2/\omega_v$. In the adiabatic approximation the two-dimensional electronic Hamiltonian is diagonalized for each $Q$ to get the $Q$-dependent adiabatic eigenstates whose energy as a function of $Q$ is shown in Fig. 2.1d.

If we are only interested in adiabatic results at equilibrium $Q$

$$\bar{Q} = \sqrt{\frac{2\omega_v}{\hbar}} \frac{g}{\omega^2} \rho \tag{2.10}$$

we may solve the equilibrium adiabatic Hamiltonian that reduces to the two-state electronic Hamiltonian in Eq. 2.1 but with the energy gap between the N and Z states that self-consistently depends on the $\rho$: $2z = 2z_0 - 2\varepsilon_v \rho$ [68]. This self-consistent problem is easily solved to get the $\rho(z0)$ for fixed $\epsilon_v$ (see Fig. 2.1a).

### 2.2.2 The model for the aggregate

To model an aggregate we consider a linear ordered array of $N$ DA dyes, imposing periodic boundary conditions to minimize finite size effects, while preserving translational symmetry. In line with the standard model to describe aggregates, we assume that intermolecular distances are large enough to neglect the overlap between orbitals on nearby molecules, so that electrons are fully localized on the molecular units, and intermolecular interactions are only due to electrostatic forces. The aggregate Hamiltonian is the sum of the molecular Hamiltonians plus a term that accounts for electrostatic intermolecular interactions:

$$\hat{H} = \sum_i (2z_0\hat{\rho}_i - \tau\hat{\sigma}_{x,i}) + \frac{1}{2}\sum_{i,j} V_{ij}\hat{\rho}_i\hat{\rho}_j + \hbar\omega_v \sum_i (\hat{a}_i^\dagger \hat{a}_i + \frac{1}{2}) - g\sum_i (a_i^\dagger + \hat{a}_i)\hat{\rho}_i \tag{2.11}$$

where $V_{ij}$ is the electrostatic interaction between two molecules in their zwitterionic state, and $i$,$j$ run over all aggregate units.

The adopted model for dipolar aggregates, despite its semplicity, implies a problem related to its dimension. Indeed, the dimension of the electronic basis grows as $2^N$, allowing to treat fairly large aggregates (up to more than 10 molecules). But vibrations must be accounted for in a non-adiabatic approach to properly deal with aggregates, and if just 5 vibrational quanta are considered per molecule, one ends up with a basis increasing as $10^N$, making the problem intractable already at $N \sim 3-4$. In the following we will discuss strategies to deal with this problem, before showing selected results.

### 2.2.3 Electronic Hamiltonian: the rotation on adiabatic states

We start our discussion focusing on the electronic Hamiltonian, corresponding to Eq. 2.8 with $g$=0:

$$\hat{H}^{el} = \sum_i (2z_0\hat{\rho}_i - \tau\hat{\sigma}_{x,i}) + \frac{1}{2}\sum_{i,j} V_{ij}\hat{\rho}_i\hat{\rho}_j \tag{2.12}$$

This Hamiltonian, written on the diabatic DA e $D^+A^-$ basis, is fairly simple, but we need to account for all $2^N$ states already to describe the ground state. In fact each molecular unit is described in the ground state by a linear combination of the DA and $D^+A^-$ state (see equation 2.2). Therefore it is convenient to rotate the electronic basis and rewrite the Hamiltonian on the adiabatic basis, $g$ and $e$. Of course the rotation does not affect the basis dimension. However, as it will be discussed below, a proper choice of the adiabatic basis will help us to better understand the physics of the system, also allowing for a controlled truncation of the basis, while maintaining the quality of the results.

Following a previous work[69] we define two new operators, linear combinations of Pauli operators $\sigma_{x,z}$, whose projections are defined by the parameter $\rho$:

$$\begin{aligned}\hat{S}_{x,i} &= -2\beta\hat{\sigma}_{z,i} + \alpha\hat{\sigma}_{x,i}\\ \hat{S}_{z,i} &= \alpha\hat{\sigma}_{z,i} + 2\beta\hat{\sigma}_{x,i}\end{aligned} \tag{2.13}$$

where $i$ runs on the molecular sites and $\alpha = 1 - 2\rho$ and $\beta = \sqrt{\rho(1-\rho)}$ are the same variables introduced previously. The above operators are then expressed in terms of creation and annihilation operators:

$$\begin{aligned}\hat{S}_{x,i} &= 1 - 2\hat{b}_i^\dagger\hat{b}_i\\ \hat{S}_{z,i} &= (\hat{b}_i^\dagger + \hat{b}_i)\end{aligned} \tag{2.14}$$

The operator $\hat{b}_i^\dagger$ creates an excitation on site $i$, by turning the molecule from state $|g\rangle$ to $|e\rangle$, while $\hat{b}_i$ destroys the excitation. As discussed by Agranovich,[70] these operators obey a Paulion algebra:

$$[\hat{b}_i, \hat{b}_j^\dagger] = \begin{cases} 1 - 2\hat{b}_j^\dagger \hat{b}_i, & \text{if } i = j \\ 0, & \text{if } i \neq j. \end{cases} \tag{2.15}$$

The electronic Hamiltonian in Eq. 2.11 can be rewritten in terms of these new operators as follows:[69]

$$\begin{aligned} \hat{H}_{ge}^{el} = & \sum_i \hat{n}_i \left[2\alpha\left(z_0 + M\rho\right) + 4\beta\tau\right] + \sum_i (\hat{b}_i^\dagger + \hat{b}_i)\left[2\beta\left(z_0 + M\rho\right) - \alpha\tau\right] \\ & + \frac{1}{2}\sum_{i,j} V_{ij}\beta^2(\hat{b}_i^\dagger \hat{b}_j + \hat{b}_i^\dagger \hat{b}_j^\dagger + h.c.) + \frac{1}{2}\sum_{i,j} V_{ij}\alpha^2(\hat{n}_i\hat{n}_j) + \sum_{i,j} V_{ij}\alpha\beta(b_i^\dagger + \hat{b}_i)\hat{n}_j \end{aligned} \tag{2.16}$$

where $M = \sum_{i>j} V_{ij}/N$ and $\hat{n}_i = \hat{b}_i^\dagger \hat{b}_i$ counts the number of excitons on the i-th site. The above equation holds true for any value of $\rho$ in the range $[0, 1]$. However, a clever choice would fix $\rho$ as to impose the vanishing of the prefactor of the $\hat{b}_i^\dagger + \hat{b}_i$ terms in the above Hamiltonian. In these conditions in fact the Hamiltonian would reduce to a Hamiltonian that counts the molecular excitations and accounts for electrostatic intermolecular interactions. Imposing the vanishing of this term, corresponds to fix $\rho$ precisely as in Eq. 2.3, but with $z_0$ replaced with $z_{eff} = z_0 + M\rho$.

The proposed transformation has an important physical meaning. Indeed the best choice of $\rho$ fixes it to its mean field (mf) value. In the mf approximation each molecule feels the potential generated by the surrounding molecules and this potential affects the energy gap $2z$ needed to turn a molecule from neutral to zwitterionic (see Fig. 2.2c,d). Of course the potential generated by the surrounding molecules is proportional to $\rho$, measuring the charge residing on the D and A site, leading to a self-consistent problem, that, first addressed by Soos [37] to describe the neutral-ionic phase transition in mixed stack crystals, was subsequently used to describe aggregates and crystals of DA dyes.[40, 57, 55]

Fig. 2.2(e,f) show the $\rho$ vs $z_0$ dependence calculated for systems with different $M$ values. For $M > 0$ (repulsive interactions) the ionicity of the molecule inside the aggregate decreases, as a result of intermolecular interactions that disfavor charge separation. For attractive interactions ($M < 0$) the ionicity of the molecule in the aggregate increases,

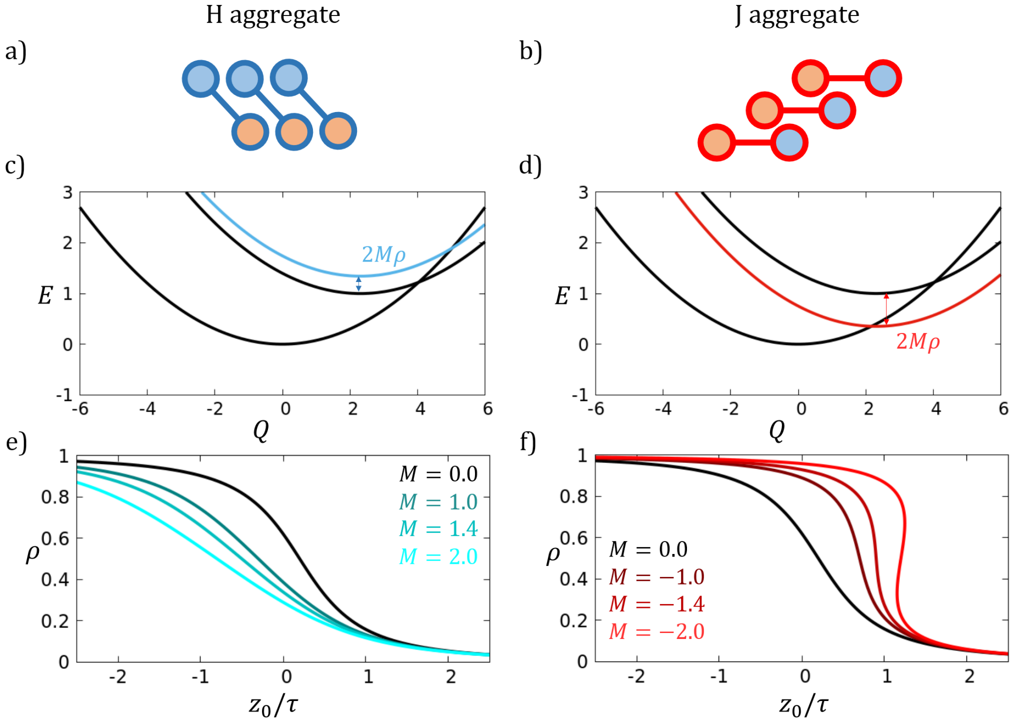

Figure 2.2: Panels (a) and (b) show the H and J geometries, respectively. (c) The diabatic PES for the isolated dye and for a dye in a H-aggregate. (d) The diabatic PES for the isolated dye and for a dye in a J-aggregate. (e) The $\rho(z_0/\tau)$ curves calculated for a H aggregate with $M = 0$ (isolated dye) and M=1. (e) The $\rho(z_0/\tau)$ curves calculated for a J aggregate with M=0 (isolated dye) and $M$=-1, -1.4 and -2.0 eV. All results refer to systems with $\varepsilon_v = 0.4$.

as intermolecular interactions favor charge separation. Quite interestingly, for large attractive interactions ($M < -2$) the S-shaped $\rho(z_0)$ curve signals the appearance of a bistable region. [71, 72, 73]

It is important to notice that, when solving the mf molecular problem, the $\rho$-dependence of all spectral properties (transition energy and dipole moment and the mesomeric dipole moment) stays exactly the same as for the isolated dye, so that Eqs 2.8 and 2.11 still apply. The curves in Fig. 2.2 similarly describe the mf dye, provided that $\rho$ is fixed to the mf value.

### 2.2.4 Accounting for vibrations: the Lang-Firsov transformation

Having addressed the proper rotation of the electronic basis, we now turn attention to the vibrational basis. To remain consistent during the rotation, a Lang-Firsov transformation is applied, to ensure the correct placement of the potential minimum to the ground state equilibrium value for the (mf) ground state:

$$\begin{aligned}
\hat{Q} &= \sqrt{\frac{\hbar}{2\omega_v}}(\hat{a}+\hat{a}^\dagger) \quad \rightarrow \quad \hat{\tilde{Q}} = \hat{Q} - \overline{Q} \\
\hat{P} &= i\sqrt{\frac{\hbar\omega_v}{2}}(\hat{a}^\dagger-\hat{a}) \quad \rightarrow \quad \hat{\tilde{P}} = \hat{P}
\end{aligned} \tag{2.17}$$

The total Hamiltonian in the transformed basis then reads

$$\begin{aligned}
\hat{H}_{ge} = \quad & \hbar\Omega\sum_i \hat{n}_i + \hbar\omega_v\sum_i\left(\hat{\tilde{a}}_i^\dagger\hat{\tilde{a}}_i + \frac{1}{2}\right) \\
& -g\Big[\alpha\sum_i \hat{n}_i(\hat{\tilde{a}}_i^\dagger + \hat{\tilde{a}}_i) + \beta\sum_i(\hat{b}_i^\dagger + \hat{b}_i)(\hat{\tilde{a}}_i^\dagger + \hat{\tilde{a}}_i)\Big] \\
& +\frac{1}{2}\beta^2\sum_{i,j}V_{ij}(\hat{b}_i^\dagger b_j + \hat{b}_i^\dagger\hat{b}_j^\dagger + h.c.) \\
& +\frac{1}{2}\alpha^2\sum_{i,j}V_{ij}(\hat{n}_i\hat{n}_j) + \alpha\beta\sum_{i,j}V_{ij}(b_i^\dagger + \hat{b}_i)\hat{n}_j
\end{aligned} \tag{2.18}$$

The first line in this equation assigns energy $\hbar\Omega$ to each exciton and adds the vibrational energy $\hbar\omega_v$ for each vibrational quantum. The second line accounts for vibrational coupling and, as expected, it is an on-site term. The first term in this line is the standard Condon term, with the vibrational coupling renormalized from $g$ to $g(1-2\rho)$ to account for the relative position of the equilibrium geometries for the $|g\rangle$ and $|e\rangle$ PES.[74] The second term in the second line is instead an ultraexcitonic term mixing states with the number of exciton differing by one unit. This ultraexciton term has a vibronic origin: the creation/destruction of the exciton on site $i$ is always accompanied by the creation or destruction of a vibrational quantum in the same site. The terms in the two last lines of Eq. 2.18 all come from intermolecular electrostatic interactions. The term in the third line is proportional to the squared transition dipole moment of the mf dye (see eq. 2.6) and contains both the exciton hopping term, as well as the two-exciton terms that are usually neglected in the exciton model.[75] In the last line the first term is an exciton-exciton interaction term (proportional to the squared mesomeric moment): it conserves the exciton number and it may enter the exciton model, but is of course relevant only to aggregates of polar dyes.[53] The very last term is again an ultraexcitonic term mixing states whose exciton number changes by one unit.

### 2.2.5 Computational Strategy

The dimension of the basis of the non-adiabatic problem increases fast with the aggregate dimension. On each molecular unit the basis includes 2 electronic states to be multiplied by a number $n_{ph}$ of vibrational states as needed for convergence. The basis for an aggregate of $N$ molecules has then dimension $(2n_{ph})^N$, quickly leading to intractable problems. To overcome this limitation we make use of symmetry. Imposing periodic boundary conditions in fact helps to minimize finite size effects, while enforcing translational symmetry in the system. The wavevector $k$ is a good quantum number for the system and optical transitions obey a strict selection rule imposing that only states with the same wavevector can be reached. The ground state is a zero-wavevector state, so that only the $k = 0$ subspace is of interest for absorption processes. Emission phenomena are less trivial. In aggregates with attractive interactions (J-aggregates) the lowest excited state is also a zero wavevector state, so that again only the $k = 0$ subspace if of interest. In H aggregates, instead, the lowest excited state (the fluorescent state) belongs to the $k = \pi$ subspace, so that for the calculation of fluorescence in aggregates with repulsive interactions we must diagonalize the Hamiltonian in this sub-space.

To further reduce the basis dimension we take advantage from the exciton basis that, while leading to a fairly cumbersome Hamiltonian, allows, for not too large intermolecular interactions, to limit the basis dimension discarding all states with a number of excitations larger than $M_e$ with $M_e < N$. In addition we truncate the vibrational basis as to discard all state with a total number of vibrational quanta larger than $M_v$.

In the bit-representation we store each basis state in the computer memory as an integer number whose binary code is composed of 4 bits for each molecule in the aggregate, where the first bit represents the electronic state ($0 \equiv |g_i\rangle, 1 \equiv |e_i\rangle$) and the following 3 bits store the integer number that counts the vibrational quanta (from a minimum of $000 \equiv |0_i\rangle$ to a maximum of $111 \equiv |7_i\rangle$) (Fig. 2.3). The basis set is created scrolling through all integer numbers from 0 to $16^{N-1}$ and selecting only the numbers corresponding to states that comply with the required values of $M_e$ and $M_v$. Translational symmetry operations are then applied to the basis states to finally obtain symmetry-adapted linear combinations in the $k = 0$ space, as needed to calculate absorption of J and H-aggregates, and in the $k = \pi$ subspace to calculate fluorescence of H-aggregates. Since the basis is very large, we do not store the full non-symmetrized basis, but we only store a single representative state for each symmetry-adapted linear combination together with the information concerning its multiplicity. The Hamiltonian in Eq.2.18 is finally written on the symmetrized basis and diagonalized in the relevant subspaces. Depending on the number of excitons and vibrational states needed to reach convergence, we are able to address systems with up to $N = 7$ sites (of course only aggregates with even $N$ can be considered in the $k = \pi$ subspace).

Once the Hamiltonian is diagonalized getting the ground $|G\rangle$ and the excited vibronic eigenstates $|E\rangle$, we calculate the linear absorption spectra, assigning a gaussian lineshape with width $\sigma = 0.0425$ to each transition:

$$\sigma(\omega)_{ass} \propto \hbar\omega \sum_{E} |\langle E|\hat{\mu}|G\rangle|^2 e^{-\frac{1}{2}\frac{(\hbar\omega_{EG}-\hbar\omega)^2}{\sigma^2}}, \tag{2.19}$$

where $\hbar\omega_{EG}$ is the energy of the $|E\rangle \rightarrow |G\rangle$ transition.[76] An analogous expression is used for emission:

$$I(\omega)_{fluo} \propto (\hbar\omega)^3 \sum_{E<F} |\langle E|\hat{\mu}|F\rangle|^2 e^{-\frac{1}{2}\frac{(\hbar\omega_{EF}-\hbar\omega)^2}{\sigma^2}}, \tag{2.20}$$

where the fluorescent state $|F\rangle$ is selected as the lowest energy state in the excited state

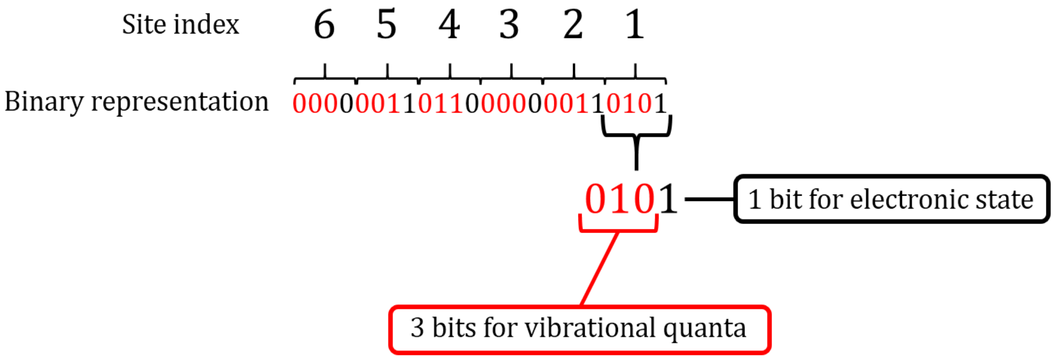

Figure 2.3: Graphic representation of the bit allocation.

manifold.

### 2.2.6 Results

In the following we only account for nearest neighbor interactions, so that $M = V$, with $V$ measuring the interaction between two nearby molecules in the zwitterionic state. Moreover we fix $\varepsilon_v = 0.4$ and $\omega_v = 0.17$. Results are shown for different $z_0$ as to consider dyes with different ionicities.

#### Weak Coupling

We start our analysis with H-aggregates, setting a moderate value for the electrostatic interaction, $V = 1$. Fig. 2.4 shows results for a largely neutral dye ($\rho$=0.2) a dye with intermediate ionicity ($\rho = 0.64$) and a zwitterionic dye ($\rho = 0.8$). Results are shown for the biggest achievable aggregate $N$=6, but finite size effects are in this case negligible. Moreover convergence is obtained already for $N_e$=3, as the $N_e = 3$ and 4 results are superimposed in the scale of the figure. In all cases, in line with the H-nature of the aggregate, as determined by repulsive intermolecular interactions, the fluorescence intensity is largely suppressed and a huge Stokes shift is observed for the aggregate. Understanding the position of absorption bands is however tricky. With reference to the isolated (gas phase) dye, the absorption band blueshifts for the dyes with low and intermediate polarity (left and central panels), but red-shifts in the case of a largerly polar dye (right panel). These apparently crazy results, possibly suggesting the failure of the exciton picture, are indeed related to a bad choice of the reference state. A large part of the shift in fact is not excitonic in origin, but is related to the effects that surrounding charges have on the energy of the states. This is easily calculated in the mf approximation, solving the problem for an isolated dye feeling the potential from the surrounding dyes. Repulsive intermolecular interactions leads to a reduction of the polarity of each dye in the aggregate (see fig. 2e) and hence to a variation of the frequency of the absorption band. The proper reference for the exciton model is indeed represented by the mf frequency. Specifically, for the dye in the left panels of Fig. 2.4, the ionicity decreases from 0.19 in the gas phase to a mf value of 0.17. Accordingly, the maximum of the absorption blueshifts, slightly reducing the exciton shift. Similar considerations apply to the dye in the middle panels, whose ionicity is reduced from 0.64 in the gas phase to 0.5 in the mf approach. For $\rho = 0.5$ (the so-called cianine limit) the Condon vibrational coupling (proportional to the squared mesomeric dipole moment) vanishes leading to the disappearance of the vibronic structure for absorption and fluorescence bands. More inspiring is the case of the zwitterionic dye in right column of Fig. 2.4. Here the decrease of the ionicity from 0.76 in the gas phase to 0.61 in the mf approximation is responsible for a large red-shift of the absorption band. Taking as proper reference the mf frequency, a blue-shift of the absorption band is observed for the aggregate, fully in line with its H character, as due to repulsive ($V > 0$) intermolecular interactions.

Fluorescence in H-aggregates comes from electronic states at the border of the Brillouin zone and are only allowed due to the coupling to vibrational modes. As a result, very weak and largely red-shifted bands are observed, but what we notice here is that, since the dominating (Condon) term accounting for electron-vibration coupling vanishes in the cyanine limit, the fluorescence intensity is vanishingly small in this limit.

A similar analysis can be done for the aggregates in Fig. 2.5, corresponding to the case of weak attractive intermolecular interactions ($V = -1$). Intense emission bands and vanishing Stokes shifts in the aggregate are fully in line with J-aggregate behavior. The redshift of absorption (and emission) bands observed for the dyes in the left and

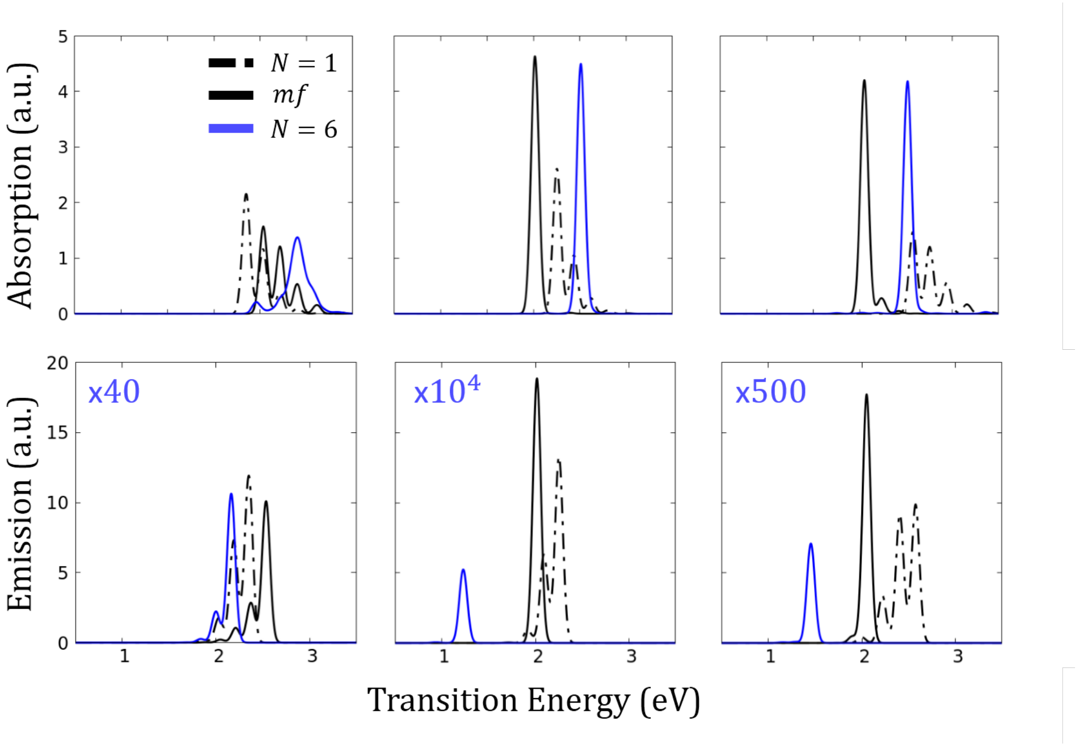

Figure 2.4: H aggregate, $V = 1$, $\varepsilon_v = 0.4$, $\omega_v = 0.17$: top and bottom panel show calculated absorption and fluorescence spectra. Intensities per molecules are reported in arbitrary units. The weak fluorescence spectra of the aggregate are multiplied by the factor shown in the figure. Left panels refer to a system with $z_0 = 0.8$, corresponding to an ionicity for the isolated dye $\rho = 0.19$ that deacreses in the mf approximation to $\rho = 0.17$. Middle panels: $z_0 = -0.3$, gas phase $\rho = 0.64$, mf $\rho = 0.50$. Right panels: $z_0 = -0.6$, gas phase $\rho = 0.76$, mf $\rho = 0.61$.

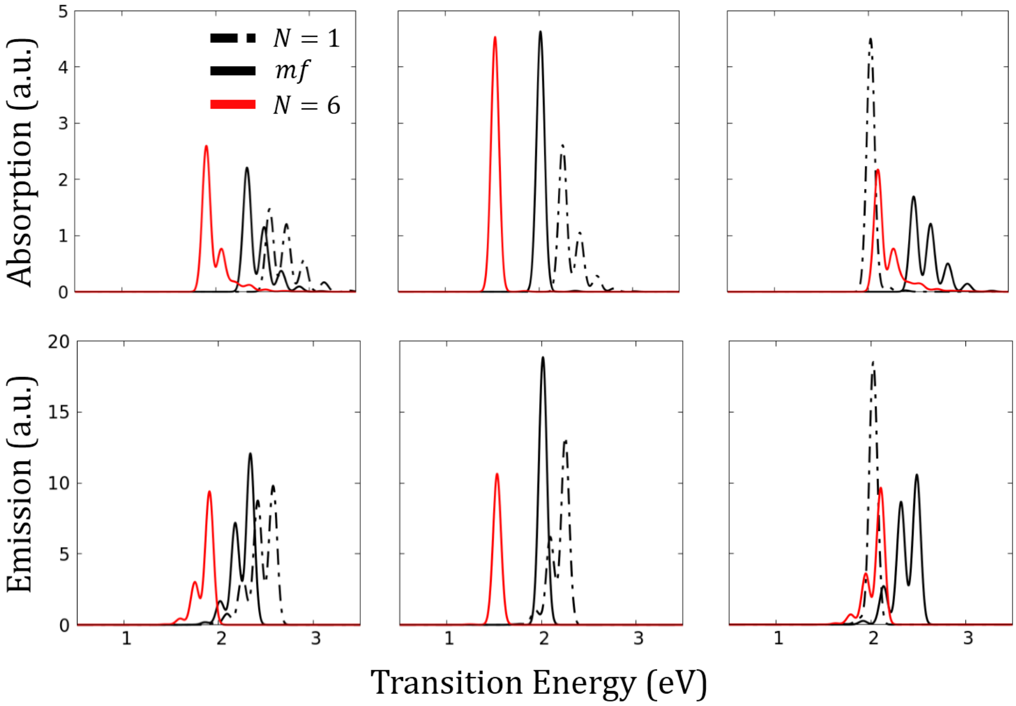

Figure 2.5: J aggregate, $V = -1$, $\varepsilon_v = 0.4$, $\omega_v = 0.17$: top and bottom panel show calculated absorption and fluorescence spectra. Intensities per molecules are reported in arbitrary units. Left panels refer to a system with $z_0 = 1.0$, corresponding to an ionicity for the isolated dye $\rho = 0.15$ that increase in the mf approximation to $\rho = 0.21$. Middle panels: $z_0 = 0.7$, gas phase $\rho = 0.21$, mf $\rho = 0.50$. Right panels: $z_0 = 0.3$, gas phase $\rho = 0.36$, mf $\rho = 0.82$.

middle panels of Fig. 2.4 are again in line with a J-aggregate behavior. The most striking results is however recognized again for the most polar molecule ($\rho = 0.36$ in the gas phase) in the right panels of Fig. 2.4: here in fact the exciton band moves to the blue with respect to the gas-phase molecule. But again this anomalous behavior is simply related to the choice of a wrong starting point. In the aggregate, the mf solution of the problem drives the molecule deep in the ionic regime with $\rho$= 0.82. This implies a large blue shift of the absorption and fluorescence bands, so that, when taking as reference the gas phase molecule, an apparent blue-shift of the exciton band is observed, that actually corresponds to a red-shift when the proper reference is considered, in line with the attractive nature of the interactions. We also notice that for the zwitterionic system, when the wrong reference state is considered, the intensity of the transitions (both absorption and fluorescence) decreases and the vibronic structure becomes more prominent, in striking contrast with the J-nature of the aggregate. This inconsistency is however quite naturally solved if the proper mf reference is considered: in all cases the spectral intensity increases when going from the mf dye to the aggregate, while the vibronic structure becomes less and less prominent. Quite interestingly, results in the central panel fo Fig. 2.4 refer to a dye with ionicity $\rho = 0.16$ in the gas phase that is driven to the cyanine limit, $\rho = 0.50$ when embedded in the aggregate. Once again, in the cianine limit the vibronic structure of absorption and fluorescence bands disappears.

### Medium and Strong Coupling

We will now address the cases of medium and strong coupling. Fig. 2.4 show absorption spectra calculated for H-aggregates in the medium ($V = 1.6$) and strong-coupling ($V = 2.0$) regimes. It turns out that $N_e = 4$ is the minimum number of exciton states needed for convergence, $N_e = 3$ results are totally untenable, with the only exception of the systems that in the mf approaximation have $\rho = 0.5$. In these conditions in fact all terms in Eq.2.18 proportional to $1 - 2\rho$ vanish. Accordingly, the vibronic structure disappears, as discussed above, as well as all terms related to the mesomeric dipole moment. For the electronic part, the Hamiltonian in the $\rho = 0.5$ limit reduces to that relevant to non-polar aggregates and most of the anomalous effects associated with aggregates of polar and polarizable dyes are washed out. Once convergence is reached, finite size effects are marginal for largely neutral dyes, as well as for dyes in the cyanine limit, but become relevant for zwitterionic dyes.

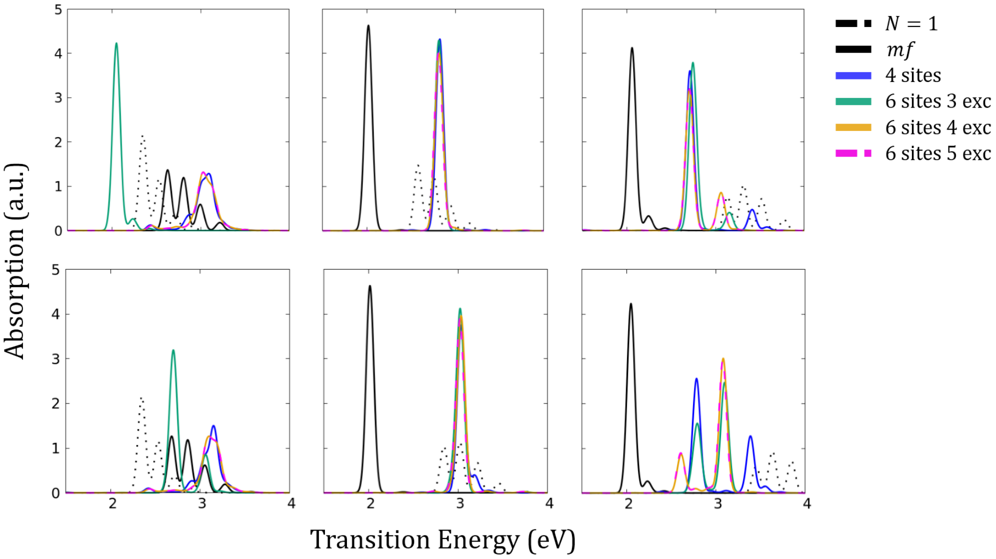

Figure 2.6: H aggregate absorption spectra. All results refer to a system with $\epsilon_v = 0.4$ and $\omega_v = 0.17$. Top panels show results for $V = -1.6$, from left to right: $z_0 = 0.8$, gas phase $\rho = 0.21$, mf $\rho = 0.15$; $z_0 = -0.6$, gas phase $\rho = 0.84$, mf $\rho = 0.5$; $z_0 = -1.0$, gas phase $\rho = 0.9$, mf $\rho = 0.62$. Bottom panels show results for $V = -2.0$, from left to right: $z_0 = 0.8$, gas phase $\rho = 0.21$, mf $\rho = 0.14$; $z_0 = -0.8$, gas phase $\rho = 0.88$, mf $\rho = 0.5$; $z_0 = -1.2$, gas phase $\rho = 0.92$, mf $\rho = 0.61$. For $N = 4$ the full electronic basis is considered, $N_e = 4$.

More interesting is the case of J-aggregates, where electrostatic intermolecular interactions lead to intriguing phenomena.[53, 62] Fig. 2.7 shows absorption and fluorescence spectra calculated for a system with $V = -1.6$, corresponding to the curve in Fig. 2.2 that marks the boundary between the normal (weak coupling) and the bistable (strong coupling) regime. Much as in the weak case, the apparently anomalous behavior observed when comparing aggregate spectra with spectra calculated for the isolated dye are relieved if the proper reference system is considered, corresponding to the mf solution. In all cases in fact the aggregate spectrum is red-shifted with respect to the relevant mf spectrum. The most important difference with respect to the weak coupling is the appearance of finite size effects, with $N = 6$ results differing from $N = 4$, pointing to excitons with large delocalization. Moreover, to get convergence for $N = 6$ at least $N_e = 4$ is needed (see Appendix A) in sharp contrast with the weak coupling case. Quite interestingly, finite size effects are marginal for the system described in middle column of fig. 2.7 where the mf ionicity is 0.5. As discussed above, in this limit, the vanishing of terms proportional to $1 - 2\rho$ not only kills the main vibronic coupling term, but also reduces the electronic part of the Hamiltonian to that of aggregates of non-polar dyes.

This is even more evident in the strong coupling limit in fig. 2.8, showing spectra calculated for $V = -2.0$. Similar considerations apply as in the medium-coupling regime, but in this case $N = 6$ results do not converge until the maximum number of excitons $N_e = 6$ is accounted for in the calculation, or in other terms, the complete electronic basis is considered (see Appendix A). This immediately tells us that the exciton-exciton interaction term (the first term in the last line of Eq.2.18, lowers the energy of multiexciton states that get mixed with the lowest excited states giving a sizable multiexcitonic character to the state, as extensively discussed in refs. [53, 62] Again, this term vanishes for a system with a mf ionicity $\rho = 0.5$, so that for this system (middle panel of fig. 2.8) the $N = 6$ results already converge at $N_e = 3$.

### 2.2.7 Discussion

Extending a previous work[53] to account for molecular vibrations, as needed to properly address spectral bandshapes, a two-step approach is introduced for the description of optical spectra of aggregates of polar and polarizable molecules. The first step is the definition of the proper reference state as the mf solution of the problem. Basically, the ground state polarity of each dye is self-consistently defined by the polarity of the surrounding dyes, leading to increased polarity for attractive intermolecular interactions and reduced polarity for repulsive interactions. Of course all molecular properties (including transition frequencies and dipole moments) are affected by this variation. These mf states define the proper reference states for the exciton model. The molecular geometry is also affected by the molecular polarity and the correct reference state for the vibrational problem is defined via a Lang-Firsov transformation that simply translates the origin of the vibrational coordinates to the equilibrium position relevant to the charge distribution of the molecule inside the aggregate. Since molecular vibrations in turn affect the molecular polarity, this leads to another self-consistent interaction. While this may look as a difficult problem, it boils down to a simple self-consistent diagonalization of a two by two Hamiltonian if the molecules are described in an essential state picture.[77, 55]

The essential state model adopted here has been extensively validated against experiment and describes in a very effective way the low-energy spectral properties of push-pull dyes accounting for environmental effects in solution[68, 78, 79] and aggregates[80, 55], films[81] and crystals.[72, 77] In the context of this work, however, we underline that the model relies on similar approximation as the standard exciton model, accounting for a single electronic excitation and a single vibrational mode per molecule. At variance with the standard exciton model, however, the proposed model fully accounts for the molecular polarizability and for the dependence of the ground and excited state molecular geometry on the molecular polarity.

Once the proper reference state is defined, several interaction terms are recognized in the Hamiltonian that can be classified as excitonic, when conserving the exciton number, and ultraexcitonic when mixing states with a different number of excitons.[53] The vibrational coupling lead to an excitonic term that corresponds to the Condon coupling in the exciton model, but turns out proportional to $1-2\rho$, and therefore vanishes in system whose mf ionicity is close to 0.5: in these system the vibronic bandshape is washed out. The ultraexcitonic term exchanges vibrational quanta and excitons and has marginal spectroscopic effects in the weak coupling limit as shown in Fig. 2.9 and 2.10, that compare exact results obtained in the weak and strong coupling regimes for H and J aggregates with those obtained suppressing the non-Condon vibronic coupling in the Hamiltonian in Eq. 2.18. Non-Condon corrections give rise to sizable effects only in the strong coupling regime.

As for excitonic terms originating from electrostatic interactions, we recognize terms $\propto \rho(1-\rho)$, i.e. proportional to the squared transition dipole moment of the mf molecules:

these terms are responsible for the exciton hopping. Other terms appear $\propto (1 - 2\rho)$, i.e. proportional to the mesomeric dipole moment, that account for exciton-exciton interactions. These last terms vanish when the mf molecular ionicity is close to 0.5, and the system reduces to an aggregate of non-polar dyes. The exciton approximation works reasonably well for weak coupling but becomes clearly untenable in the strong coupling regimes (see fig. 2.9 and 2.10).

Indeed, when increasing the coupling, ultraexcitonic terms enter into play with particularly impressive effects in J-aggregates, where bistability regions are observed in the mf solution.[53, 62] Finite size effects become important in these conditions and the exciton basis cannot be reduced to account for just the first few exciton states (up to 3 excitons are enough to get converged results in the weak coupling limit). Indeed, the lowest excited state in these conditions cannot be described, not even approximately, as a state with a single exciton, rather it corresponds to a state where several excited molecules cluster together in a multiexciton state.[53, 62]

## 2.3 Aggregates of non-polar molecules

Aggregates of non-polar dyes are typically described in terms of the exciton model. Specifically, the model assumes that each molecule in the aggregate can be either on the ground $|g\rangle$ or excited $|e\rangle$ state, both states having a negligible permanent dipole moment. Electrostatic intermolecular interaction then only imply transition dipole moments, $\langle g|\hat{\mu}|e\rangle = \mu_t$. Relevant interactions enter the aggregate Hamiltonian in two different terms: an Heitler-London (HL) term that is responsible for the exciton hopping, and a non-HL term that mixes states whose exciton number differs by two units. When intermolecular interactions are much smaller than the exciton energy, one can neglect all terms in the Hamiltonian that mix states with different energy. The non-HL terms are then neglected, leading to the standard exciton model. The HL approximation is very useful and widely adopted as it leads to an enormous reduction of the electronic basis. Indeed, while for the complete model one should account for $2^N$ states ($N$ is the number of molecules in the aggregate) in the HL approximation, as long as one is interested to linear spectral properties, only the subspace with a single exciton is of relevance and the basis has dimension $N$.

In physical terms, imposing the HL approximation amounts to fully neglect the molecular polarizability, imposing that the nature of the molecular ground and excited states is not affected by intermolecular interactions. As it will be discussed below, this approximation, while usually leading to acceptable spectra, leads to some fundamental problem. Specifically the sum rule for the oscillator strength and for the rotational strength in chiral aggregates[82] are broken. In the following, we will see how these issues can be solved relaxing the HL approximation.

### 2.3.1 The model Hamiltonian

We consider a one dimensional array of $N$ non-polar molecules assuming periodic boundary conditions. Each molecule is either in the ground, $|g\rangle$ or excited $|e\rangle$ state, the two states being separated by an energy $\hbar\omega_0$. An internal vibrational coordinate $\hat{q}_i$ is introduced per molecule and the two electronic states are assigned harmonic potential energy surfaces with the same frequency, $\omega_v$, but displaced minima. The strength of the electron-vibration coupling is measured by the vibrational relaxation energy, $\lambda$, that, being related to the Huang-Rhys factor, $S = \lambda/\hbar\omega_v$, can be extracted from the analysis of the absorption or fluorescence bandshape for the isolated dye in solution.[25] The electrostatic interaction between two molecules at sites $i$ and $j$ reads:[50]

$$J_{i,j} = \frac{\mu_t^2}{4\pi\varepsilon d_{ij}^3} D_{ij}, \tag{2.21}$$

where $D_{ij}$ is a geometrical factor that only depends on the relative orientation of the transition dipole moments on sites $i$ and $j$, while $d_{ij}$ is the distance between the two molecular sites. $D_{ij}$ can assume positive values (repulsive interactions) or negative values (attractive interactions). In the following, we will address one-dimensional molecular aggregates with one molecule per unit cell. We will impose periodic boundary conditions as to maintain translational symmetry. In these conditions, intermolecular interactions only depend on the relative distance between molecules and we define $J_m = J_{i,i\pm m}$. Two extreme cases will be considered: (a) nearest-neighbor interactions with $J_1 = J$ and $J_m = 0$ for $m > 1$; (b) unscreened long-range Coulomb interactions with $J_1 = J$ and $J_m = J[\sin(\pi/N)/\sin(m\pi/N)]^3$ for $m > 1$, with $N$ being the number of molecular units.

In either case a single parameter, $J$, measuring the strength of the nearest-neighbor interaction, fully defines the model.

The magnitude of $\mu_t$ is experimentally accessible from the oscillator strength of the $g \rightarrow e$ transition measured for the isolated dye in solution:

$$f_{ge} = \frac{2}{3}\frac{m_e}{\hbar e^2}\omega_0 \mu_t^2, \tag{2.22}$$

where $m_e$ is the electron mass, $e$ the electron charge and $\omega_0$ the frequency of the $g \rightarrow e$ transition. Alternatively, the transition dipole moment can be obtained from quantum chemical calculations, with the added value of getting information about the dipole moment orientation with respect to the molecular frame.

With these definitions, the Hamiltonian for a linear array of $N$ molecules reads:

$$\begin{aligned} \hat{H} &= \sum_i \left[E - \lambda(\hat{a}_i^\dagger + \hat{a}_i)\right]\hat{n}_i + \hbar\omega_v \sum_i \left(\hat{a}_i^\dagger \hat{a}_i + \frac{1}{2}\right) \\ &+ \sum_m J_m(\hat{b}_i^\dagger \hat{b}_{i+m} + h.c.) + \sum_m J_m(\hat{b}_i^\dagger \hat{b}_{i+m}^\dagger + h.c.), \end{aligned} \tag{2.23}$$

where $i$ and $j$ run on the $N$ molecular sites. The operators $\hat{a}_i^\dagger$, $\hat{a}_i$ are the boson operators associated with the harmonic oscillator on site $i$. The operator $\hat{b}_i^\dagger$ creates an excitation on site $i$, by turning the molecule from state $|g\rangle$ to $|e\rangle$, while $\hat{b}_i$ destroys the excitation (these operators obey Paulion algebra as discussed in Section 2.2).

The first term in the above Hamiltonian describes the molecular problem, where $E$ is the vertical excitation energy of the molecule in the aggregate. It may differ from $\hbar\omega_0$, the transition energy in the isolated molecule, due to local field effects, but we will neglect these corrections in the following, setting $E{=}\hbar\omega_0$. The last two terms account for intermolecular interactions: the same interaction $J_m$ is responsible for the hopping of the excitation from site $i$ to $i+m$ (and viceversa) and for the simultaneous creation (destruction) of two excitations on sites $i$ and $i+m$. As mentioned above, the hopping term mixes states with the same number of excitons, i.e. states having the same diagonal energy, while the last term in the above Hamiltonian describes the interaction among states whose energy differs by $2E$ and, in the HL approximation, it is neglected. Of course, the HL approximation works well for $J \ll 2E$.

Before closing this Section, it is instructive to compare the Hamiltonian for non - polar dyes in Eq. 2.23 with the Hamiltonian describing polar and polarizable dyes in

Eq. 2.16. As for the electronic part, the Hamiltonian in Eq. 2.16 reduces exactly to the Hamiltonian for non-polar dyes when $\rho = 0.5$. In these condition in fact, the mesomeric dipole moment, proportional to $1-2\rho$ (see Eq. 2.7), vanishes and the only terms surviving from the intermolecular interactions are those proportional to the squared transition dipole moment $\propto \rho(1-\rho)$. Specifically $J_{ij} = V_{ij}\rho(1-\rho) = V_{ij}/4$. However, it should be noticed that this is just a formal equivalence, as the ground and excited state of the non-polar dye are not in general described as a linear combination of a neutral and a zwitterionic state. This difference shows up most clearly in the vibronic coupling term: in the Hamiltonian for aggregates of polar dyes (Eq. 2.18) in fact the leading Condon term in the electron-vibration coupling exactly vanishes at $\rho = 0.5$, while Condon coupling is undoubtedly observed in non-polar dyes. Indeed, electrostatic intermolecular interactions only depend on the charge distribution in the molecular structure which, in turn, can be reliably described for either polar or non-polar dyes adopting the two-state electronic Hamiltonian described in Section 2.2. However the molecular Hamiltonian defined for DA dyes is not general enough to properly account for vibronic coupling in non-polar dyes.

### 2.3.2 Exact diagonalization approach: calculating absorption and fluorescence spectra

The complete basis needed to describe the coupled electronic and vibrational motion defined by the Hamiltonian in Eq. 2.23, is obtained as the direct product of the electronic basis states, the $2^N$ states where each one of the N molecules can be either in state $|g\rangle$ or $|e\rangle$, times the vibrational basis. In principle, the vibrational basis has infinite dimension as one should account for the (infinite number of) states associated with each one of the $N$ harmonic oscillators residing on each molecular site. Of course as it will be discussed below, the vibrational basis will be truncated to numerically address the problem.

Translational symmetry can be implemented by separately finding the wavevector for the electronic and vibrational states, $k$ and $q$, respectively, and then combining the two to give states with the required total wavevector. To this end, we move the Paulion operators for creating/destroying an exciton to the Fourier space:

$$\hat{b}_j = \frac{1}{\sqrt{N}} \sum_k e^{-ijk} \hat{b}_k, \qquad \hat{b}_j^\dagger = \frac{1}{\sqrt{N}} \sum_k e^{ijk} \hat{b}_k^\dagger, \tag{2.24}$$

and apply the same transformation to the boson operators that create/destroy vibrational quanta:

$$\hat{a}_j = \frac{1}{\sqrt{N}} \sum_q e^{-ijq} \hat{a}_q, \qquad \hat{a}_j^\dagger = \frac{1}{\sqrt{N}} \sum_q e^{ijq} \hat{a}_q^\dagger. \tag{2.25}$$

The Hamiltonian in Eq. 2.23 is rewritten using the transformed operators as follow:

$$\begin{aligned} \hat{H} &= \sum_k \hat{b}_k^\dagger \hat{b}_k \left( E + \sum_m J_m e^{imk} \right) + \hbar\omega_v \sum_q \hat{a}_q^\dagger \hat{a}_q \\ &\quad - \frac{\lambda}{\sqrt{N}} \sum_{k,q} (\hat{a}_q^\dagger \hat{b}_k^\dagger \hat{b}_{k+q} + \hat{a}_{-q} \hat{b}_k^\dagger \hat{b}_{k+q}) \\ &\quad + \frac{1}{2} \sum_{k,m} J_m \left( \hat{b}_k^\dagger \hat{b}_{-k}^\dagger e^{imk} + h.c. \right). \end{aligned} \tag{2.26}$$

The non-HL term (last term of the above equation) mixes electronic states with different number of excitons and different $k$, making the symmetrization procedure cumbersome, so that, for the complete problem we prefer to adopt a similar technique as implemented for dipolar aggregates in the previous Section. Each molecule in the aggregate is represented using 4 bits, one accounting for the electronic excitation and 3 defining the vibrational level. As before, $M_e$, represents the maximum number of molecules simultaneously in the excited state, and $M_v$ the maximum number of total vibrational quanta.

When the HL approximation is adopted the $N$ electronic states with a single exciton are easily combined to give $N$ linear combinations in the reciprocal space. The total wavevector $K$ is calculated for each state as the sum of the electronic wavevector plus the vibrational contribution $K = k + \sum_q n_q q$, where $n_q$ counts the number of vibrational quanta in the vibrational mode with wavevector $q$.

The Hamiltonian is finally diagonalized in the relevant subspaces to get numerically exact non-adiabatic vibronic eigenstates that describe the combined electronic and vibrational motion in the aggregate. To calculate optical spectra we write the explicit expression for the dipole moment operator of the aggregate, and considering aligned dipoles as to avoid vectorial sums, we get:

$$\hat{\mu} = \mu_0 \sum_i (\hat{b}_i^\dagger + \hat{b}_i) = \mu_0 \sqrt{N}(\hat{b}_{k=0}^\dagger + \hat{b}_{k=0}). \tag{2.27}$$

Spectra are calculated adopting the expression for $\sigma_{abs}$ and $I_{fluo}$ in Eq. 2.19 and 2.20. We underline that in the standard exciton model, due to the decoupling of the vacuum state $|...ggg...\rangle$ with the states with one (or more) excitons, the eigenstates and hence the transition dipole moments are fully independent on the bare exciton frequency, $\omega_0$. However, absorption (fluorescence) spectra acquire a dependence on $\omega_0$, or more precisely on the specific frequency of the electronic transitions, due to the $\omega$ ($\omega^3$) prefactor in the expression for absorption (fluorescence).

The calculation of fluorescence spectra requires some care to single out the long-lived state out of the excited states manifold. This state corresponds to the lowest excited state in the electronically excited manifold (we assume that temperature is low enough as to have a sizable population only on the lowest excited state). In the standard exciton model, since the Hamiltonian is diagonalized in the single-exciton manifold, the fluorescent state coincides with the lowest energy state. Depending on the sign of intermolecular interactions the fluorescent state is found in either the $K = 0$ subspace ($J < 0$, J-aggregates) or in the $K = K_{max}$ subspace ($J > 0$, H-aggregates). When relaxing the HL approximation, the eigenstates also contain the ground state vibronic manifold. We therefore recognize the fluorescent state as the lowest energy state in either the $K = 0$ or $K_{max}$ subspace with a number of excitons close to 1. The fluorescence spectrum is calculated using Eq. 2.20 where the sum runs on all eigenstates (including the ground state) having a lower energy than the fluorescent state $|F\rangle$ and being located in the same subspace (either $K = 0$ or $K_{max}$) as the fluorescent state. Since in the complete model the eigenstates also include the vibronic manifold of the ground state, Eq. 2.20 can be used without further analysis. In the standard exciton model instead the $|E\rangle$ states in the above equation corresponds to the vibronic eigenstates in the ground state manifold and must be explicitly written as the product of the electronic ground state $|...ggg...\rangle$ (the zero exciton state, a state with $k = 0$) times the states of the harmonic oscillators (taking into account only states with $\sum_q n_q q = 0, K_{max}$, depending on the relevant subspace).

### 2.3.3 Exact results on finite size systems: validating the Heitler-London approximation

Fig. 2.11 shows selected results for typical model parameters. Specifically, we consider only nearest neighbor interactions for $\hbar\omega_0$=2 eV and $\hbar\omega_v$=0.17 eV, corresponding to a system with an electronic excitation in the visible and a mid-IR vibrational mode. A medium-large vibrational coupling is considered, setting $\lambda$=0.17 eV, corresponding to a monomer spectrum peaking at the 0-1 vibronic line (results for weaker and stronger coupling are also shown in Appendix A). The intermolecular interaction strength is fixed to $|J|$=0.255 eV, roughly a tenth of the exciton bare energy, $\hbar\omega_0$. We estimate that this $J$ value corresponds, for a typical oscillator strength $f$=1 of the monomer, to an intermolecular distance $d \sim 7$ Å, that would reduce to $\sim 3.5$ Å accounting for a screening factor $\sim 2$.

Results in the figure are obtained for $N$=6, truncating the vibrational basis to $M_v$=6, and refer to positive $J$ (H-aggregates) in the upper panel and to negative $J$ (J-aggregates) in the lower panel. In each panel, the dash-dotted line shows the monomer spectrum and the continuous curves refer to results obtained truncating the number of excitons to $M_e$=1-4, as specified in the legend. The first observation is that results for $M_e$=3 and 4 are superimposed: accounting for up to 3 excitons leads to nominally exact results.

Results for $M_e$=1 of course coincide with those obtained in the standard exciton model. Apparently the HL approximation works very well to estimate the position of the absorption band and reasonably well for the band-shape (small deviations are observed in H-aggregates), but it fails to reproduce the intensity of the spectrum. Calculated spectra show a non-monotonous behavior with increasing $M_e$: while for $M_e$=1 the position of the absorption band is properly calculated (even if we are off with the intensity), $M_e$=2 results are off with the frequency, but improve on the intensity. This immediately suggests that the HL approximation (corresponding to $M_e$=1 results in the figure) gives good results for the band position due to error cancellation. The non-HL term in Eq. 2.23 in fact mixes states with a number of excitons differing by 2: the energy of the ground state is lowered due to the non-HL mixing with two-exciton states by an amount similar to the stabilization of one-exciton states due to the mixing with the three-exciton states. Accordingly, the frequency of the observed transition is marginally affected by the non-HL terms. Of course the transition frequency calculated for $M_e$=2 is overestimated since it accounts for the stabilization of the ground state, but not for stabilization of the excited states.

Spectra calculated in the HL approximation overestimate the intensity of H-aggregates and underestimate the intensity of J-aggregates. This interesting result deserves some discussion. Since in the HL approximation the excited states reached upon absorption are linear combinations of one-exciton states, the total squared transition dipole moment in an aggregate of $N$ molecules is equal to the total squared transition dipole moment of $N$ non-interacting molecules. This immediately points to an internal inconsistency of the exciton model in its standard implementation. As it is well known (see also the detailed analysis in Appendix A), the total oscillator strength of a system can always be related to a ground state property:

$$F = \sum_E f_{EG} = \frac{2}{3}\frac{m_e}{\hbar e^2}\sum_E \omega_{EG}\mu_{EG}^2 = -\frac{im_e}{3\hbar e^2}\langle G|[\hat{\mu},\hat{v}]|G\rangle, \tag{2.28}$$

where $i$ is the imaginary unit and the velocity dipole operator is defined as:

$$i\hbar\hat{v} = [\hat{\mu},\hat{H}]. \tag{2.29}$$

In the HL approximation the aggregate ground state is the same as the ground state of $N$ non-interacting monomers, so that the sum-rule in Eq.2.28 would impose the conservation of the total oscillator strength (per molecule) when going from the monomer to the aggregate. However, in the HL approximation the total dipole moment is conserved, therefore in the standard exciton model the oscillator strength for J-aggregates (having a red-shifted transition with respect to the monomer) is underestimated, while it is overestimated for H-aggregates (having a blue-shifted absorption).

Of course the sum rule is strictly obeyed in the complete exciton model. Specifically, the relevant commutator in Eq.2.28 is (see the derivation in Appendix A):

$$[\hat{\mu},\hat{v}] = \frac{1}{i\hbar}\mu_0^2\sum_i[\hbar\omega_0 - \lambda(\hat{a}_i^\dagger + \hat{a}_i)](4\hat{n}_i - 2), \tag{2.30}$$

so that

$$F = \frac{2}{3}\frac{m_e \mu_0^2}{\hbar^2 e^2}\langle G|\sum_i [\hbar\omega_0 - \lambda(\hat{a}_i^\dagger + \hat{a}_i)](1-2\hat{n}_i)|G\rangle. \tag{2.31}$$

We explicitly verified that the total oscillator strength calculated for the complete model as the sum of the oscillator strengths of the individual transitions coincides with the ground state expectation value in the above equation. The vibrational contribution in the above expression simply renormalizes the bare excitation frequency, $\hbar\omega_0$, a marginal correction as the ground state expectation value of $(\hat{a}_i^\dagger + \hat{a}_i)$ is negligible. Neglecting this correction, the oscillator strength $F$ in Eq. 2.31 is made up of two terms: the first term coincides with the oscillator strength of $N$ non-interacting molecules (see Eq. 2.22), while the second term describes the correction to the oscillator strength due the finite weight in the ground state of states with a finite exciton number. We stress that the HL approximation leads in the standard exciton model to sizable deviations of absorption intensity from exact results already for $J$ values one order of magnitude smaller than the unperturbed exciton frequency. This very general result must be accounted for when addressing hypo- and hyperchromism in molecular aggregates: relaxing the HL approximation in fact naturally explains hyperchromic effects in J-aggregates and hypochromic effects in H-aggregates.

Calculated emission spectra for the same systems as in Fig. 2.11 are shown in Fig. 2.12 (results for long-range intermolecular interactions and for different values of $\lambda$ are shown in Appendix A). The first observation is the intensity of the emission for H aggregates being lower than that of J-aggregates by two orders of magnitude (of course we are referring to the nominal fluorescence intensity, not taking into account non-radiative deactivation pathways). The fluorescent state in H-aggregate is in the $K = K_{max}$ subspace and is therefore a dark state. Indeed it acquires a finite (albeit weak) intensity due to vibronic coupling and, specifically, due to the presence of $K = K_{max}$ states in the vibronic manifold of the ground state. Because the zero-phonon line is forbidden by symmetry, the H-aggregate emission is even more red-shifted than the emission of the J-aggregate. As for the quality of the results obtained in the HL approximation, the position and shape of the fluorescence band are well approximated while, in line with the above discussion, the emission intensity is overestimated for H-aggregates and underestimated for J-aggregates.

### 2.3.4 Testing approximation schemes

Exact diagonalization approaches are limited to small aggregates, up to 7 sites for the complete model and up to 10 sites in the HL approximation. The electronic basis is comparatively small, growing with $N$ in the HL approximation and as $2^N$ in the complete model. Indeed the basis blows up because of the vibrational states: accounting for just three vibrational quanta per site would multiply by a $3^N$ factor the basis dimension. It is therefore very important to discuss approximation schemes to cut the basis dimension and particularly so for the vibrational states. Indeed the HL electronic basis is already very small, while we already discussed how the electronic basis in the complete model can be reduced by fixing a maximum number of excitons ($M_e = 3$ seems to work pretty well in most cases of interest in this study, even if this approximation is untenable for clusters of polar and polarizable dyes in medium or strong coupling regimes.

Recently,[55] discussing J-aggregates of polar dyes, we realized that for largely delocalized excitons only the vibrational modes in the close proximity of the center of the Brillouin zone are effectively coupled to the electronic degrees of freedom so that, instead of accounting for $N$ local harmonic oscillators, reasonable results are obtained accounting for the single oscillator with $q = 0$. This of course leads to an enormous reduction of the basis dimension. The Hamiltonian in Eq. 2.26 shows that accounting for just the $q = 0$ mode one obtains a similar coupling Hamiltonian as for the isolated molecule, but with the strength of the coupling reduced to $\lambda/\sqrt{N}$. As a result, in this approximation the same bandshape is calculated for J and H aggregates, as shown in the top panels of Fig. 2.13, where we show absorption spectra calculated in the HL approximation for the same model parameters as in Fig. 2.11.

A full decoupling of the $q = 0$ vibrational mode is expected in the infinite chain limit and a washing out of the vibronic structure in either J or H aggregates of infinite size. Adding the two nearest modes to the $q = 0$ mode in the Brillouin zone (middle panels of Fig. 2.13) improves the agreement and adding 2 more modes (for a grand total of 5 delocalized vibrations, bottom panels) gives very good results for J aggregates and an acceptable agreement for H-aggregates. Cutting vibrational modes in the Fourier space works in principle for the complete as well as for the standard exciton model, but, apart from the simplest case where only the $q = 0$ mode is accounted for, the approach is difficult to implement in the complete model. Moreover this approximation is expected to work well for largely delocalized excitons. Of course for localized excitons or in the presence of disorder the approach could only work if many modes (possibly all) in the reciprocal space are introduced, making the approximation useless.

A useful and widely adopted approach to reduce the vibrational space is the so-called *few-particle approximation*,[83, 84] that has been extensively applied by Spano[46, 47] in the 2-particle approximation (2PA) or 3-particle approximation (3PA) flavors. It works in the real space, so that it does not require a symmetric or ordered system, but only applies in the HL approximation where all relevant basis states have a single exciton. In the 2PA approximation, the basis is cut imposing a maximum number $n_e$ of vibronic excitations on the electronically excited states (notice that these vibronic states refer to the *displaced* harmonic oscillator as relevant to the electronically excited state). Moreover a maximum number of vibrational quanta $n_v$ can be present in just a single additional site, different from the site bearing the exciton.

In the three particle approximation (3PA), one accounts for vibrational excitations occurring on up to two sites. Two different approximation schemes are possible for both 2PA and 3PA, a small-range (sr) scheme, where vibrational excitations are only allowed in the nearest sites of the site bearing the exciton (Fig. 2.15), or a long-range (lr) scheme, where vibrational sites can be spread all over the aggregate. Of course the 2PA-sr or the 3PA-sr only apply when the exciton model accounts for nearest neighbor interactions, while one must resort to lr-schemes when accounting for long-range electrostatic interactions.

To be specific, the 2PA basis set is:

$$|\psi_{2PA}\rangle = |n, \tilde{\nu}, \nu_l\rangle, \quad l \neq n, \tag{2.32}$$

where $n$ marks the site where the exciton resides and $\tilde{\nu}$ counts the number of vibrational quanta in the displaced oscillator associated with the same site. The numbers $\nu_{l\neq n}$ count the vibrational quanta in the undisplaced harmonic oscillator on site $l$. In the sr flavor of 2PA, $l = n \pm 1$, while in the lr flavor, $l$ can assume any value different from $n$. The diagonal energy of the 2PA states is easily calculated as $\hbar\omega_0 + (\tilde{\nu} + \nu_l)\hbar\omega_v$. Off diagonal matrix elements, accounting for the interaction between different sites, are:

$$\langle n,\tilde{\nu},\nu_l|\hat{H}|m,\tilde{\mu},\mu_k\rangle = Jf_{\tilde{\nu},\mu_n}f_{\tilde{\mu},\nu_m}\prod_{i\neq n,m}\delta_{\nu_i,\mu_i}, \tag{2.33}$$

where $f_{\tilde{i},j}$ is the Franck-Condon factor measuring the overlap between the vibrational level of excited state $\tilde{i}$ and vibrational level of ground state $j$. Finally, the transition dipole moment is calculated as follows:

$$\mu_i^{trans} = \langle G|\hat{\mu}|\psi_i\rangle = \sum_{n,\tilde{\nu}} c_{n,\tilde{\nu}}\langle G|\hat{\mu}|n,\tilde{\nu},0\rangle = \sum_{n,\tilde{\nu}} c_{n,\tilde{\nu}}\mu_0 f_{\tilde{\nu},0}. \tag{2.34}$$

Moving to the 3PA, the relevant basis set reads $|\psi_{3PA}\rangle = |n,\tilde{\nu},\nu_l,\nu_{l'}\rangle,\quad l,l' \neq n$. Accordingly, the diagonal energy is $\hbar\omega_0 + (\tilde{\nu}+\nu_l+\nu_{l'})\hbar\omega_\nu$, while the Hamiltonian off-diagonal matrix elements are:

$$\langle n,\tilde{\nu},\nu_l,\nu_{l'}|\hat{H}|m,\tilde{\mu},\mu_k,\mu_{k'}\rangle = Jf_{\tilde{\nu},\mu_n}f_{\tilde{\mu},\nu_m}\prod_{i\neq n,m}\delta_{\nu_i,\mu_i}. \tag{2.35}$$

Fig. 2.16 compares absorption spectra calculated via exact diagonalization and with the 2PA-sr and 3PA-sr for an aggregate of 10 molecules, described by the standard exciton model, with increasing strength of nearest-neighbor interactions, $J$. For J-aggregates the 2PA and 3PA approximations work pretty well up to medium-large interactions, but for H-aggregates, the approximation is poor already for interactions of medium strength. Similar results hold true for emission spectra in Fig. 2.17. Moving to 2PA-lr or 3PA-lr does not change the picture, as expected.

The lr extensions of the 2PA and 3PA approaches has to be invoked for systems where long-range Coulomb interactions are accounted for. However the 3PA-lr basis is very large, making it impossible to deal with aggregates with more than 6 sites. Therefore Fig. 2.18 and Fig. 2.19 compare exact and 2PA-lr results for absorption and emission spectra, rescpectively, of 10 site aggregates with long-range intermolecular interactions.

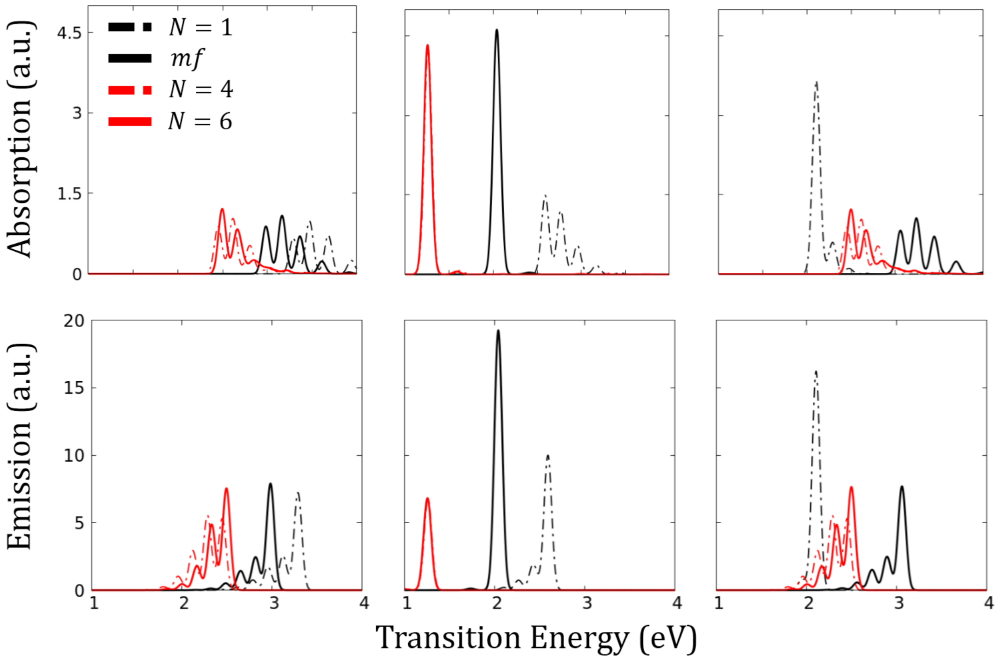

Figure 2.7: J aggregate, $V = -1.6$, $\epsilon_v = 0.4$, $\omega_v = 0.17$: top and bottom panel show calculated absorption and fluorescence spectra. Intensities per molecules are reported in arbitrary units. Left panels refer to a system with $z_0 = 1.5$, corresponding to an ionicity for the isolated dye $\rho = 0.09$ that increases in the mf approximation to $\rho = 0.10$. Middle panels: $z_0 = 1.0$, gas phase $\rho = 0.16$, mf $\rho = 0.50$. Right panels: $z_0 = 0.5$, gas phase $\rho = 0.33$, mf $\rho = 0.90$. For $N = 4$ the full electronic basis is considered, $N_e = 4$. For $N = 6$ only converged results are shown with $N_e = 4$

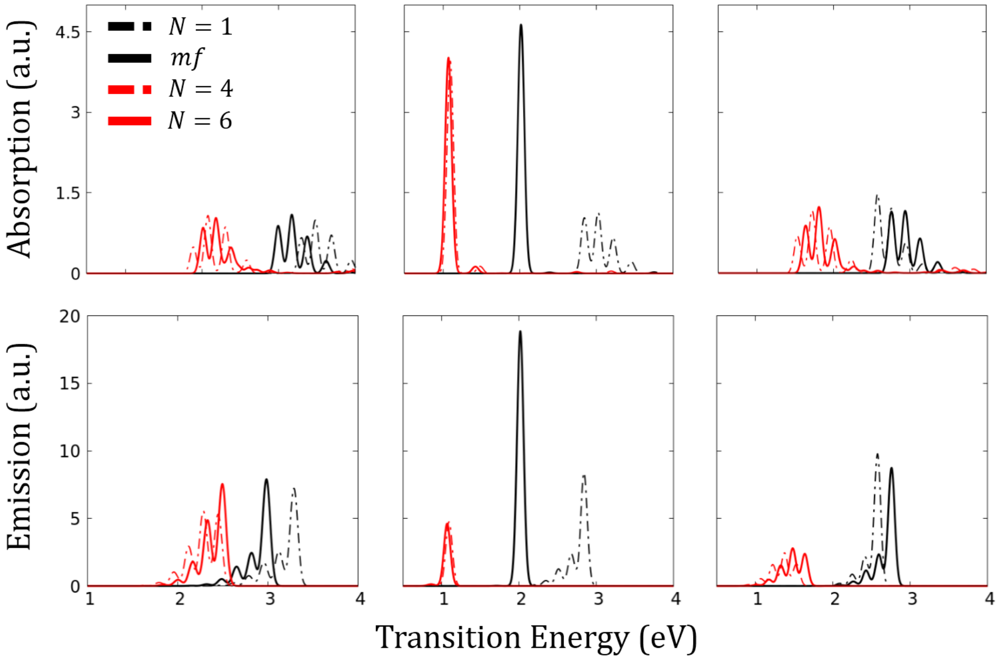

Figure 2.8: J aggregate, $V = -2.0$, $\epsilon_v = 0.4$, $\omega_v = 0.17$: top and bottom panel show calculated absorption and fluorescence spectra. Intensities per molecules are reported in arbitrary units. Left panels refer to a system with $z_0 = 1.5$, corresponding to an ionicity for the isolated dye $\rho = 0.09$ that increases in the mf approximation to $\rho = 0.11$. Middle panels: $z_0 = 1.2$, gas phase $\rho = 0.12$, mf $\rho = 0.50$. Right panels: $z_0 = 1.0$, gas phase $\rho = 0.16$, mf $\rho = 0.87$.For $N = 4$ the full electronic basis is considered, $N_e = 4$. For $N = 6$ only converged results are shown with $N_e = 4$

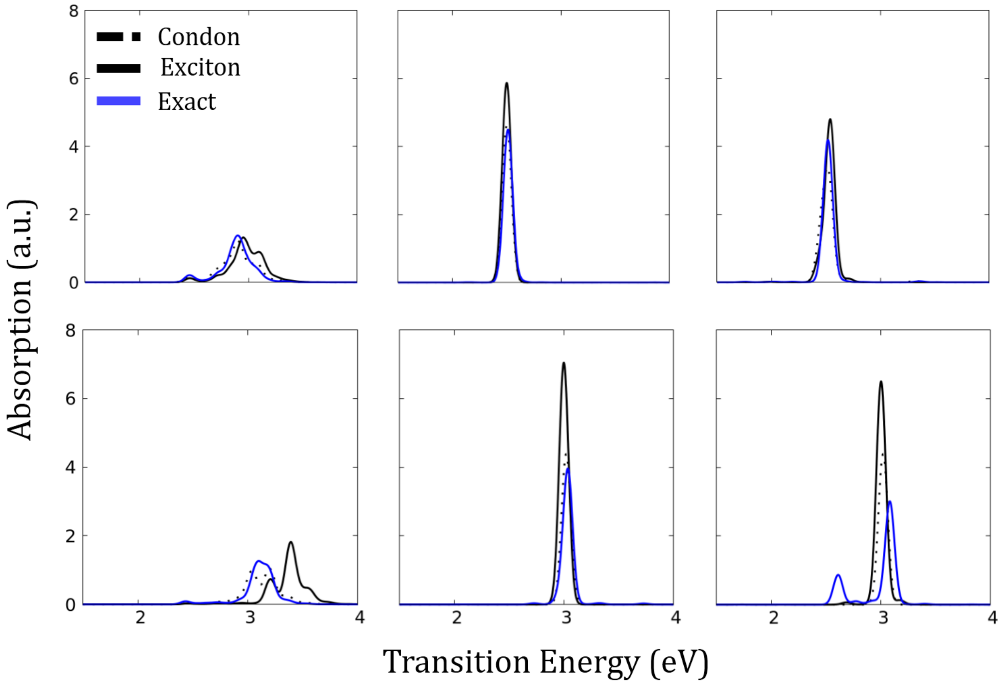

Figure 2.9: H aggregates with $N = 6$. Top panel show weak-coupling results, $V = 1$ for the same values of model parameters as in Fig. 2.4; bottom panels show results for strong coupling, $V = 2$, for the same parameters as in the bottom panels of Fig. 2.6. In all panels blue lines show converged results for the total Hamiltonian, dashed black curves show results obtained neglecting the non-Condon electron-vibration coupling term, continuous black lines show results for the exciton model, i.e. suppressing all ultraexcitonic terms in the Hamiltonian.

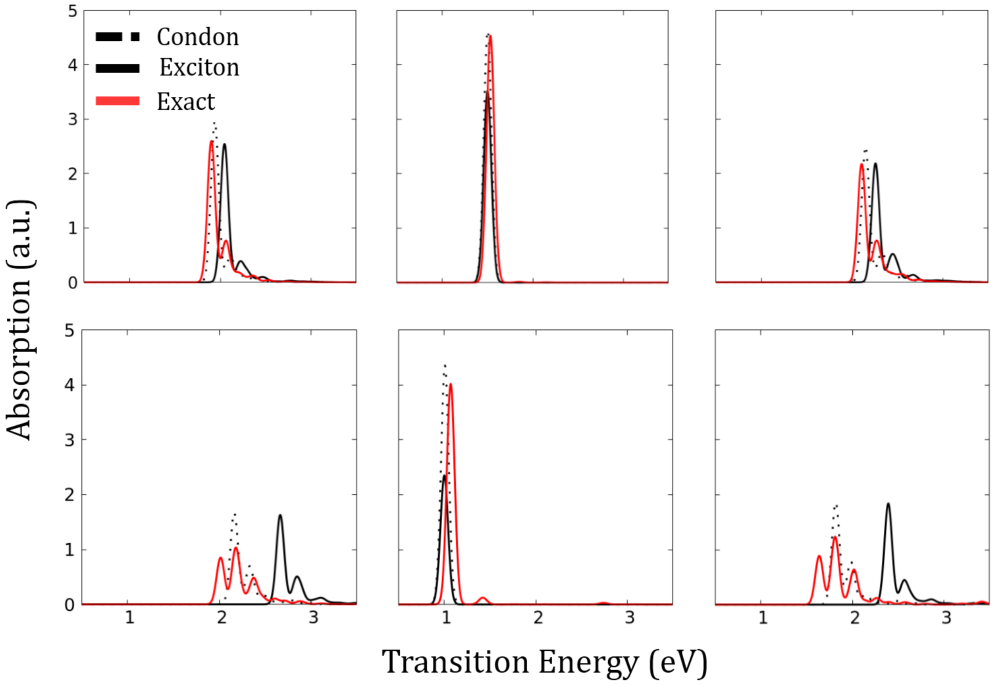

Figure 2.10: J aggregates with $N = 6$. Top panel show weak-coupling results, $V = -1$ for the same values of model parameters as in Fig. 2.5; bottom panels show results for strong coupling, $V = -2$, for the same parameters as in Fig. 2.8. In all panels blue lines show converged results for the total Hamiltonian, dashed black curves show results obtained neglecting the non-Condon electron-vibration coupling term, continuous black lines show results for the exciton model, i.e. suppressing all ultraexcitonic terms in the Hamiltonian.

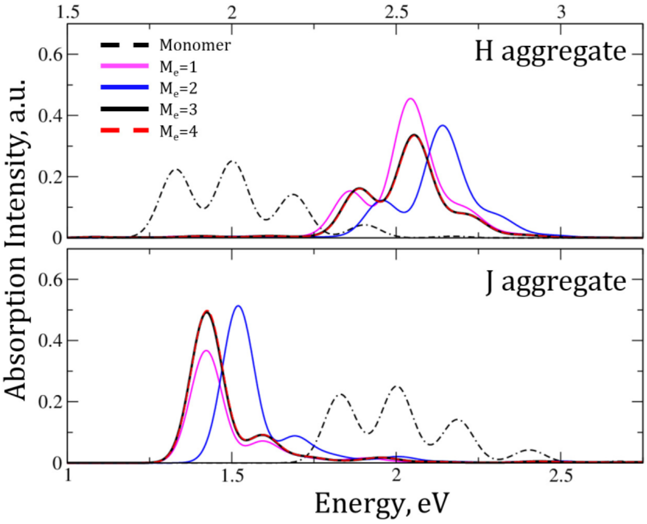

Figure 2.11: Absorption spectra calculated for the complete Hamltonian in Eq.2.23 only accounting for nearest neighbor interactions. Results are obtained for $N$=6, $\hbar\omega_0$= 2.0 eV, $\lambda$=0.17 eV, $\hbar\omega_v$=0.17 eV and $|J|$=0.255 eV. The vibrational basis is truncated setting the maximum number of total vibrational quanta $M_v$=6. The electronic basis is truncated fixing the maximum number of excitons $M_e$ to a value ranging from 1 to 4. Results for $M_e$=1 coincide with those obtained in the HL approximation. Top and bottom panels refer to H-aggregates ($J > 0$) and J-aggregates ($J < 0$), respectively. In both panels the dash-dotted line shows the spectrum relevant to non-interacting molecules (i.e., the monomer limit).

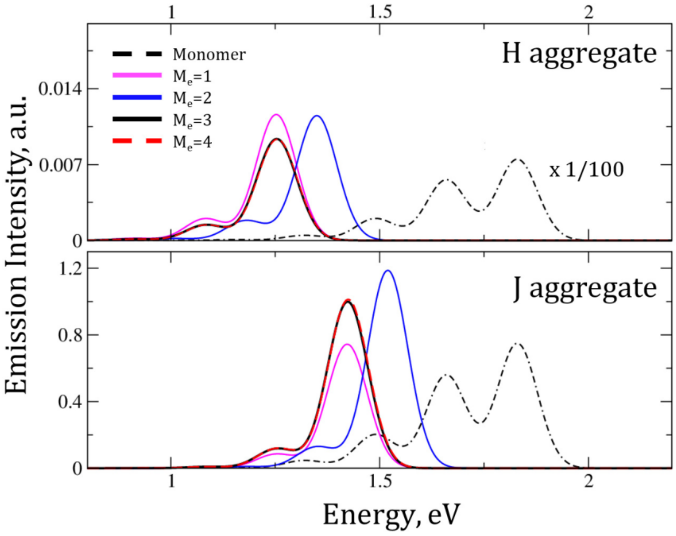

Figure 2.12: Emission spectra calculated for the the same system as in Fig. 2.11

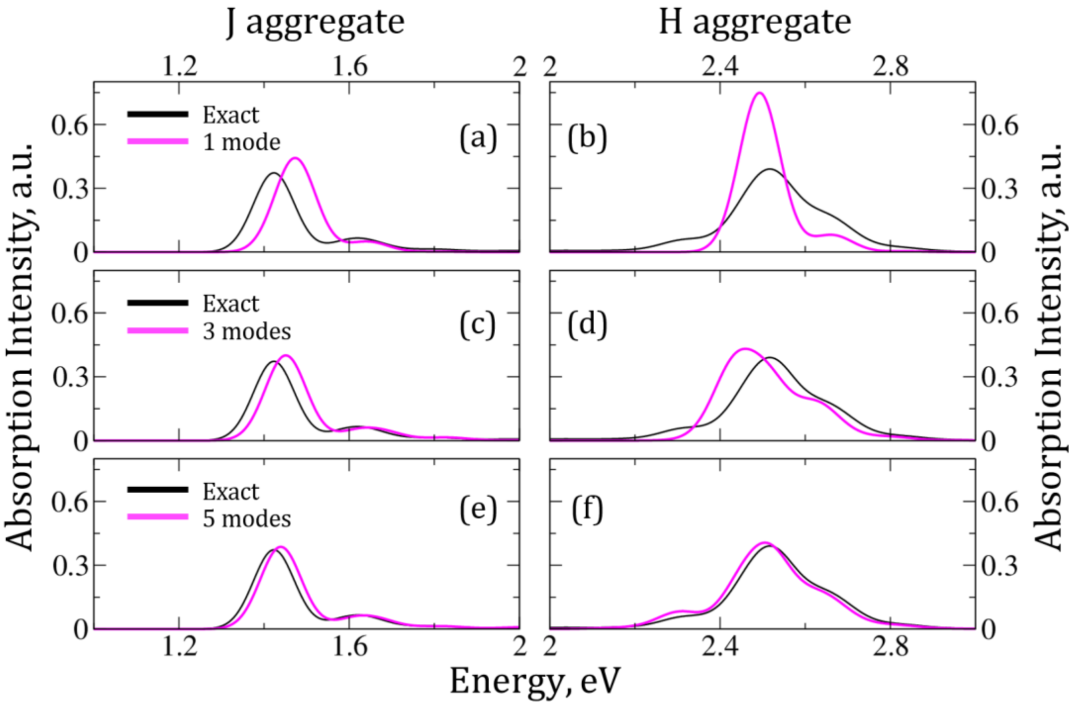

Figure 2.13: Calculated absorption spectra for J and H aggregates (left and right panels, respectively) calculated in the HL approximation for the same model parameters as in Fig. 2.11. Results refer to aggregates of 10 molecules, black lines show numerically exact results, obtained with $M_v = 4$, magenta lines show results calculated only accounting for the $q = 0$ mode (top panels), $q \in \{-\frac{\pi}{5}, 0, \frac{\pi}{5}\}$ (middle panel), $q \in \{-\frac{2}{5}\pi, -\frac{\pi}{5}, 0, \frac{\pi}{5}, \frac{2}{5}\pi\}$ (bottom panels).

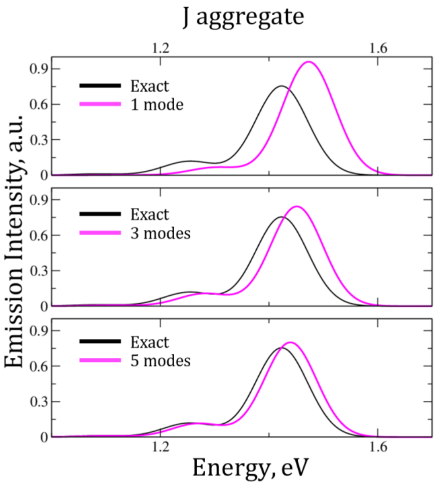

Figure 2.14: Emission spectra calculated for the same system as in left panel of Fig. 2.13.

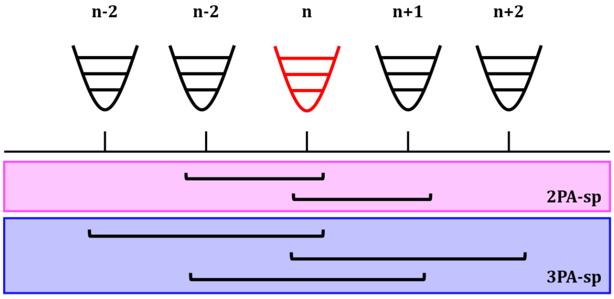

Figure 2.15: Scheme representing the allowed combination of states allowed in the *sr* ansatz. The red oscillator represents the vibronically excited state.

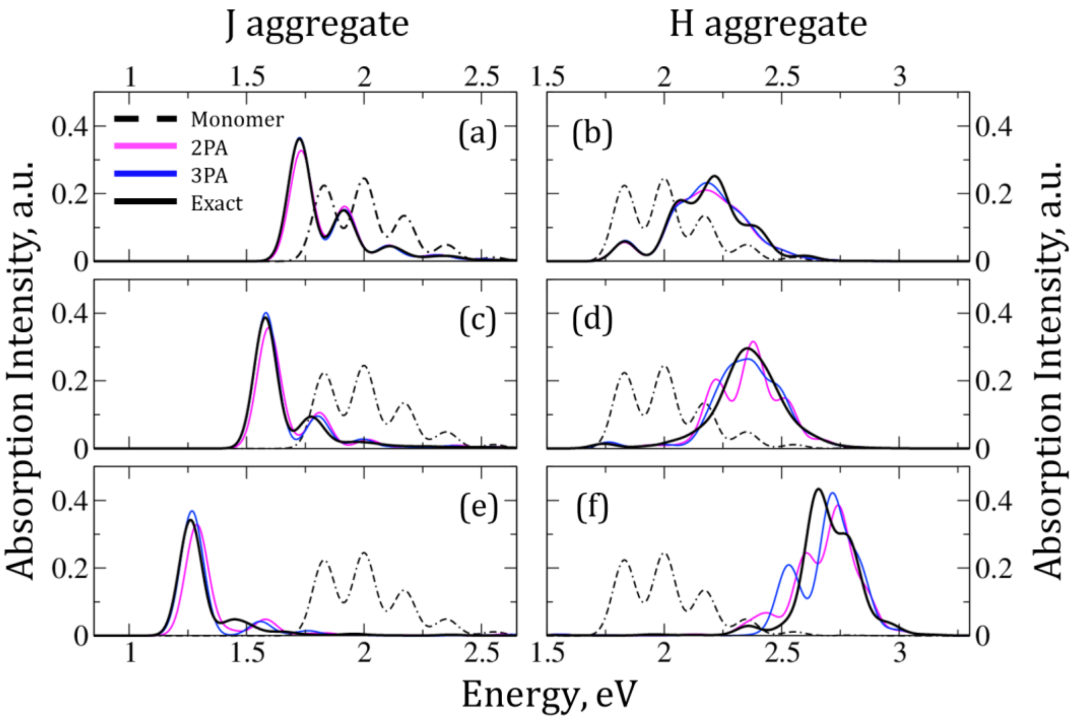

Figure 2.16: Absorption spectra for 2PA-sp, 3PA-sp and exact excitonic models for a 10 molecule aggregate allowing up to 6 phonons in the calculation. Nearest neighbors interactions: panels *a), c), e)* $J$ respectively $-0.085$eV, $-0.17$eV, $-0.34$eV; panels *b), d), f)* $J$ respectively 0.085eV, 0.17eV, 0.34eV. $\hbar\omega_\nu$=$\lambda$=0.17eV. In black dashed line the monomer spectrum is shown for comparison.

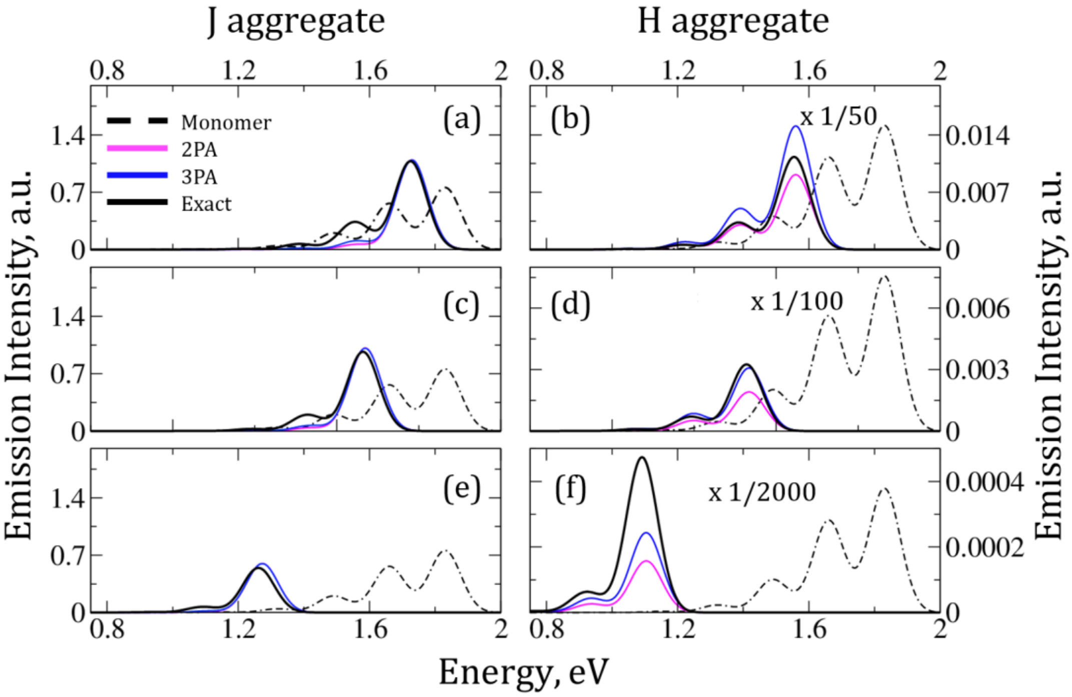

Figure 2.17: Emission spectra for 2PA-sp, 3PA-sp and exact excitonic models. Same parameters used in Fig. 2.16.

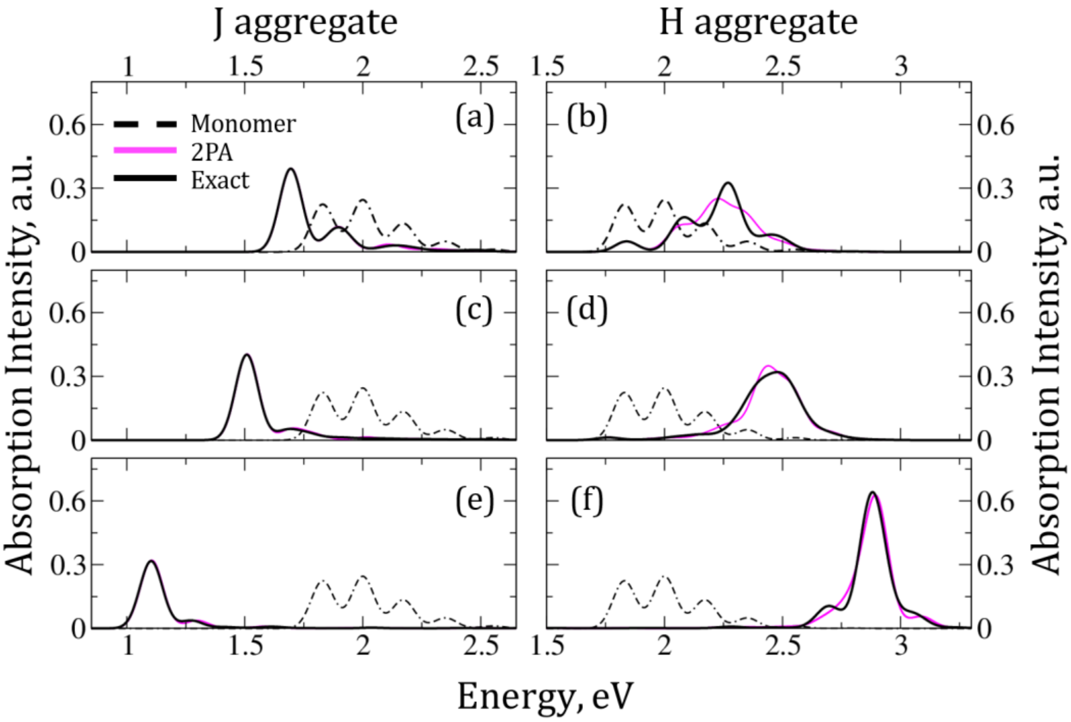

Figure 2.18: Absorption spectra for 2PA-lr and exact excitonic models for a 10 molecules aggregate allowing up to 6 phonons in the calculation. Long range interactions are taken into account: panels *a), c), e)* $J$ respectively $-0.085$eV, $-0.17$eV, $-0.34$eV; panels *b), d), f)* $J$ respectively 0.085eV, 0.17eV, 0.34eV. $\hbar\omega_\nu$=$\lambda$=0.17eV. In black dashed line the monomer spectrum is shown for comparison.

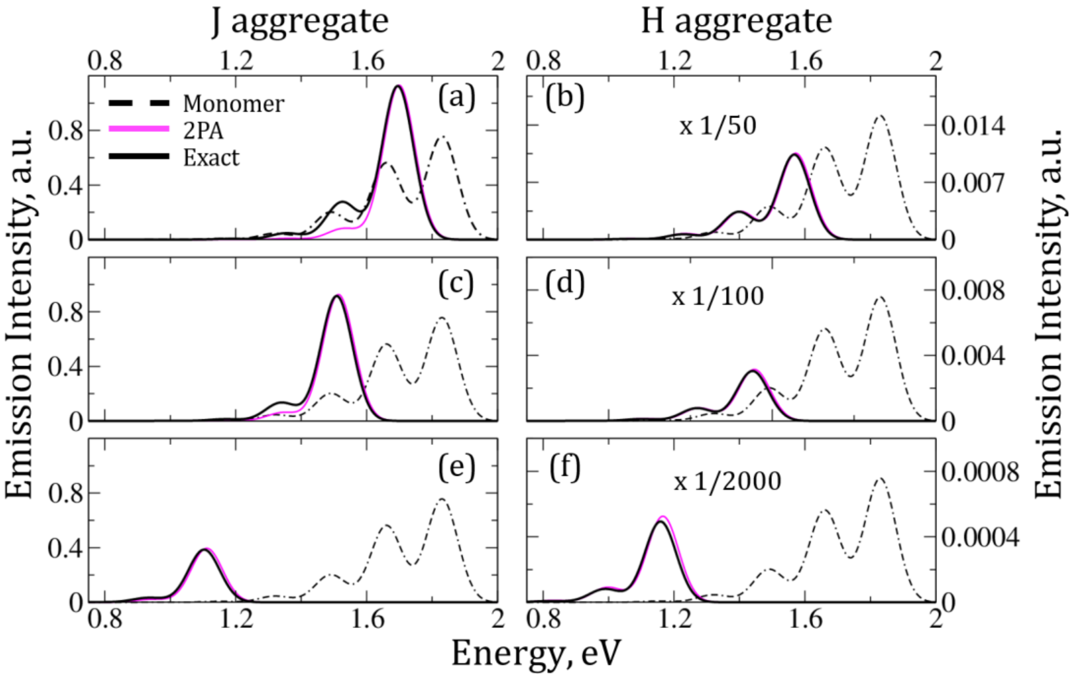

Figure 2.19: Emission spectra for 2PA-lr and exact excitonic models. Same parameters used in Fig. 2.18.

### 2.3.5 2D aggregates

#### Extending the exciton model

Having demonstrated that the exciton model works well at least to describe the frequencies of absorption and fluorescence bands, we now apply the model to describe optical spectra of molecular crystals of a series of fluorene-based dyes. The crystals were investigated by the group of Professor S.Jursenas (Vilnius University) and are of interest for their high optical quality. These fluorene derivatives[85] (illustrated in Fig. 2.20) form crystals with a well defined 2D structure, with weak intermolecular interactions between neighbor molecules in the same layer and negligible interlayer interactions (Fig. 2.21). In order to study the spectroscopic behavior of these systems, we introduce here a model for 2D aggregates.

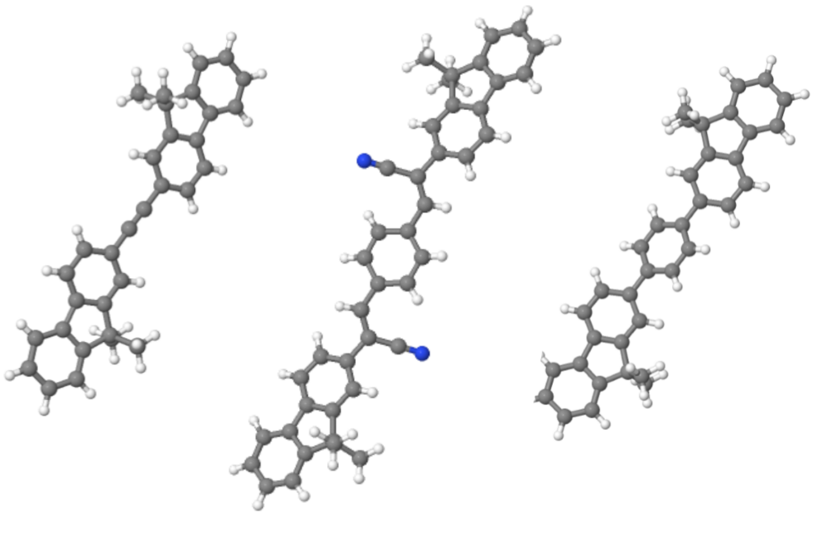

Figure 2.20: Molecular structure of the three crystal under investigation. From left to right: BF31, BF38 and GK08.

A 2 dimensional aggregate can be rationalized considering two main directions of interactions (named $J_x$ and $J_y$) and hence a two dimensional total wave-vector $\vec{K} =$

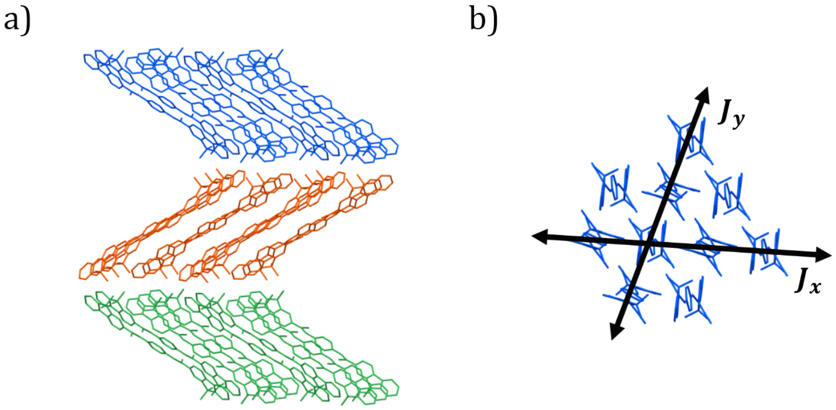

Figure 2.21: Crystal structure of BF38: (a) layered structure; (b) highlights of the two directions of interactions inside a single layer. Structures of BF31 and GK08 are completely analogous.

$(k_x, k_y)$, where $k_x$ and $k_y$ are defined as:

$$k_x = \frac{2\pi}{N_x} s_x \qquad k_y = \frac{2\pi}{N_y} s_y \tag{2.36}$$

$N_{x(y)}$ represents the number of molecules in the x(y) dimension, and $s_{x(y)}$ is anologous to its monodimensional counterpart. The Hamiltonian is written in the reciprocal space, as in Eq.2.26. The Paulion creation and annihilation operators are:

$$\hat{b}_K = \hat{b}_{k_x k_y} = \frac{1}{\sqrt{N_x N_y}} \sum_{m,n} e^{imk_x} e^{ink_y} \hat{b}_{mn} \tag{2.37}$$

$$\hat{b}^\dagger_K = \hat{b}^\dagger_{k_x k_y} = \frac{1}{\sqrt{N_x N_y}} \sum_{m,n} e^{imk_x} e^{ink_y} \hat{b}^\dagger_{mn} \tag{2.38}$$

where $i(j)$ runs on the $N_x(N_y)$ molecules. The exciton Hamiltonian in the reciprocal space reads:

$$\begin{aligned} H_{2D} &= \sum_K \hat{b}^\dagger_K b_K \left[ E + 2cos(k_x)J_x + 2cos(k_y)J_y \right] + \hbar\omega_v \sum_Q \left( \hat{a}^\dagger_Q \hat{a}_Q + \frac{1}{2} \right) \\ &- \frac{\lambda}{\sqrt{N}} \sum_{K,Q} (a^\dagger_Q b^\dagger_K b_{K+Q} + h.c.) \end{aligned} \tag{2.39}$$

where $b_K^\dagger$ creates an exciton with wavevector $\vec{K}$, whose energy is represented by the quantity in square parenthesis, $N$ represent the total number of molecules forming the aggregate ($N = N_x \cdot N_y$) and $\vec{Q} = (q_x, q_y)$ represents the two dimensional counterpart of the reciprocal space vibrations described in Eq. 2.26. Selection rules for absorption and emission are the same as in one dimension. Absorption is only possible from the ground state to a total-symmetric state ($\vec{K} = (0, 0)$), while the symmetry of the fluorescent state (the lowest excited state) depends on the sign of the interactions. Specifically, there are four possibilities for the wavevector of the fluorescent state, as shown in Table 2.1. where

| $J_x$ | $J_y$ | $\vec{K}$ |
|---|---|---|
| + | + | $(0, 0)$ |
| + | - | $(0, k_y^{max})$ |
| - | + | $(k_x^{max}, 0)$ |
| - | - | $(k_x^{max}, k_y^{max})$ |

Table 2.1: Possible values of $\vec{K}$ for the lowest excited state in bidimensional aggregates.

$k_i^{max}$, the highest value for the wavevector, depends on the number of molecules in the $i$ dimension ($N_i$):

$$k_i^{max} = \begin{cases} \pi, & \text{if } N_i \textit{ even} \\ \frac{N_i - 1}{N_i}\pi, & \text{if } N_i \textit{ odd.} \end{cases} \tag{2.40}$$

Reliable values for the $J_x$ and $J_y$ interactions are extracted in two steps. First we use TD-DFT (B3LYP functional, 6-31g(d,p) basis set) to calculate the magnitude and orientation of the transition dipole moment for the isolated molecules (see Table 2.2). Then, crystallographic data are exploited to calculate the interactions between transition dipole moments on different molecules, in the dipolar approximation:

$$J_{12} = \frac{1}{4\pi\varepsilon_0\eta^2 r_{12}^3}[(\vec{\mu}_1 \cdot \vec{\mu}_2) - \frac{3}{r_{12}^2}(\vec{\mu}_1 \cdot \vec{r}_{12})(\vec{\mu}_2 \cdot \vec{r}_{12})]|^2 \tag{2.41}$$

Specifically, we calculated interactions $J$ between all nearest neighbor couples in the crystal. For all the three systems, two major interaction are found as reported in Table 2.3 for $\eta^2 = 2$.

| Molecule | Bright Exc. State Energy (eV) | Trans. Dipole Moment (D) |
|---|---|---|
| **BF31** | 3.27 | 5.056 |
| **BF38** | 2.69 | 5.259 |
| **GK08** | 3.42 | 4.578 |

Table 2.2: Excited state energy and relative transition dipole moment magnitude for the 3 molecules under investigation.

| Molecule | $J_x$(eV) | $J_y$(eV) |
|---|---|---|
| **BF31** | 0.0059 | -0.030 |
| **BF38** | 0.053 | 0.028 |
| **GK08** | 0.061 | 0.021 |

Table 2.3: Interaction energies calculated for the three molecular crystals

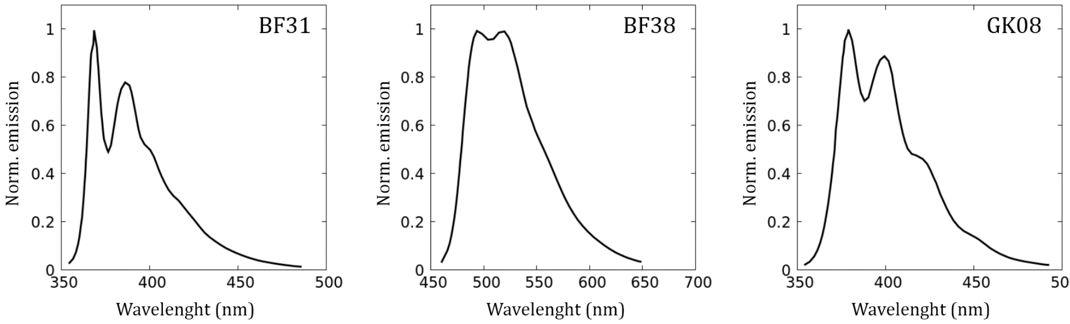

Figure 2.22: Normalized emission spectra calculated for the target molecules in THF solution.

The single layers are then modeled using a 5 × 3 bidimensional aggregate for a grandtotal of 15 molecules. Vibrational energies $\omega_v$ and electron-phonon couplings $\lambda$ are extracted from experimental monomer emission spectra (shown in Fig. 2.22). The difference in energy between the $0-0$ and $0-1$ vibronic peaks gives the vibrational energy, while the ratio between $0-0$ and $0-1$ peak intensities is proportional to the coupling $\lambda$. In fact, recalling the expression for the Franck-Condon coefficients:

$$\langle 0|n\rangle^2 = S^{\,n}\frac{e^{-S}}{n!} \qquad \text{with} \qquad S = \frac{\varepsilon_v}{\omega_v}, \tag{2.42}$$

and knowing $\varepsilon_v = \lambda^2/\omega_v$, the electron-photon coupling is obtained as:

$$\lambda = \sqrt{S}\omega_v \qquad \text{with} \qquad S = \frac{\langle 0|1\rangle^2}{\langle 0|0\rangle^2}. \tag{2.43}$$

In Fig. 2.23, 2.24 and 2.25, experimental absorption and emission spectra are compared to calculated spectra. The monomer absorption energies ($E$ in Eq. 2.39) are selected in order to match the position of experimental crystal absorption peaks. For both BF38 and GK08 the comparison between calculated and experimental spectra show a remarkably good match, both in absorbtion and emission. The bandshapes of the transitions, as well as the Stokes shift is satisfactorily reproduced. The results acquire additional value remembering that the parametrization of the Hamiltonian is obtained, except for the exciton energies, using electron-phonon couplings directly extracted from monomer spectra in solution and evaluating the $J_x$ and $J_y$ interactions from ab-initio calculations and experimental crystallographic data. On the contrary the modelization of BF31,

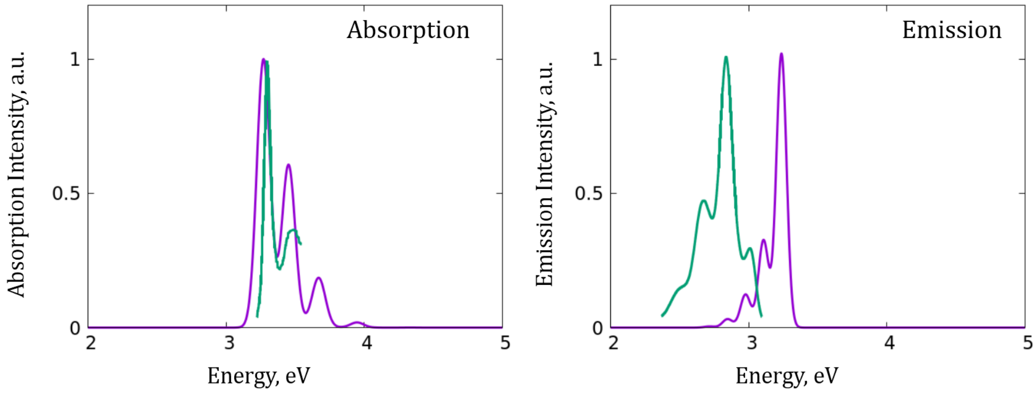

Figure 2.23: Comparison between experimental measured spectra, in green, and calculated spectra from Hamiltonian in Eq. 2.39, in violet, for the bf31 crystal. Left: absorption spectra; right: emission spectra.

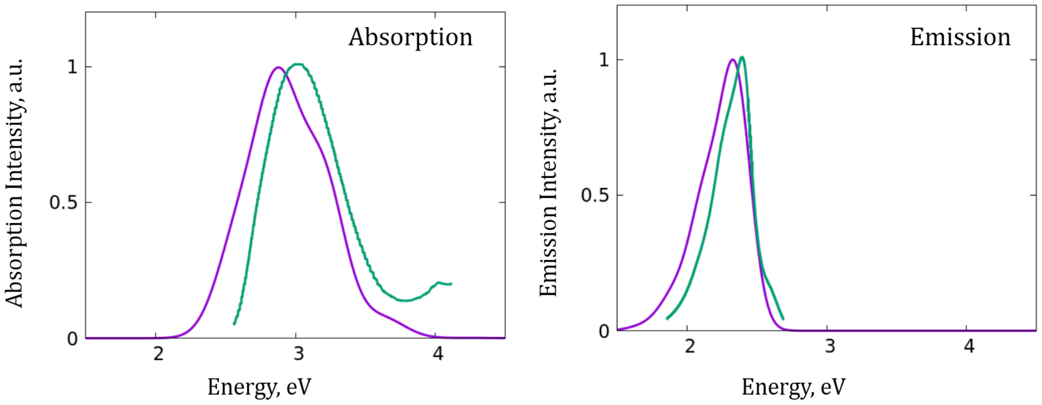

Figure 2.24: Comparison between experimental measured spectra, in green, and calculated spectra from Hamiltonian in Eq. 2.39, in violet, for the BF38 crystal. Left: absorption spectra; right: emission spectra.

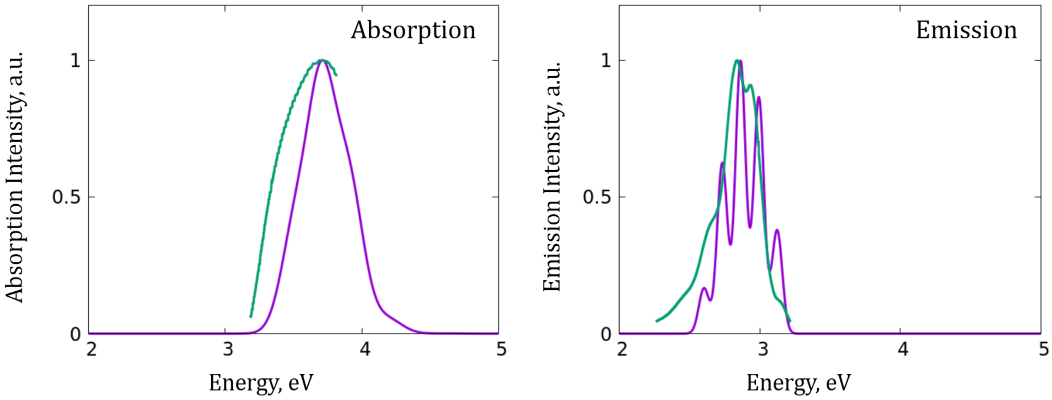

Figure 2.25: Comparison between experimental measured spectra, in green, and calculated spectra from Hamiltonian in Eq. 2.39, in violet, for the GK08 crystal. Left: absorption spectra; right: emission spectra.

while leading to an acceptable match in absorption spectrum, fail in the description of fluorescence, regarding both position and shape of the spectrum. The problem with this system can be due to the presence, in the two direction, of a positive and a negative interaction, which leads to a more cumbersome landscape that require bigger dimensions of the simulated aggregate.

## 2.4 Conclusions

In this chapter we have discussed effective models for molecular aggregates. First we have addressed linear aggregates of polar and polarizable molecules, extending a previous work[69, 62] to account for electron-vibration coupling. A clever choice of the basis, defined on the adiabatic electronic states in the mf approximation and accounting for the vibrational displacement via a Lang-Firsov transformation, allows to largely reduce the basis dimension, so that, also exploiting translational symmetry, we are able to treat fairly large systems, with up to 6 molecules. Apart from this important technical result, the proper choice of the basis amounts to a proper choice of the reference state. The apparently erratic behavior observed for aggregates of polar and polarizable molecules, where red-shifts are sometimes observed for H-aggregates and blue-shifts are sometimes observed for J-aggregates,[66] actually results from a poor choice of the reference state. Excitonic (and ultraexcitonic) effects, including shifts, must be evaluated against the transition frequencies obtained in the mf approximation, i.e. taking into account the large variation of the nature of the polarizable dye when inserted in a lattice of polar dyes. Once the proper reference is selected, J and H aggregates always give rise to red and blue-shifted absorption band. Similarly, anomalous effects on bandshapes and intensities are relieved when the proper reference state is considered. Our analysis demonstrates that, for aggregates of polar and polarizable dyes, when the proper reference is taken, the excitonic approximation works reasonably at least in the weak coupling regime. Ultraexcitonic effects are important in the strong couplig regime and particularly so in J-aggregates, where multiexcitonic states become prominent.[69, 62]

For aggregates of non-polar dyes we were able, exploiting symmetry and a clever computational implementation, to treat fairly large systems, as needed to validate several approximation schemes. More importantly we were able to address a fundamental problem of the exciton model that generates spectra that do not obey the sum rule for the oscillator strength. This is safely ascribed to the HL approximation. We demonstrated that the HL approximation, the main approximation adopted in the exciton model for aggregates of non-polar dyes, leads to good estimates of transition energies because of a cancellation of errors, while already in the weak interaction regime, the HL approximation leads to overestimated absorption (and fluorescence) intensities for

H-aggregates and underestimated intensities for J aggregates. Of course for large interactions, ultraexcitonic effects are also recognized in the frequencies of the bands.

Having demonstrated that the exciton model leads to reasonable results for weak interactions, we finally applied the model to describe optical spectra of three crystals of organic dyes, with good results, particularly in view of the minimal number of adjustable model parameters.

# Chapter 3

# Chiral aggregates of $\alpha$ and $\beta$-dicyanostylbenes: chiroptical properties

## 3.1 Introduction

Objects that cannot be superimposed to their mirror image, technically objects whose symmetry group does not contain any improper axis (including $S_1$ the mirror plane and $S_2$ the inversion center), are called chiral (from the greek word for hand). Chiral systems show special properties when interacting with light. At the linear order (weak electromagnetic fields) the Optical Rotatory Dispersion (ORD)[86, 87] measures the (frequency-dependent) difference between the refractive index for the left and right circularly polarized light and Circular Dichroism (CD)[88, 89] measures the difference in the corresponding extinction coefficients.[90, 91, 48] Of course ORD and CD spectra are related through integral expressions similar to the Kramers Krönig relations.[92] Chirality and chiroptical activity are observed in intrinsically chiral molecules, including molecules with chiral centers as well as chiral structures like helicenes. However, non-chiral molecules may give rise to chiral responses is some conditions as (a) under the effect of an external magnetic field[93, 94], when dissolved in chiral solvents [95, 96] or upon formation of chiral supramolecular systems.[97, 98]

We are particularly interested in supramolecular chirality, to investigate how chiroptical properties emerge in chiral molecular aggregates due to intermolecular interactions. Specifically, in this and in the subsequent chapter we will investigate chiral responses obtained in aggregates of non-chiral chromophores (dicyanostilbenes, DCSB, in this chapter, squaraines in the next chapter) that, decorated with chiral pendants, arrange themselves to form helical aggregates showing clear CD signals in a the chromophore spectral region, which is CD-silent for the non-aggregated dye.

In this chapter we will focus on aggregates formed by DCSB decorated with chiral pendants. Specifically, the molecules are composed by a conjugated central unit (spectroscopically active in the UV-visible region) linked to two chiral alkyl chains as in Fig. 3.1. They are denoted as $\alpha$- and $\beta$-DCSB depending on the position of the cyano groups in the chromophoric unit. Non-chiral $\alpha-$ and $\beta-$DCSB have been extensively investigated. [99, 100, 101] It is recognized that $\alpha$-DCSB typically form J-aggregates, while $\beta$DCSM form H-aggregates. Obtaining chiral aggregates of the two species then would offer the possibility to experimentally validate the novel chirality rule proposed in a joint effort from the host laboratory and the laboratory of Prof. K.George Thomas (IISER-Thiruvananthapuram, Kerala).[82] Specifically, the old, and widely adopted, chirality rule states that the sign of bisignated CD spectra typical of chiral supramolecular aggregates allows to define the hadedness of the aggregate. In particular, it states that the sign of the CD coupled (defined by the sign of the CD peak observed in the long-wavelength region) indicates a right-handed arrangement of the aggregate.[102, 103, 104] The new chirality rule, proposed from a theoretical analysis, states instead that the sign of the CD spectrum depends on both the chirality and on the sign of intermolecular interactions. Specifically, the old chirality rule applies to aggregates with dominating repulsive interaction (H-aggregates), while the rule is inverted in aggregates with dominant attractive interactions (J-aggregates). The study in this chapter will offer the first experimental validation of the new chirality rule.

## 3.2 DCSB: experimental results

All experimental work (synthesis and spectroscopic characterization) was performed by M. Sujith, student in the group of Prof. K. George Thomas, in the framework of an indo-italian collaboration project.

Fig. 3.2 shows absorption and fluorescence spectra of aggregates of $\alpha$ and $\beta$-DCSB in monomeric form (dissolved in THF solution) and in aggregated forms (80/20 water/THF mixtures). $\beta$-derivatives show clear signatures of H-aggregation, with a blue-shifted absorption, a largely redshifted emission and suppressed emission intensity. The situation is less clear in $\alpha$-derivatives where the red-shift in absorption is possibly partly superimposed to a tail due to scattering. In any case, results are compatible with J-aggregation, as also supported by the amplified fluorescence signal.

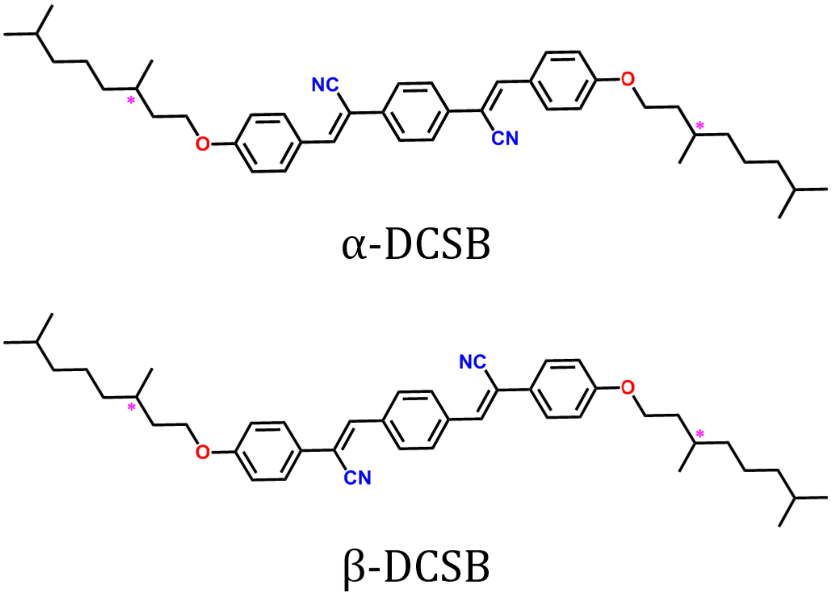

α-DCSB

β-DCSB

Figure 3.1: Structures of the two chromophore under investigation.

CD spectra in Fig. 3.3 are inspiring. Indeed spectra measured for aggregates of enatiomeric pairs (RR and SS) are equal and opposite, as expected. The most impressive

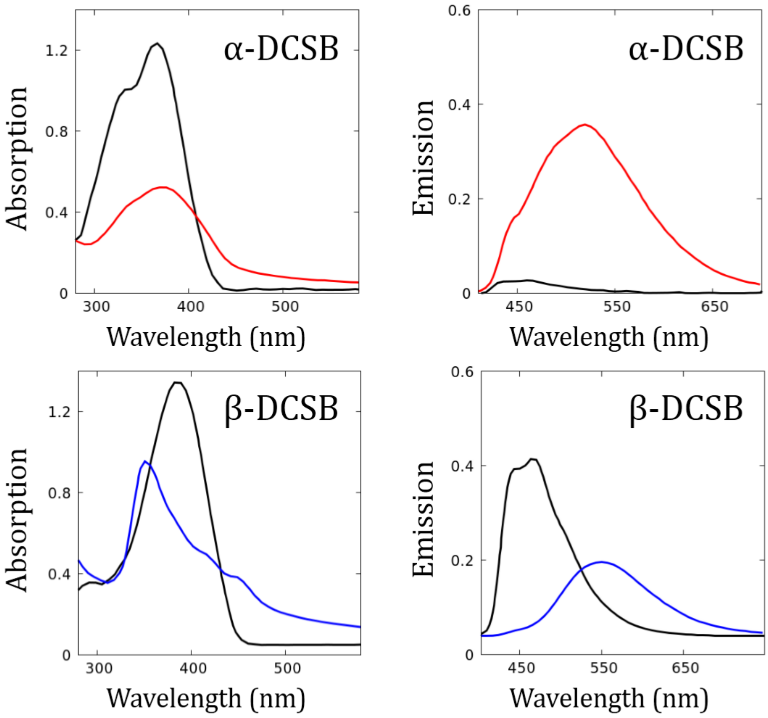

Figure 3.2: Absorption and emission spectra of the RR enantiomer of $\alpha$-DCSB (red curves, top) and $\beta$-DCSB (blue curves, bottom) in a 80/20 water/THF mixture. All spectra are compared to the relative monomer spectrum, in THF solution. Of course SS-enantiomers show very similar absorption and emission spectra as the RR enantiomer.

results is however the inversion of the sign of CD spectra measured for the $\alpha$ and $\beta$ species in the same enantioneric form. If we could prove that the $\alpha$ and $\beta$-DCSB in the same enantiomeric form give rise to structures with the same handedness, we would have a clear experimental demonstration of the new chirality rule. To get valuable information about the structure of the aggregates we undertook a MD study, that will be described in the next section. The structural information obtained from MD will be then exploited to build an exciton model for the aggregates, addressing both absorption and CD spectra.

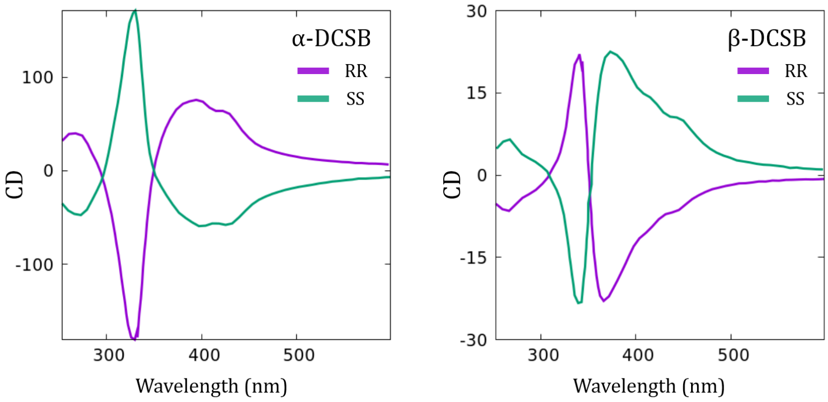

Figure 3.3: Circular Dichroism spectra for RR and SS enantiomers in 80/20 water/THF mixture. Left: $\alpha$-DCSB; right: $\beta$-DCSB. Monomer forms (in THF) are CD silent.

## 3.3 Molecular Dynamics

In order to simulate the aggregation of DCSB derivatives, we set up different simulations (one for each species) dealing with aggregates of 8 molecule in water. Following similar lines as in Chapter 1, we first address the definition of a proper force field.

### 3.3.1 Definition of the force field

DFT geometry optimizations were run (B3LYP/6-31G**, g16 package[105]) on the 4 target molecules:

- $\alpha$-DCSB-SS
- $\alpha$-DCSB-RR
- $\beta$-DCSB-SS
- $\beta$-DCSB-RR

From the optimized structures, atom types were selected according to the GAFF force field (Appendix B), employing antechamber tools.[106, 107] Atomic charges were computed according to RESP procedure: obviously R and S enantiomers give raise to the same atomic type and corresponding charges. Some bonding parameters that were incorrectly assigned were adjusted. In particular, the dihedral angles $\phi_i$, $\phi_o$, $\phi_m$ in Fig. 3.4 require a careful parametrization[100, 101], as DCSB molecules are known to exhibit specific torsional behaviour (Table 3.1). Values were selected to ensures a physically-relevant structures consistent with the experiment and the computational scans at DFT levels reported in the literature.[108]

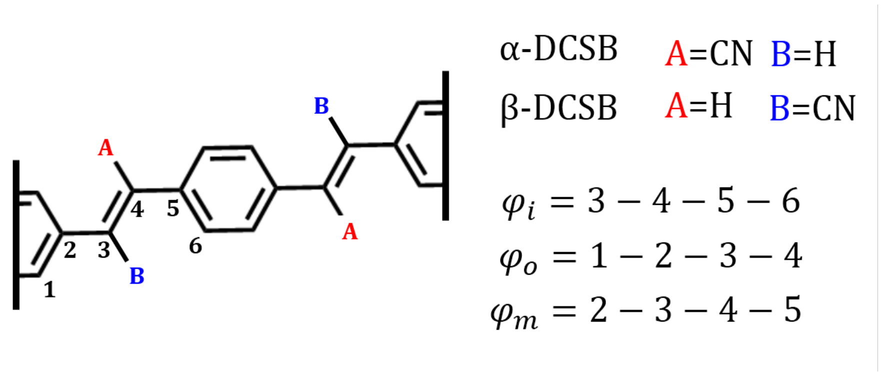

Figure 3.4: Representation of the three dihedral angles $\phi_i$, $\phi_o$ and $\phi_m$.

| Dihedral | $\alpha$-DCSB $(Kcal \cdot mol^{-1} \cdot \AA^{-2})$ | $\beta$-DCSB $(Kcal \cdot mol^{-1} \cdot \AA^{-2})$ |
|---|---|---|
| $K_{\phi i}$ | 21.3 | 55.6 |
| $K_{\phi o}$ | 55.6 | 21.3 |
| $K_{\phi m}$ | 55.6 | 55.6 |

Table 3.1: Force constants for the $\phi_i$, $\phi_o$ and $\phi_m$ dihedrals in $\alpha$ and $\beta$-DCSB.

We run TD-DFT calculations on the optimized geometries, addressing the lowest excited singlet, an optically allowed state. Results obtained with B3LYP/6-31G** and cam-B3LYP/6-31G** are listed in Table 3.2 and compared with experiment. As expected, B3LYP underestimates while cam-B3LYP overestimates transition energies. In any case transition dipole moments are very similar comparing the two functionals and we keep the ones extracted from B3LYP for the following modelizations. Orientation of transition dipole moments on the molecular units is shown in Fig. 3.5.

| **$\alpha$-DCSB (R/S)** | Bright Exc. State Energy (eV) | Trans. Dipole Moment (D) |
|---|---|---|
| B3LYP | 3.025 | 4.713 |
| cam-B3LYP | 3.500 | 4.860 |
| Exp. Value | 3.31 | |
| **$\beta$-DCSB (R/S)** | | |
| B3LYP | 2.755 | 4.971 |
| cam-B3LYP | 3.230 | 4.907 |
| Exp. Value | 3.06 | |

Table 3.2: Transition energies and dipole moment for the lowest excited states of the $\alpha$ and and $\beta$-DCSB molecules using two different levels of theory.

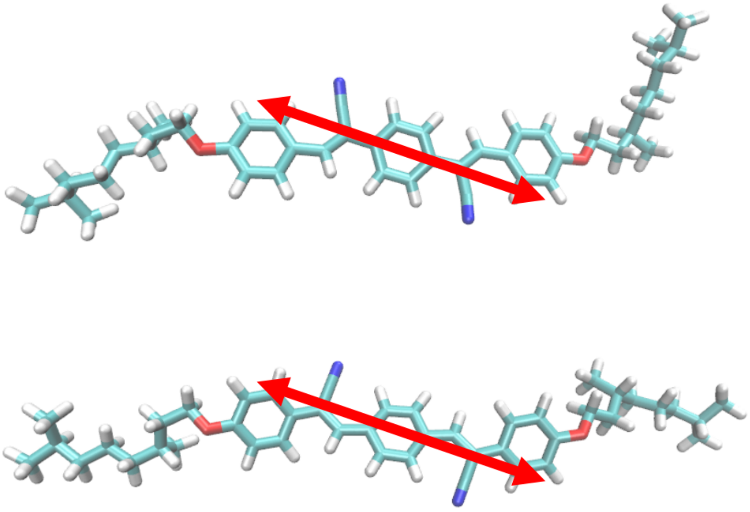

Figure 3.5: Representation of the orientation of transition dipole moments relative to the molecular structures. Top panel: $\alpha$-DCSB; bottom panel:$\beta$-DCSB.

### 3.3.2 MD simulations on aggregates

Having carefully parametrized the molecular force field, we proceed with aggregation studies in solution. Simulation boxes with a volume of $14.4\times14.4\times14.4$ nm$^{3}areprepared, inwhich8moleculesare$

and $\beta$-DCSB molecules with non-chiral substituents[99, 100] and start our MD simulation from a configuration obtained arranging the eight molecules of the $\alpha$ and $\beta$-DCSB derivatives mimiking stacks extracted from the relevant crystal structures, as shown in Fig. 3.6. We notice that, since the crystal structures are obtained for non-chiral systems, the starting configuration is non-chiral.

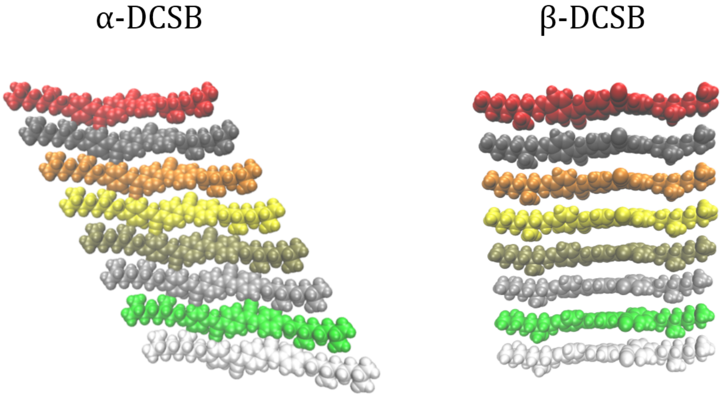

Figure 3.6: Initial configurations of $\alpha$- and $\beta$-DCSB.

Molecular dynamics simulations are then run with a first minimization step, followed by a 30 ns NPT (see Appendix B) equilibration (needed to allow molecules to arrange in the thermodynamically stable structure) and a final 200 ns NPT main run with a 1 ps timestep. In the poor solvent (water) the molecules reorganize to minimize the interaction with the solvent. The central chromophoric units interact via $\pi$-$\pi$ stacking while the side chiral chains, with asymmetric interactions, impart an overall torsion to the whole supramolecular aggregates. The high flexibility of the molecules together with the large number of units, result in a somewhat messy conformational landscape. Nevertheless, a preferential packing is clearly detected for the 4 investigated systems. In Fig. 3.7 the most representative structures arising for each of the long trajectories are presented.

All systems are characterized by a well-defined helical structure, shaped by interactions of side pendants. The RR enantiomers (either $\alpha$ or $\beta$-DCSB) show a left-handed helix organization, while SS enantiomers form a right handed helix. The MD results,

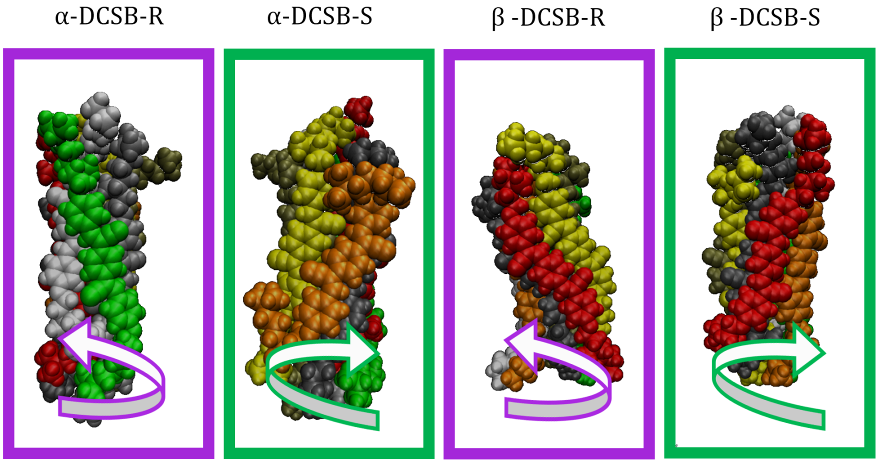

Figure 3.7: Most relevant structures of the 4 systems under investigation.

showing that $\alpha$ and $\beta$-DCSB substituted with the same chiral pendant aggregate in supramolecular structures with the same handedness but showing opposite CD signal is a first confirmation of the validity of the new chirality rule, stating that the sign of CD spectra depends not only on the chirality of the system, but also on the sign of intermolecular interactions. However, more reliable results and a better understanding of the phenomenon can be obtained via a detailed calculation of absorption and CD spectra of the aggregates.

## 3.4 Absorption and CD spectra of DCSB aggregates

### 3.4.1 The model

To model our aggregate we adopt the standard exciton model for non-polar dyes (i.e. we impose the HL approximation, see Chapter 2) and neglect the coupling to molecular vibration. As discussed previously, the exciton model gives acceptable results for optical spectra of non-polar dyes and, for largely disordered system, the information about the vibronic structure is smeared out by inhomogeneous broadening effects.

With these approximations, the excitonic Hamiltonian for a generic aggregate of $N$ identical molecules reads:

$$\hat{H} = \sum_{n} E_0 |n\rangle\langle n| + \sum_{nm} V_{nm} |n\rangle\langle m| \tag{3.1}$$

where $|n\rangle$ identifies the basis state in which the $n$th molecule is in its excited state ($|g_1, g_2 \dots e_n \dots g_N\rangle$), with energy $E_0$, and $V_{nm}$ is the dipole-dipole interaction term:

$$V_{nm} = \frac{1}{4\pi\varepsilon_0 n^2} \frac{|r_{n,m}|^2 \vec{\mu}_0{}^n \cdot \vec{\mu}_0{}^m - 3(\vec{\mu}_0{}^n \cdot \vec{r}_{nm})(\vec{\mu}_0{}^m \cdot \vec{r}_{nm})}{r_{n,m}^5} \tag{3.2}$$

where $\vec{\mu_0}^n$ is the transition dipole moment for the excitation on the $n$-th molecule and $\vec{r}_{nm}$ is the vector distance between sites $n$ and $m$. In the following we will use the molecular transition dipole moments obtained by TD-DFT (B3LYP/6-31G**) as discussed in Section 3.3, anchored to the molecular site.

The diagonalization of the excitonic Hamiltonian on the $N$ basis gives the excitonic eigenstates accounting for the linear combination of singly excited states. Transition dipole moment, from the ground state to the $k$ eigenstate, $\vec{\mu}_t{}^k$, is obtained as linear combinations of molecular transition dipole moments:

$$\vec{\mu}_t{}^k = \sum_{n} \vec{\mu}_t{}^{kn} = \sum_{n} \langle k|n\rangle \vec{\mu}_0{}^n \tag{3.3}$$

where $k$ runs on the eigenstates and $\vec{\mu}_0{}^n$ is the dipole moment associated to the $|g\rangle \rightarrow |e\rangle$ transition in the $n$th molecule. The absorption spectrum is calculated assigning a Gaussian lineshape to each transition:

$$A(\omega) = \hbar\omega \sum_{k} \left|\vec{\mu}_t{}^k\right|^2 e^{\frac{(\hbar\omega - E_k)^2}{2\sigma^2}} \tag{3.4}$$

where $E_k$ is the energy of the transition from the ground to the $k$ eigenstate.

In the proposed model, electrons are localized on each molecular unit. In this case, as first demonstrated in a classical work by Condon[91], CD spectra can be calculated from the knowledge of transition dipole moments. In fact, in this limit, transition magnetic dipole moments, needed to calculate CD spectra (see Chapter 4 for further details), can be expressed in terms of transition dipole moments. Following Condon we define the rotational strength for each transition from the ground to the $k$-eigenstate as

$$R_k = -E_k \sum_{nm} \vec{r}_{nm} \cdot ({\vec{\mu}_t}^{kn} \times {\vec{\mu}_t}^{km}) \tag{3.5}$$

where ${\vec{\mu}_t}^{kn}$ is the dipole moment of the $|0\rangle \rightarrow |k\rangle$ transition relative to molecule $n$. Replacing Eq. 3.3 in Eq. 3.5, we obtain the explicit expression for $R_k$:

$$R_k = -E_k \sum_{nm} \vec{r}_{nm} \langle n|k\rangle\langle m|k\rangle \cdot ({\vec{\mu}_0}^{n} \times {\vec{\mu}_0}^{m}) \tag{3.6}$$

CD spectra, measuring the difference between exctinction coefficient of left and right circularly polarized light, is simply obtained assining a Gaussian lineshape with width $\sigma$ to each transition:

$$\Delta\epsilon(\omega) \propto \sum_k R_k e^{\frac{(\hbar\omega - E_k)^2}{2\sigma^2}} \tag{3.7}$$

### 3.4.2 Calculated Spectra

The output of MD simulations is a collection of configurations. Assuming that the transition dipole vectors calculated for the isolated molecules stay constant during the dynamics with respect to the molecular frame of each monomer, we can calculate, for each configuration of the aggregate, the electrostatic interactions entering the Hamiltonain (see Eq. 3.2). The values of $E_0$, corresponding to the transition energy for the isolated monomer, are extracted from experimental values in Fig. 3.2 and are set to 3.37 eV for $\alpha$ deriatives and 3.10 eV for $\beta$ derivatives. The Hamiltonian is then diagonalized and transition energies, transition dipole moments and rotational strengths are finally obtained.

With these information, absorption and CD spectra are calculated (Eq. 3.7, setting $\sigma$=0.07 eV). The resulting spectra are then averaged over a large portion of dynamics (60 ns). Results for the absorption and and CD spectra of the 4 systems under investigation are shown in Fig. 3.8 and 3.9.

Calculated spectra and experimental data presented in Fig. 3.2 are generally in good agreement. Rotational strenghts extracted from trajectories mimic accurately experimental CD spectra. Specifically, we obtain the correct signs for CD spectra for the 4 simulations. This result, together with the most relevant structures presented in Fig.

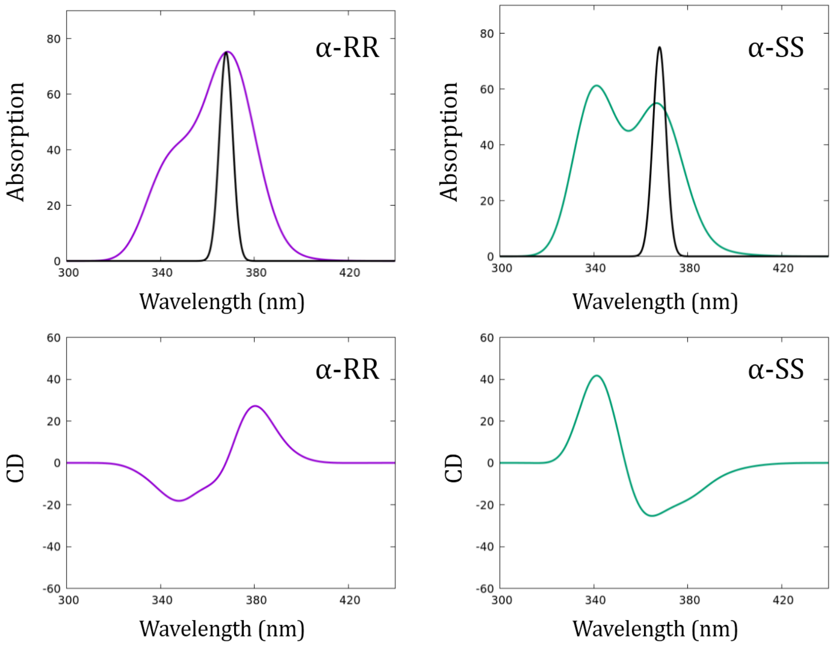

Figure 3.8: Top panels: absorption spectra of both enantiomers of $\alpha$-DCSB compared to the monomer (black curve). Bottom panels: corresponding CD spectra.

3.7, demonstrate the reliabilty of our hybrid method in the modelization of these complex systems. Results for $\beta$-DCSB are very good: absorption spectra of both enantiomers are very similar, comfirming that the equilibrium geometry is obtained for both species, and show a very clear blue-shift with respect to the monomer. Results for $\alpha$-DCSB are less satisfactory. While the spectrum for the R enatiomer has its main peak slightly red shifted with respect to the monomer, both R and S systems present a not negligible band at higher energy, denoting the formations of H type clusters. More critically, the absorption spectra of the two $\alpha$-enantiomers differ considerably, suggesting that the MD simulation has not yet fully converged to the equilibrium. For this reason, while results for all systems are promising, calculations on $\alpha$ derivatives are still on going.

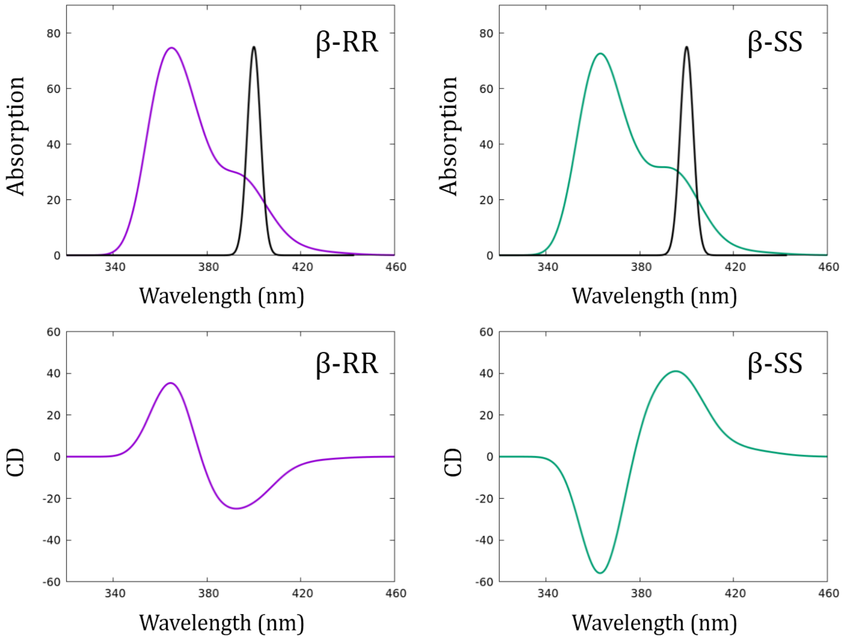

Figure 3.9: Top panels: absorption spectra of both enantiomers of $\alpha$-DCSB compared to the monomer (black curve). Bottom panels: corresponding CD spectra.

## 3.5 Conclusions

In this Chapter we suggested a novel approach to the spectroscopic characterization of complex aggregates in solution. We proposed a hybrid method, based on the combination of MD simulations and exciton models to calculate absorption and circular dichroism spectra of a family of dicyanostilbenes (DCSB) derivatives. In particular, we focused our investigation on 4 systems: $\alpha$-DCSB (R and S enantiomers) and $\beta$-DCSB (R and S enantiomers) that show different spectroscopic behavior depending on the nature of the chromophoric unit and the chirality of the side chains. With the use of MD we studied the aggregation of these systems in solution. Starting from completely achiral arrangements of monomers, extracted from crystallographic data on related systems, well defined clusters are obtained, with an overall helicity that only depends on the chirality of side chains. Geometric informations were extracted from classic trajectories and then processed in order to parametrize an exciton model. Absorption and CD spectra are then calculated for the 4 systems of interest, averaging over thousands of conformations. We obtain CD spectra in good agreement with experimental data. The hybrid technique proposed in this Chapter represents a reliable method for the replication of chiroptical properties in unusual chiral assemblies, where the fine interplay between chromophores nature and peripheral ligand chirality contributes to complex outcomes.

# Chapter 4

# Chiral aggregates of squraine dyes

## 4.1 Introduction

Squaraines are a widely investigated family of organic dyes, characterized by a resonance stabilized structure where the central squaryl ring, a strong electron-acceptor unit, is conjugated to two electron-donating groups, as in the examples shown in Fig. 4.1. Squaraines have interesting spectroscopic properties, with intense and sharp absorption and emission bands in the red and near-IR spectral regions and large two-photon cross-sections. They are investigated for applications in dye-sensitized solar cells[3, 4], in colorimetric sensors [109] and non-linear optics.[110] Moreover, their rigid conjugated structure allows the formation of stable aggregates, [111, 112] whose unsusual spectroscopic properties further widen the possible range of applications. The study of self-organization and aggregation behaviour of squaraine dyes is a fairly hot topic in recent years. [113, 16, 114, 14]

Chiral aggregates of squaraine dyes were obtained $\sim$ 15 years ago via the supramolecular arrangment of squaraine dyes decorated at the two sides by chiral groups[115, 112]. The chiral supramolecular arrangment is demonstrated by the observation of characteristic CD spectra for the aggregate structure, in the region of the squaraine absorption, CD-silent for the non-aggregated dye. New attention on chiral squaraine aggregates was called by a recent paper from the group of Manuela Schieck [114], showing how

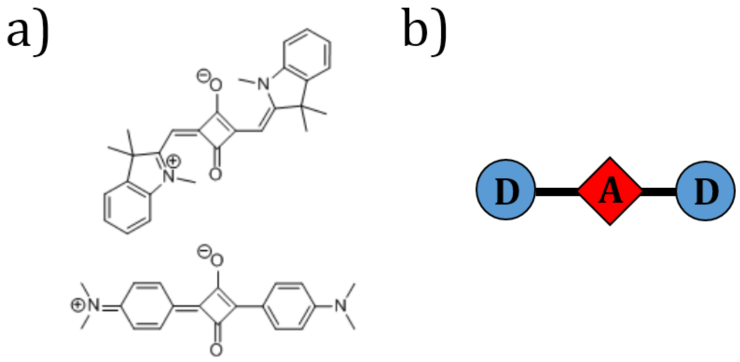

Figure 4.1: a): example of two squaraine dyes; b): schematic representation of the squaraine D-A-D structure.

aggregates deposited on films give rise to very large CD signals.

In this chapted we describe an extensive theoretical work that, devoted to the analysis of absorption and CD spectra of chiral squaraine aggregates in solution, represents a first fundamental step to understand the behavior of aggregates deposited on films. This work is done in collaboration with experimentalists and specifically with researchers in the group of Professors Manuela Schiek (Johannes Kepler University of Linz, Austria) and Arne Lützen (University of Bonn, Bonn). Fig. 4.2 (courtesy of PhD student Jennifer Zablocki) shows representative absorption and CD spectra for aggregates in solution. Indeed a very large number of results are available on aggregates of squaraine dyes with different substituents (Fig. 4.3). For all aggregates absorption spectra show aggregations features both to the blue and to the red of the monomer band, located at 650 nm. We will dub the two features as H and J bands, respectively, even if their nature (as it will be demonstrated below) is different.

Initially, the two bands were ascribed to two features associated with the exciton splitting of the monomer band. This however would require a fairly large intermolecular interactions. Moreover, this interpretation contrasts sharply with the observed CD spectra. Indeed if the H and J bands were the two features due to the exciton splitting, one would have observed in CD spectra a single bisignated signal with opposite sign at the

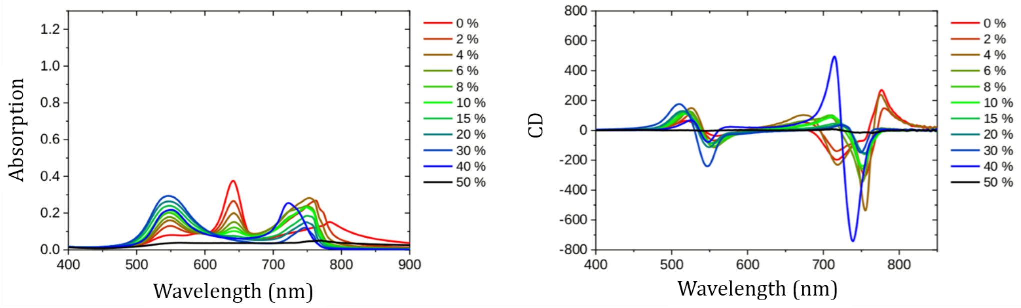

Figure 4.2: Absorption (left) and CD (right) spectra measured for the ProSQ-SS-C10 molecule in methanol upon addition of water.

H an J band locations. Instead, the CD spectrum shows two distinct bisignated signals, one in the region of the H and and one in the region of the J band. The possibility that the H and J bands are due to the simultaneous presence of different kinds of aggregates in the same sample is not very likely, due to the consistent observation of the two features in samples obtained in different experimental conditions and using dyes with different substituents. Absorption and CD spectra of chiral squaraine aggregates then call for a careful modelization that will be the topic of this chapter.

## 4.2 The three state model for squaraine dyes

The spectroscopic behaviour of quadrupolar DAD dyes, and specifically of squaraines, can be rationalized adopting an essential state model, based on 3 electronic basis states [116]. The three orthogonal states are a neutral state $|N\rangle$, and two degenerate states, $|Z_1\rangle$ and $|Z_2\rangle$, corresponding to the two zwitterionic structures $D^+A^-D$ and $DA^-D^+$. On this basis, the electronic Hamiltonian is:

$$\hat{H}^{el} = 2z_0\hat{\rho} - \tau\hat{\sigma} \tag{4.1}$$

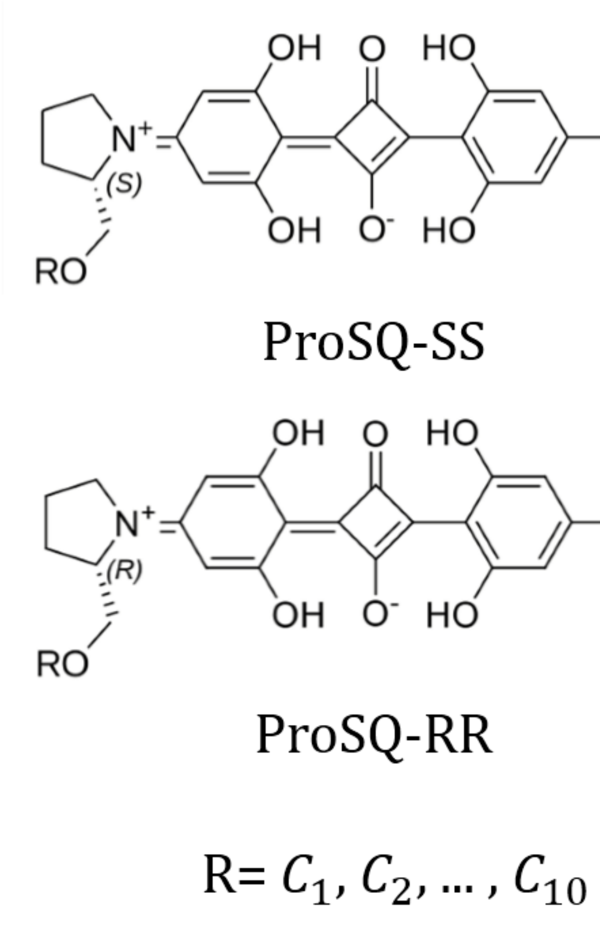

Figure 4.3: Structure of the ProSQ family studied in the group of Professor Manuela Schiek.

where $2z_0$ is the energy required to transfer a charge from the D to the A site and $-\tau$ is the matrix element that mixes $N$ and $Z_{1,2}$ states. The operator $\hat{\rho}$ and $\hat{\sigma}$ are defined as:

$$\hat{\rho} = \begin{pmatrix} 0 & 0 & 0 \\ 0 & 1 & 0 \\ 0 & 0 & 1 \end{pmatrix} \qquad \hat{\sigma} = \begin{pmatrix} 0 & 1 & 1 \\ 1 & 0 & 0 \\ 1 & 0 & 0 \end{pmatrix} \tag{4.2}$$

The dipole moment is negligible in the neutral state and is set to $\pm\mu_0$ for the two zwitterionic states, where it points in opposite directions of equal magnitude:

$$\hat{\mu} = \mu_0 \begin{pmatrix} 0 & 0 & 0 \\ 0 & 1 & 0 \\ 0 & 0 & -1 \end{pmatrix} \tag{4.3}$$

The electronic Hamiltonian is diagonalized to obtain the molecular electronic eigenstates (Fig. 4.4):

$$\begin{aligned} |g\rangle &= \sqrt{1-\rho}|N\rangle + \sqrt{\frac{\rho}{2}}(|Z_1\rangle + |Z_2\rangle) \\ |e_1\rangle &= \frac{1}{\sqrt{2}}(|Z_1\rangle - |Z_2\rangle) \\ |e_2\rangle &= \sqrt{\rho}|N\rangle - \sqrt{\frac{1-\rho}{2}}(|Z_1\rangle + |Z_2\rangle) \end{aligned} \tag{4.4}$$

where:

$$\rho = \frac{1}{2} - \frac{\eta}{2\sqrt{\eta^2+\tau^2}}, \tag{4.5}$$

measures the charge separation in the ground state as $\mathrm{D}^{+\rho/2}\mathrm{A}^{-\rho}\mathrm{D}^{+\rho/2}$.

The lowest energy excited state $|e_1\rangle$ is optically active, with a transition dipole moment $\mu_0\rho$. The second excited state $|e_2\rangle$ is a dark state, active in two-photon absorption.[117] The original model[116] also accounts for electron-vibration coupling as needed to address in detail the bandshape of optical spectra. Very good agreement with experimental data was in general observed. However, vibronic effects are marginal in squaraine dyes and, in our discussion of aggregates, we will not account for them.

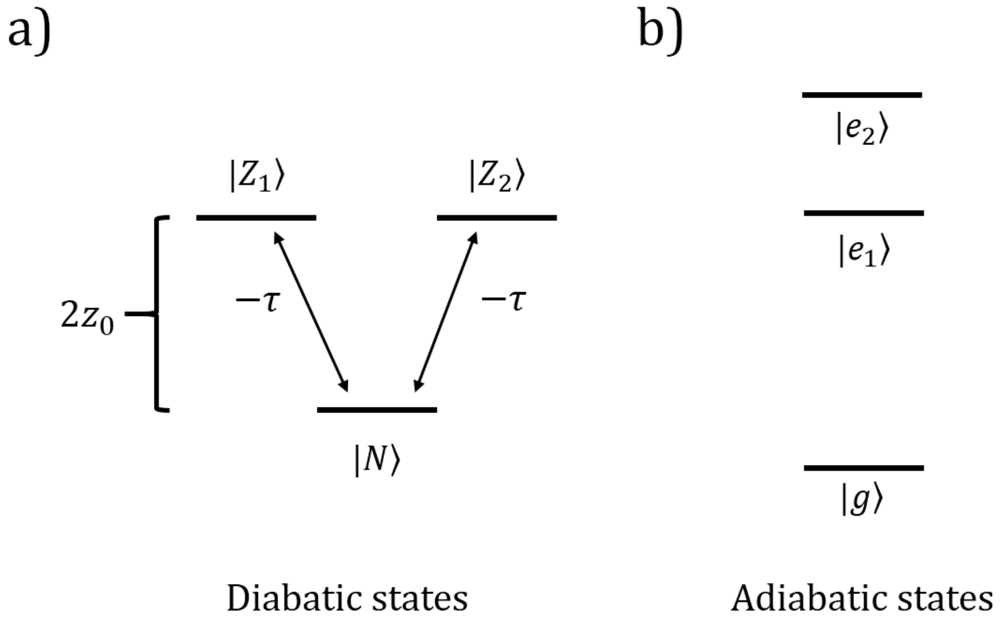

Figure 4.4: Illustration of the electronic states in the essential states model for a quadrupolar chromophore. (a) energy-level diagram of the diabatic states; (b) energy-level diagram of the adiabatic states.

## 4.3 Aggregate model: electrostatic interactions

Aggregates of quadrupolar dyes have been extensively investigated in recent years, both theoretically and experimentally.[80, 118, 119, 120, 121, 122] In these papers, aggregation was modeled accounting for electrostatic intermolecular interactions. Specifically, much as with dipolar dyes, on the adopted diabatic basis electrostatic interactions account for the interactions between molecules in their charge-separated states, affecting their diagonal energies. Charge densities are reduced to positive and negative point charges residing on the donor sites and at the center of the squaryl ring, respectively. The aggregate Hamiltonian is the sum of monomer Hamiltonians (in Eq. 4.1 plus a term accounting for intermolecular interactions:

$$\hat{H} = \sum_m \left(2z_0\hat{\rho}_m - \tau\hat{\sigma}_m\right) + \sum_{m>n} V_{ij}^{mn}\rho_{i,m}\rho_{j,n} \tag{4.6}$$

where $m, n$ indices run on the molecular sites, and $i, j$ run on the three sites (DAD) defined on each molecule. The operators measuring the site ionicities are defined, for each $m$ as

$$\hat{\rho}_1 = \begin{pmatrix} 0 & 0 & 0 \\ 0 & 1 & 0 \\ 0 & 0 & 0 \end{pmatrix} \qquad \hat{\rho}_2 = \begin{pmatrix} 0 & 0 & 0 \\ 0 & -1 & 0 \\ 0 & 0 & -1 \end{pmatrix} \qquad \hat{\rho}_3 = \begin{pmatrix} 0 & 0 & 0 \\ 0 & 0 & 0 \\ 0 & 0 & 1 \end{pmatrix} \tag{4.7}$$

$V_{ij}^{mn}$ measures the electrostatic interaction between charges on sites $i, j$ on molecules $m, n$ as follows:

$$V_{ij}^{mn} = \frac{1}{4\pi\varepsilon_0\eta^2}\frac{1}{|\vec{r}_{i,m} - \vec{r}_{j,n}|} \tag{4.8}$$

with $\vec{r}_{i,m}$ being the position of site $i$ in molecule $m$ and $\eta$ the refractive index. This Hamiltonian is easily written and diagonalized on the basis of 9 states obtained as the direct product of the three basis state on each dye:

$$|NN\rangle, \quad |NZ_1\rangle, \quad |NZ_2\rangle, \quad |Z_1N\rangle, \quad |Z_1Z_1\rangle, \quad |Z_1Z_2\rangle, \quad |Z_2N\rangle, \quad |Z_2Z_1\rangle, \quad |Z_2Z_2\rangle \tag{4.9}$$

To calculate spectra, we need a definition of the dipole moment operator. Since the Hamiltonian describes a system where electrons are localized on each molecular site, the total dipole moment operator is simply the vectorial sum of the molecular dipole moments operators, defined above (of course each molecular dipole moment is aligned along the DAD axis). Spectra calculated for two dimeric structures are reported in Fig. 4.5. The Hamiltonian is parametrized fixing molecular parameters $z_0 = 0.2$ eV and $\tau = -1.2$ eV,[116] leading to a monomer absorption at $\sim 650nm$. The intramolecular D-A distance (needed to evaluate the interactions in Eq. 4.8) is set to $a = 5.3$ $\mathring{A}$ and the refractive index is set to $\eta = 2$. In both configurations molecules are aligned along the squaraine long axis, the distance between the axis being 4 Å. In the stacked geometry (Fig4.5A) repulsive interactions dominate, resulting in a blue-shift of the spectrum. When the molecules are displaced so that the donor of the first molecule is aligned with

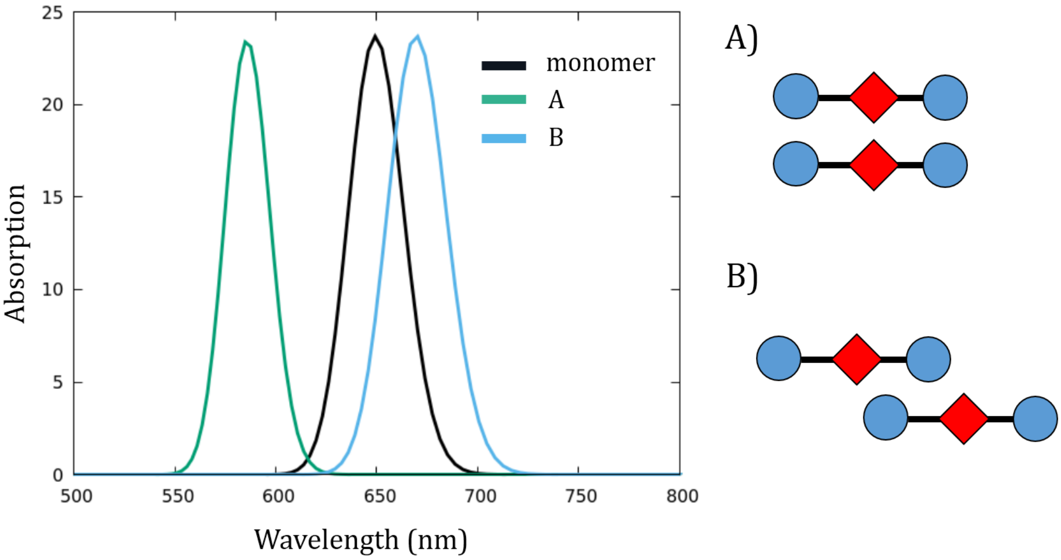

Figure 4.5: Absorption spectra (left) for a model squaraine dimer in two configurations (sketched on the right), compared to the monomer spectrum. For clarity, all spectra are calculated assigning a gaussian bandshape to the transitions with $\sigma = 0.04$ eV.

the acceptor of the second molecule (Fig4.5B), attractive interactions dominate and the absorption band red-shifts compared to the monomer.

Of course in twisted molecular geometries, like in Fig. 4.6 one observes for each dimer both the band to the red and the one to the blue of the monomer band (even if possibly with different intensities). The twisted dimers are clearly chiral and it is interesting to calculate Circular Dichroism (CD) spectra. The calculation is not difficult, indeed the adopted model Hamiltonian has the electrons perfectly localized on the molecular units, so that molecular dipoles moments are well defined. In these conditions, following the classical work of Condon,[91] the rotational strength needed to calculate CD spectra can be expressed in terms of the molecular transition dipole moments.[82] Specifically, for the transition from the ground state to the excited $k$ state, the rotational strength depends on the transition energy $E_k$ and relative orientation of single molecule transition dipole moments, as defined in Chapter 3 (Eq. 3.5).

Results for two tilted dimers for molecules forming an angle $\alpha = 25^\circ$ are reported in Fig. 4.6. As expected, bisignated CD spectra appear with a positive and a negative peak located in the proximity of the two exciton bands observed in absorption. Quite interestingly, both dimers correspond to right-handed helices, but only dimer (A) with predominant repulsive interactions obeys the *chirality rule*[102] while dimer (B) shows the opposite behavior. This is in line with with recent results in the laboratory,[82] proving that, as discussed in the previous chapter, the chirality rule only holds for positive (repulsive) interactions, while it is reversed for negative (attractive interactions).

It is clear from results in Fig. 4.6 that a simple model only accounting for electrostatic intermolecular interactions cannot account for the complex CD spectra observed experimentally (see Fig. 4.2). Considering larger systems does not change the results and attempts to account for symmetry-lowering phenomena, related to local asymmetry, possibly making the dark state optically active, were ineffective: even pushing model parameters towards extreme values we were not able to explain the observed spectral features. Other interactions must be introduced, as first recognized by Spano and Collison, studying non-chiral aggregates of squaraine dyes.[14]

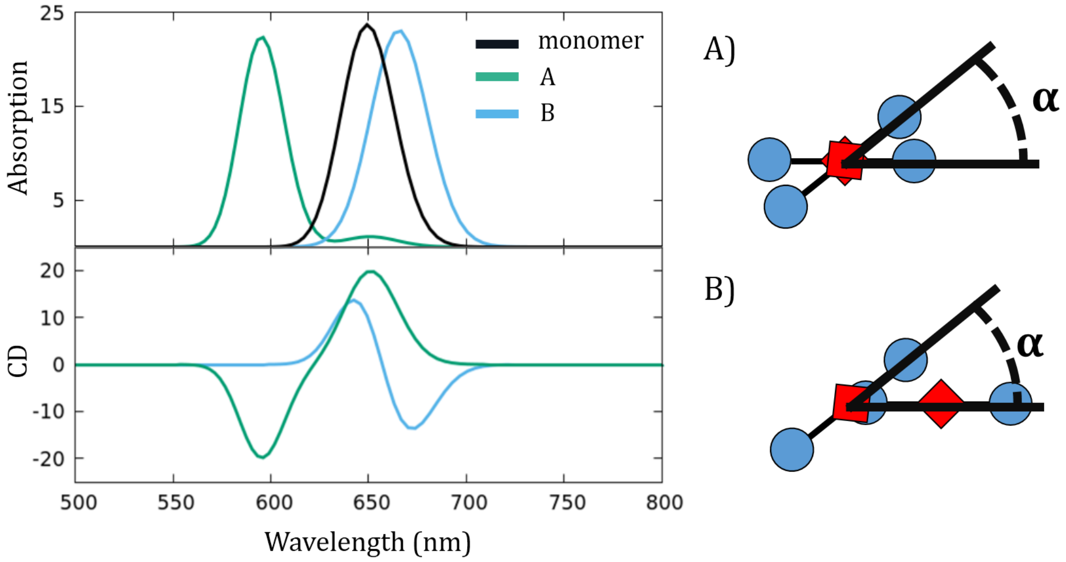

Figure 4.6: Absorption (top-left) and CD (bottom-left) spectra for the same system in Fig. 4.5, with a finite tilt angle $\alpha = 25°$.

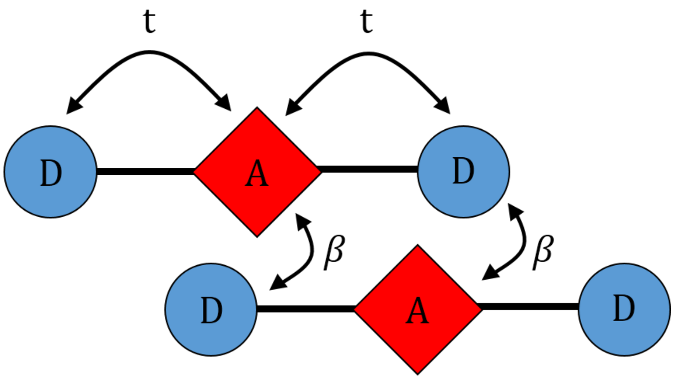

Figure 4.7: The model dimer studied by Collison and Spano with highlighted intramolecular and intermolecular charge transfers.

## 4.4 The role of intermolecular charge transfer interactions

In a recent paper Spano and Collison studied non-chiral aggregates of squaraine dyes characterized by an absorption spectrum showing prominent absorption features both to the red and to the blue of the monomer absorption spectrum.[14]. They ascribed this observation to the presence of a charge transfer (CT) interaction between adjacent molecules. This work inspired us to investigate intermolecular CT as a source of the anomalous spectral features observed in our chiral aggregates. Specifically, Spano and Collison, considered a dimer structure as in Fig. 4.7, and accounted for a CT interaction between the adjacent D and A sites located in the two different molecules. Indeed other structures can also be considered, including e.g. those drawn in Fig. 4.5a.

Of course, when accounting for intermolecular CT interaction the basis must be enlarged to account for states with charge separation between the two molecules, so that in addition to the 9 localized states in Eq. 4.9, other states enter into play. Specifically, Spano and Collison proposed to add the states obtained considering that each dye could be in any of the following states:

$$\begin{aligned} &\mathrm{D^{+}AD} && |C_1\rangle \\ &\mathrm{DAD^{+}} && |C_2\rangle \\ &\mathrm{D^{+}A^{-}D^{+}} && |C_3\rangle \\ &\mathrm{DA^{-}D} && |A\rangle \end{aligned} \tag{4.10}$$

with $C_n$ states bearing a positive charge (cations) and $A$ bearing a negative charge (anion). Of course dimer states must be overall neutral so that one adds 6 states to the 9 localized states in Eq. 4.9, for a grand total of 15 states.

While Spano and Collison definitely had the good intuition about the possible role of intermolecular CT in squaraine aggregates, the adopted basis is far from complete. Indeed they fully disregard the electronic spin degrees of freedom, basically building a model that implicitely treats electrons as spinless fermions. This is easily understood adopting the valence-bond basis where electrons are paired in singlet states.[123, 124] Fig. 4.8 shows a very simple example referring to a state with two zwitterionic molecules, indeed a state that is already present in the localized basis as state $|Z_2Z_1\rangle$. If CT interactions are disregarded, electrons can only be paired within each single molecular unit (the basis states defined as direct product of the three basis state for each dye constitute a complete basis set), but, if CT interactions are accounted for, a second state must be considered to account for the two different possibilities to pair electrons in singlet states.[123, 124]

The valence bond basis, constructed accounting for the subspace with total spin zero, would correspond to the smallest basis for our system. However a problem arises since the valence bond basis is non-orthonormal, making the procedure to calculate observables and transition dipole fairly cumbersone. We therefore adopt a simpler approach, using the so-called real-space basis, where electrons are accomodated in the different D/A site, selecting only states with $S_z = 0$, where $S_z$ measures the total spin component along the z direction. The real space basis is larger than the valence bond-basis, but, in view of the fairly complex calculations required for CD spectra (see Section 4.7) we stick on it for our calculations. Specifically, the real space basis for a squaraine dimer comprises 53 basis states, represented in the bit-representation by integer numbers, as shown in Fig.

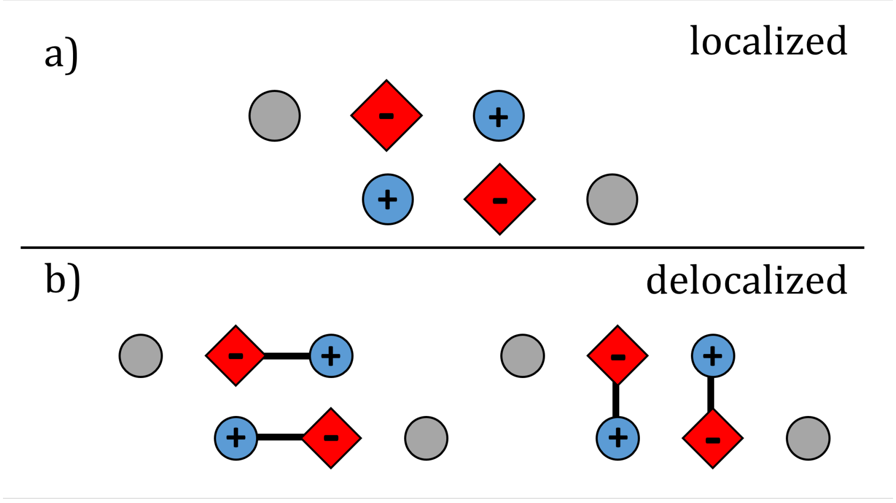

Figure 4.8: a) Example of bi-zwitterionic state as proposed by Spano and coworkers; b) When intermolecular charge delocalization is taken into account, two singlet states are needed to represent the same charge distribution.

4.9

To proceed, we must define the Hamiltonian accounting for intra and intermolecular CT and for electrostatic intermolecular interactions. We propose a Hubbard-like Hamiltonian as follows:

$$\begin{aligned}\hat{H} &= \sum_m \sum_i \varepsilon_i \hat{n}_i^m + \frac{U}{2} \sum_m \sum_i \hat{n}_i^m (\hat{n}_i^m - 1) + \frac{1}{2} \sum_{mn} \sum_{ij} V_{ij}^{mn} \hat{q}_i^m \hat{q}_j^n (1 - \delta_{ij}) \\ &\quad -t \sum_m \sum_{i \neq j} \left( \hat{b}_{ij}^m + \hat{b}_{ij}^{\dagger m} \right) - \beta \sum_{m,m+1} \sum_{ij} \left( \hat{b}_{ij}^m + \hat{b}_{ij}^{\dagger m} \right) \end{aligned} \tag{4.11}$$

where $\hat{n}_i^m$ counts the electrons on site $i(= 1, 2, 3)$ of molecule $m$, $\hat{q}_i^m$ measures the on-site charge with $\hat{q}_i^m = 2 - \hat{n}_i^m$ for sites D ($i$ =1 or 3) and $\hat{q}_i^m = -\hat{n}_i^m$ for sites A ($i$ =2). Moreover, $n_i^m = \sum_\sigma \hat{c}_{i\sigma}^{\dagger m} \hat{c}_{i\sigma}^m$ counts the electrons on site $i$ of molecule $m$ and $\hat{c}_{i\sigma}^{\dagger m}$ and $\hat{c}_{i\sigma}^m$ create and annihilate and electron with spin $\sigma$ on site $i, m$. Intramolecular and intermolecular CT are defined by the hopping integrals $t$ and $\beta$ with the hopping operator (an anti-Hermitian operator) defined as $\hat{b}_{ij}^{mn} = \sum_\sigma \hat{c}_{i\sigma}^{\dagger m} \hat{c}_{j\sigma}^n$. At variance with the Hamiltonian in Eq. 4.6, in this Hamiltonian both inter and intramolecular electrostatic

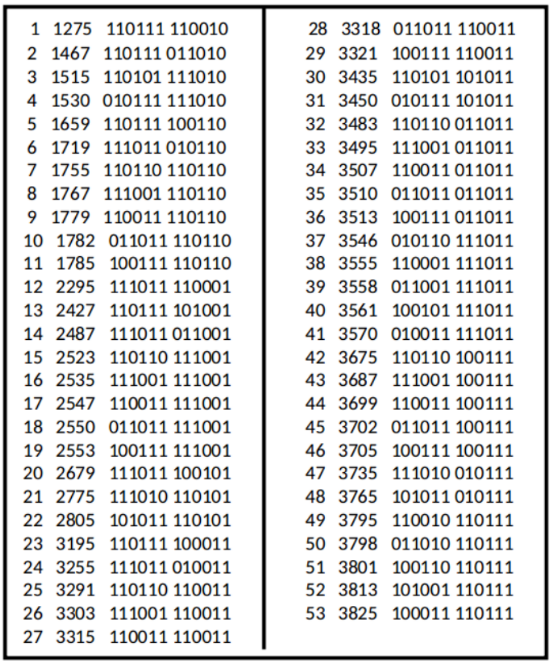

| | | |
|---|---|---|
| 1 | 1275 | 110111 110010 |
| 2 | 1467 | 110111 011010 |
| 3 | 1515 | 110101 111010 |
| 4 | 1530 | 010111 111010 |
| 5 | 1659 | 110111 100110 |
| 6 | 1719 | 111011 010110 |
| 7 | 1755 | 110110 110110 |
| 8 | 1767 | 111001 110110 |
| 9 | 1779 | 110011 110110 |
| 10 | 1782 | 011011 110110 |
| 11 | 1785 | 100111 110110 |
| 12 | 2295 | 111011 110001 |
| 13 | 2427 | 110111 101001 |
| 14 | 2487 | 111011 011001 |
| 15 | 2523 | 110110 111001 |
| 16 | 2535 | 111001 111001 |
| 17 | 2547 | 110011 111001 |
| 18 | 2550 | 011011 111001 |
| 19 | 2553 | 100111 111001 |
| 20 | 2679 | 111011 100101 |
| 21 | 2775 | 111010 110101 |
| 22 | 2805 | 101011 110101 |
| 23 | 3195 | 110111 100011 |
| 24 | 3255 | 111011 010011 |
| 25 | 3291 | 110110 110011 |
| 26 | 3303 | 111001 110011 |
| 27 | 3315 | 110011 110011 |
| 28 | 3318 | 011011 110011 |
| 29 | 3321 | 100111 110011 |
| 30 | 3435 | 110101 101011 |
| 31 | 3450 | 010111 101011 |
| 32 | 3483 | 110110 011011 |
| 33 | 3495 | 111001 011011 |
| 34 | 3507 | 110011 011011 |
| 35 | 3510 | 011011 011011 |
| 36 | 3513 | 100111 011011 |
| 37 | 3546 | 010110 111011 |
| 38 | 3555 | 110001 111011 |
| 39 | 3558 | 011001 111011 |
| 40 | 3561 | 100101 111011 |
| 41 | 3570 | 010011 111011 |
| 42 | 3675 | 110110 100111 |
| 43 | 3687 | 111001 100111 |
| 44 | 3699 | 110011 100111 |
| 45 | 3702 | 011011 100111 |
| 46 | 3705 | 100111 100111 |
| 47 | 3735 | 111010 010111 |
| 48 | 3765 | 101011 010111 |
| 49 | 3795 | 110010 110111 |
| 50 | 3798 | 011010 110111 |
| 51 | 3801 | 100110 110111 |
| 52 | 3813 | 101001 110111 |
| 53 | 3825 | 100011 110111 |

Figure 4.9: The 53 diagrams composing the real state basis for a squaraine dimer. The first column numbers the diagrams, the second and third columns are the integer numbers representing each basis state in decimal and binary representation, respectively. Each of the 6 sites is represented by two digits in the binary number, 00 stands for a vaccum site, 01 and 10 for a spin up and a spin down electron, respectively, 11 for a doubly occupied site. In other terms, for each site, the first digit counts the number of spin down, the second digit counts the number of spin up.

interactions are accounted for, with $V_{ij}^{mn}$ designed as in Eq. 4.8. To ensure that the Hubbard Hamiltonian in the above equation reduces to the Hamiltonian in Eq. 4.6 for $\beta = 0$ we set $t = \tau/\sqrt{2}$ and fix on site energies so that $2z_0 = 2\varepsilon_i - U - V$ where $V = V_{12}^{mm} = V_{23}^{mm}$ is the modulus of the electrostatic interaction between charges on D and A sites in the same molecule (of course fully defined by the D-A distance). Finally, we set $U$, the repulsion between two electrons residing on the same site, to a very large value as to make its value irrelevant, and to ensure that states with doubly charged site $D^{2+}$ and $A^{2-}$ have very large energies and can be safely disregarded.

The above Hamiltonain is written and diagonalized on the real-space basis to get relevant eigenstates and eigenvalues. The calculation of absorption spectra only requires the definition of the dipole moment operator, that reads:

$$\hat{\vec{\mu}} = -\sum_m \sum_i \vec{r}_i^{\,m} \hat{n}_i^m \tag{4.12}$$

where $\vec{r}_i^{\,m}$ is the position vector for site $i$ of molecule $m$. On the chosen basis the dipole moment operator is diagonal. To calculate absorption spectra we calculate transition dipole moments from the ground to the excited states and calculate absorption spectra assigning a Gaussian lineshape with width $\sigma = 0.08$ to each transition:

$$A(\omega) \propto \hbar\omega \sum_E |\, \langle E|\hat{\mu}|G\rangle \,|^2 e^{\frac{-(\hbar\omega - \hbar\omega_E G)^2}{2\sigma^2}} \tag{4.13}$$

Fig. 4.10 shows absorption spectra calculated for two different dimers with aligned molecules with exactly the same model parameters as in Fig4.5 but introducing a finite $\beta = 0.6$. It is clear that for both dimers, accounting for intermolecular CT interactions leads to a splitting of the band with the appearance of two transitions, one to the blue and one to the red of the monomer absorption band. We observe that the absorption spectrum arising from the configuration B is very similar to experimental data presented in Fig. 4.2.

To better understand the nature of the double picked absorption spectrum we give a closer look to the transion dipole moments. Specifically, we calculate absorption spectra of the dimer in Fig. 4.10B accounting for polarized radiation. We oriented the dimer in order to have the molecules aligned along the x-axis and packed along z. The dipole moment of transitions lead by intramolecular CT (term $\tau$) will be parallel to x-axis

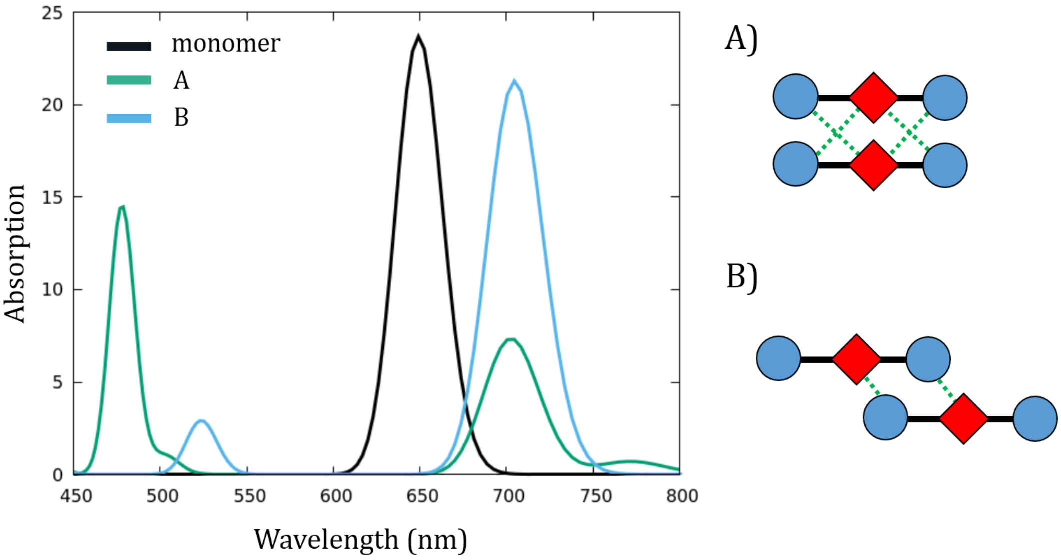

Figure 4.10: Absorption spectra (left) for a model squaraine dimer in the same configurations introduced in Fig. 4.5, compared to the monomer. The CT interactions taken into account for each configuration are depicted with green dashed lines.

(same direction of the D-A arms), while intermolecular CT (term $\beta$) will be concordant with the packing direction, the z-axis. In Fig. 4.11 the total absorption spetrum of the dimer (top panel) is plotted together with absorption spectra obtained with x- and z-polarized light (middle and bottom panels). It is evident how the intensity of both transitions is governed by intramolecular, rather than intermolecular, charge migration. The two characteristic transitions seen in CT dimers arise from the mixing of CT and exciton states. However the CT weight in the ground state is negligible so that CT states do not contribute to the intensity of transitions from the ground state. In other terms the intensity of the localized transition redistributes in two states, the red and the blue band.

## 4.5 Calculation of CD spectra of aggregates with delocalized electrons

Results in the previous section suggests that accounting for intermolecular CT interaction is probably the key to understand the strange spectroscopic behavior of chiral squaraine aggregates. However, to proceed we must attack a non-trivial problem, i.e. the calculation of CD spectra in a molecular aggregate where, due to intermolecular CT interactions, electrons are not localized on the molecular units. This makes it impossible to use the approach described in Section 4.3 that, based on the classical Condon work,[91] relies on the definition of the aggregate dipole moment as the sum of molecular dipole moments. This approach of course is inadequate for delocalized electrons.

According to Condon[91], CD spectra can be calculated from the rotational strength associated to each transition $R_i$. The rotational strength plays for CD spectra the same role as the oscillator strength in absorption spectra, so that CD spectra can be calculated, once the $R_i$ are known for each transition assigning a spectral bandshape (typically Gaussian or Lorentzian) to each transition. If $|g\rangle$ is the ground state the rotational strength for the $|g\rangle \rightarrow |f\rangle$ transition is

$$R_f = \mathrm{Im}\Big\{ \langle g|\hat{\mu}|f\rangle \cdot \langle f|\hat{M}|g\rangle \Big\} \tag{4.14}$$

where $\hat{\mu}$ and $\hat{M}$ are the electric and magnetic dipole operators, respectively. While

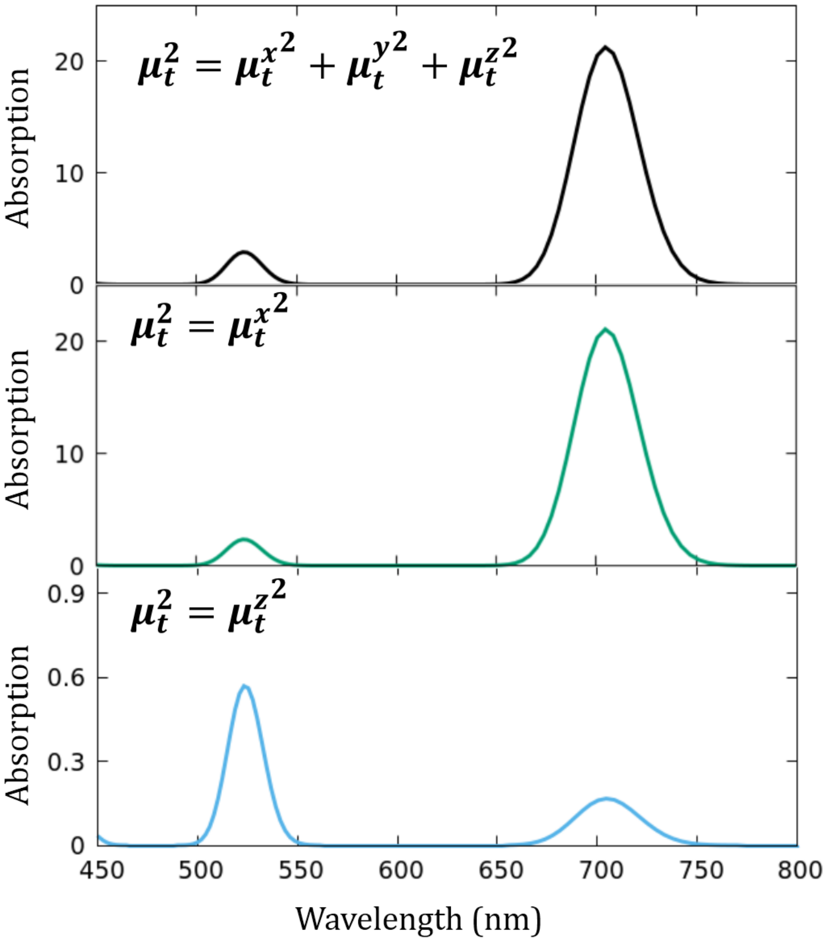

Figure 4.11: Top panel: absorption spectrum of dimer in Fig. 4.10B. Middle panel: absorption calculated for the same system with radiation polarized along the x-axis. Bottom panel: absorption calculated for the same system with radiation polarized along the z-axis.

the definition of electric dipole moment operator is straightforward (see Eq, 4.12), the definition of the magnetic dipole moment operator is more delicate. The magnetic dipole is proportional to the total angular momentum:

$$\hat{\vec{M}} \propto -\hat{\vec{L}} = -\sum_k \hat{\vec{l}}_k \tag{4.15}$$

where $k$ runs on all electrons. The angular momentum of $k$-electron is related to its linear momentum $\hat{\vec{p}}_k$ by

$$\hat{\vec{l}}_k = \hat{\vec{r}}_k \times \hat{\vec{p}}_k \tag{4.16}$$

Finally the linear momentum can be obtained as

$$\hat{\vec{p}}_k = -\frac{i}{\hbar}\Big[\hat{\vec{\mu}}_k, H\Big] \tag{4.17}$$

The problem is that in a real-space description we cannot address the properties of a single electron. To overcome the problem we start evaluating the total linear momentum. For the sake of clarity we explicitly write the expression for only one of the three components:

$$\hat{P}_x = -\frac{i}{\hbar}[\hat{\mu}_x, H] \tag{4.18}$$

where $\hat{\mu}_x$ is the $x$ component of the total dipole moment in Eq. 4.12. The dipole moment operator commutes with the first three terms of the Hamiltonian in Eq. 4.11, while it does not commute with the hopping terms. Overall

$$\hat{P}_x = \frac{i}{\hbar}\sum_{mn}\sum_{ij}\delta_{i,j\pm1}\Big\{(x_j^n - x_i^m)\hat{v}_{ij}^{mn}\Big[\tau\delta_{mn} + \beta(1-\delta_{mn})\Big]\Big\} \tag{4.19}$$

where the bond velocity is an anti-Hermitian operator

$$\hat{v}_{ij}^{mn} = \hat{b}_{ij}^{mn} - \hat{b}_{ij}^{\dagger mn} = \hat{b}_{ij}^{mn} - \hat{b}_{ji}^{nm} \tag{4.20}$$

If we calculate $\hat{\vec{R}} \times \hat{\vec{P}}$, where $\hat{\vec{R}}$, the global position operator, is identical to the total dipole moment operator in Eq. 4.12, we do not get the total angular momentum in Eq. 4.15, as $\vec{R} \times \vec{P}$ does contain both one-electron and two-electron terms. We then define $\hat{\vec{L}}$ selecting out of the $\hat{\vec{R}} \times \hat{\vec{P}}$ operator only the one-electron terms. Accordingly:

$$\begin{aligned}\hat{L}_x = \; & -\frac{i}{\hbar}\sum_{mn}\sum_{ij}\delta_{i,j\pm1}\Big\{\Big[(z_j^n - z_i^m)(y_i^m\hat{b}_{ij}^{mn} - y_j^n\hat{b}_{ji}^{nm}) \\ & -(y_j^n - y_i^m)(z_i^m\hat{b}_{ij}^{mn} - z_j^n\hat{b}_{ji}^{nm})\Big]\Big[\tau\delta_{mn} + \beta(1-\delta_{mn})\Big]\Big\}\end{aligned} \tag{4.21}$$

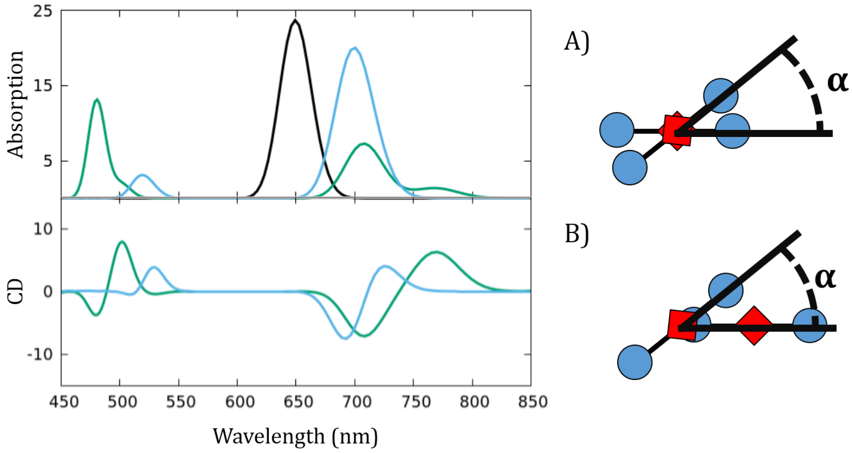

Figure 4.12: Absorption (top left) and CD (bottom left) spectra for a model squaraine dimer in the same configurations introduced in Fig. 4.6.

Analogous expressions for $\hat{L}_y$ and $\hat{L}_z$ can be obtained upon ciclic permutation of $x$, $y$ and $z$ indices. Remembering that $-\hat{\vec{L}} \propto \hat{\vec{M}}$ we are now in the position to calculate rotational strengths using the canonical expression:

$$R_f = Im\Big\{ \langle g|\hat{\mu}|f\rangle \cdot \langle f|\hat{M}|g\rangle \Big\} \tag{4.22}$$

Fig. 4.12 shows absorption and CD spectra for the same model dimer represented in Fig. 4.6, but accounting for CT interactions, with $\beta = 0.6$. We verified explicitly that settin $\beta = 0$ callculated spectra coincide with those obtained in Fig. 4.5, exploiting the standard Condon approach for localized electrons.

The results in Fig. 4.12 are inspiring: for both dimers in fact two CD doublets are seen at the location of the J and H bands seen in the absorption spectrum, suggesting that intermolecular CT interactions may be the key to understand the observed spectroscopic behavior of chiral squaraine aggregates. To proceed however we need information about the structure of the aggregates, a problem that will be attacked using the tools of MD.

## 4.6 Molecular Dynamics modeling of chiral squaraine aggregates

### 4.6.1 Definition of a force field

The geometry of both ProSQ-RR and SS stereoisomers (see Fig. 4.3) are optimized in two steps. In the first optimization only the $\pi$-conjugated *"core"* of the molecule is taken into account and an optimization with constrained geometry was performed (point group $D_{2h}$). Then another optimization is made freezing the molecular cores in the optimized geometry and adding the stereocenters at both ends (RR or SS). RESP atomic charges were obtained for the optimized geometries. All calculations were performed at B3LYP 6-31G** level of theory (g16 package). On the basis of these results, a GAFF force field[125] was defined (see Appendix B for further clarifications), employing antechamber tools.

### 4.6.2 Enhanced sampling MD on tetramers

We studied the aggregation in solution of four ProSQ- RR and four ProSQ-SS molecules in two solvents (NPT ensamble):

- **60:40** Methanol / Water solution 60/40 (v/v)
- **MeOH** Pure Methanol

Simulation boxes were set up using a size of $5 \times 5 \times 5$ nm$^3$. After obtaining equilibrated sample, Hamiltonian Replica Exchange MD (hrexMD) simulations (see Appendix B) were run on 16 replica of the same systems, in order to accelerate the sampling and produce reliable geometries for the tetramer aggregates. Specifically, a first 30 ns hrexMD was first run on both RR and SS, followed by other 50 ns on each systems. To have a better understanding of the supramolecular structures, a data-science based algorithm (Advanced Density Peak) was employed and structures from the trajectories were assigned to belong to a "cluster", a region of the coordinates space characterizing a type of aggregate. The density peaks of such region, i.e. the center of the cluster, correspond then to a statistically representative structure. These were found for both RR and SS enantiomer. In both solvents, the largely dominant structure is constituted by an helix arrangement of units. Most stable structures are reported in Fig. 4.13. For both ProSQ-RR and SS the most abundant structure is a right-handed and left-handed helix respectively. Since the two enantiomeric species have perfectly mirror structures, we focused further investigations on the ProSQ-SS enantiomer.

### 4.6.3 Selection of statistically representative structures

In order to quantitatively describe the aggregates, we defined a set of independent parameters defining the reciprocal orientation of molecules. Three parameters were identified for all pairs of adjacent molecules:

- $d$, the distance between molecular planes
- $\theta_S$, the shift angle between molecules
- $\theta_T$, the tilt angle between molecules

The determination of these parameters is achieved mapping the molecular structures of Fig. 4.3 with the sketched quadrupolar scheme in Fig. 4.1b. In particular, the acceptor group is identified in the geometric center of the squaryl ring, while the donor groups are superimposed to the conjugated carbon next to the aniline nitrogens (see Fig. 4.14).

The parameter $d$ is obtained as the the distance between closest donor groups of adiacent units. $\theta_S(i,j)$ is determined measuring the angle between a donor-acceptor couple pertaining to the $i$ molecule and the acceptor of the $j$th molecule (Fig. 4.15b). Since the two donor arms of squaraines are undistinguishable, the distribution is built considering both possible angles. What's expected is an almost symmetric distribution, picked at $\theta_S$ and $\pi - \theta_S$. Finally, the angle $\theta_T$ is defined as the dihedral angle spanned by two squaraine arms (Fig. 4.15c). Fig. 4.16 plots the histograms relative to the three geometric parameters, accounting for the 3 nearest neighbors pairs of the tetramer. For the distance $d$ distribution we see a broad peak centered at $\sim 4.5$ $\AA$, that marks the $\pi-\pi$ stacking aggregation between units. The shift angle distribution reveals the presence of two peaks at $\theta$ and $\pi - \theta$, as expected, with a most recurrent value of 51.5° for $\theta_S$. Finally, the tilt angle distributon shows three distributions peaked at 31.5°. The three parameters found are sufficient to completely determine the geometry of the “average dimer” and hence to calculate absorption and CD spectra.

## 4.7 Chiral aggregates of squaraine dyes: absorption and CD spectra

We calculate dimer spectra using the Hamiltonian defined in Eq. 4.11. As already discussed in Section 4.3 we set $\tau = -1.2eV$, $z = 0.2eV$ and we fixed the donor acceptor distance (the quadrupolar arm) to $a = 5.3\AA$ and $n^2 = 4$. In Fig. 4.17 the spectrum of the monomer is compared to dimer spectra with different CT integral $\beta$. Absorption spectra show the double peaked signature deriving from CT interactions. As expected, the energy difference between the bright states increases as the $\beta$ integral becomes higher. CD spectra show two well resolved bisignated doublet, that follow the trend of absorption spectra. It is important to notice how the high energy doublet gains rotational strength with increasing $\beta$. This effect is in agreement with Fig. 4.11, from which it clear how the majority of oscillator strength generated by intermolecular interactions belongs to the blueshifted band. Reiterating the roto-translations used to generate the “average dimer”, we are also able to build higher dimensionality clusters. The problem arising when increasing the number of molecules is of course related to the dimension of the real-space basis. For this reason we restrict analysis of bigger systems to the trimer (707 basis states) and the tetramer (10453 basis states). Absorption and CD spectra for the trimer and tetramer are shown respectively in Fig. 4.18 and 4.19. While results for $\beta = 0.4$ are similar to what seen for the dimer, as the CT integral increase, the interpretation of absorption and CD spectra becomes trickier. The increase of the basis set implies a large number of excited states.As a consequence, even though the energy window remains more or less the same, the total spectra embody contributions from a large amount of transitions. Nevertheless, in both the trimer and the tetramer, the low energy peaks remain well resolved, both in absorption and CD spectra.

Calculated absorptions in Fig. 4.17 are satisfactory as they allow to understand the physical origin of the so called H and J bands in absorption spectra and the appearence of two bisignated CD signals in the CD spectrum. However a closer look to the CD spectra show a discrepancy in the sign of the high energy bisignated band. The reason of this difference can be possibly attributed to complex mechanisms occurring upon aggregation. In fact, as already discussed in a previous work by Jyothish et al.[112], the supramolecular assembly of chiral squaraine derivatives heavily depends on the conditions applied. They report, for the same system, the formation of aggregates with opposite CD spectra depending on the good/poor solvent ratio and temperature. Extensive aggregation studies at variable temperature allow the authors to ascribe the experimental observation of the inversion of CD signal at increasing temperature to different structures of aggregates formed under kinetic and thermodynamic control. Indeed, the analysis presented in Section 4.6, deriving from Molecular Dynamics simulation, allow the identification of only the thermodynamic stable assembly. Conversely, aggregates obtained experimentally might be formed under kinetic control. Further investigations are proceeding in order to get a more detailed insight of these peculiar systems.

## 4.8 Conclusions

In this chapter the spectroscopic and supramolecular features of squaraine aggregates have been extensively investigated. In particular, we focused our study on a novel class of squaraine chiral derivatives, named ProSQ, that show unique absorption and circular dichroism spectra upon aggregation. The presence in these molecules of peripheral chiral chains leads to the formation of helical supramolecular clusters. Through accurate MD modelization, we were able to study aggregation of ProSQ units, obtaining reliable geometries for the interacting monomers. We then presented a new model to describe squaraine aggregates accounting for electrostatic and CT intermolecular interactions. The model proposed, offers an accurate description of spectroscopic properties of these complex supramolecular systems. In particular, the parametrization of the electronic Hamiltonian with geometric outcomes extracted from MD trajectories returns spectra in good agreement with experimental data.

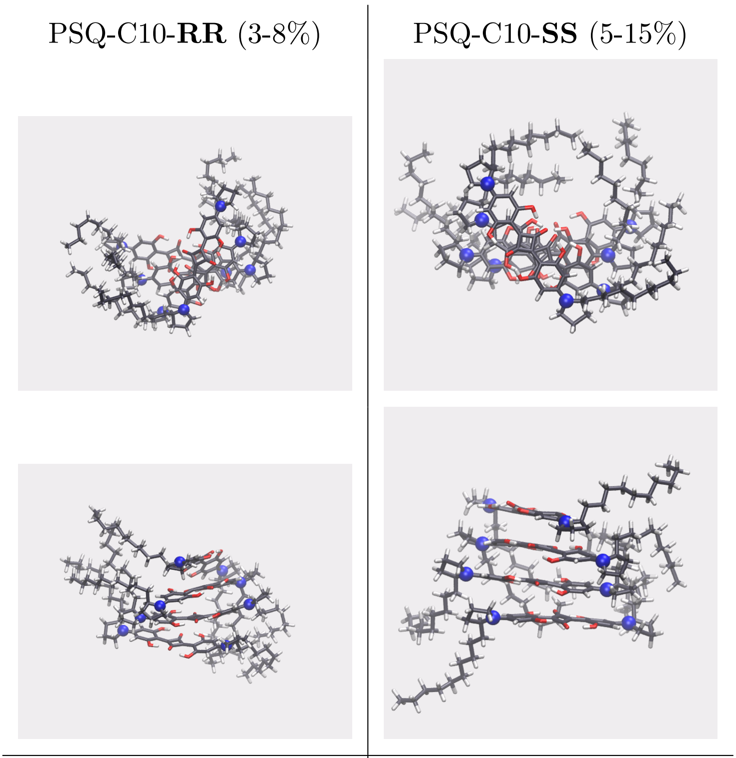

PSQ-C10-**RR** (3-8%)

PSQ-C10-**SS** (5-15%)

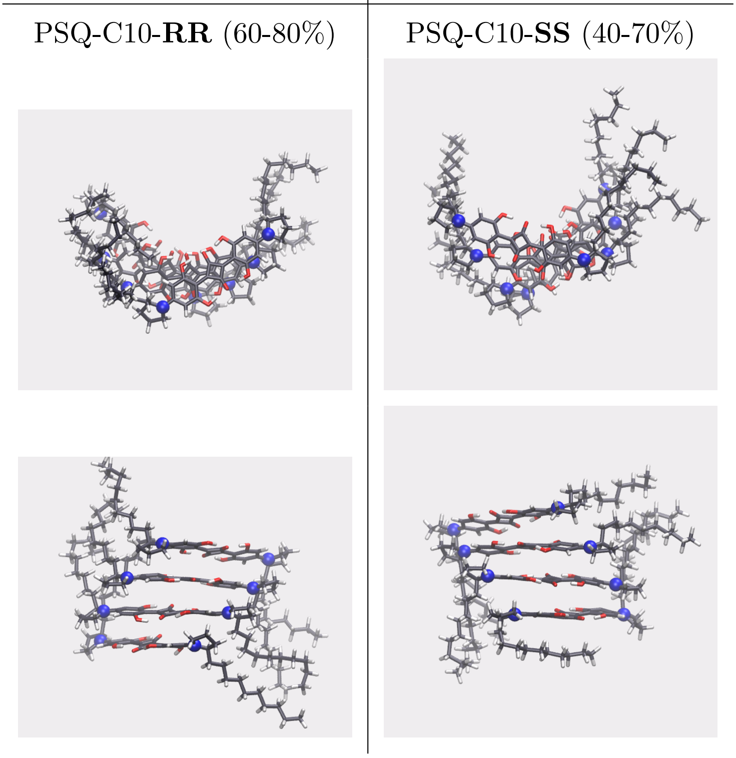

PSQ-C10-**RR** (60-80%)

PSQ-C10-**SS** (40-70%)

Figure 4.13: Most stable conformers of PSQ-C10-**RR** (left) and -**SS** (right) tetramers, two each.

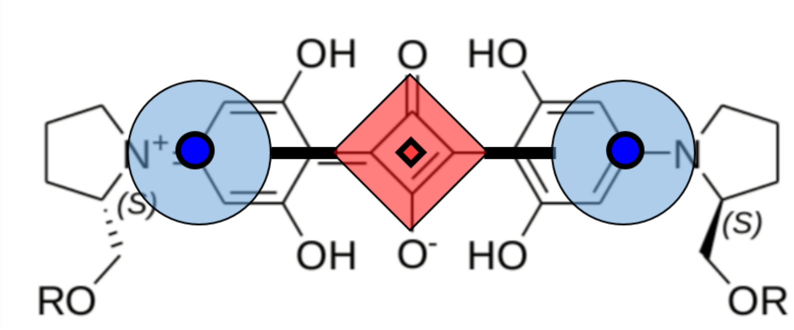

Figure 4.14: Modelization of Prosq-SS into a schematic representation of DAD quadrupolar dye (same modelizazion applies to ProSQ-RR).

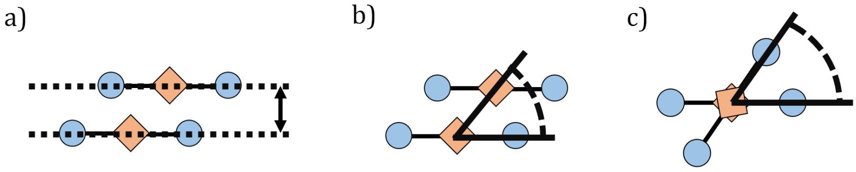

Figure 4.15: The three parameters used to define relative orientation of squaraine pairs. From lefto to right: plane distance $d$, shift angle $\theta_S$ and tilt angle $\theta_T$

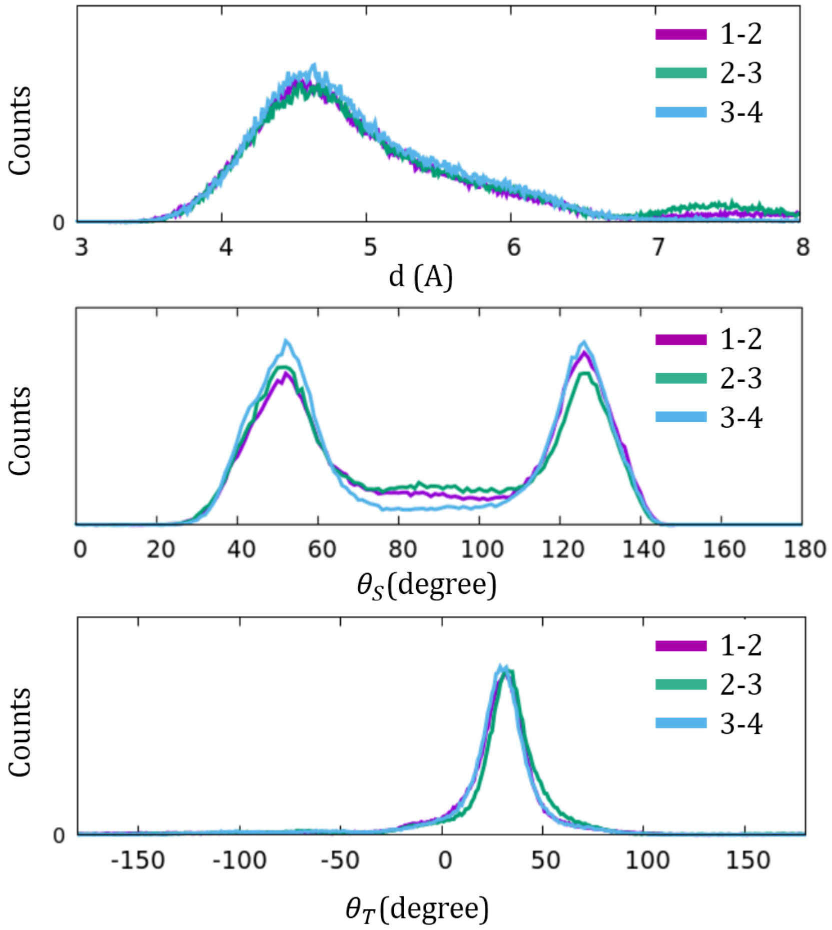

Figure 4.16: Histograms representing the distribution of the three geometric parameters. From top to bottom: $d$, $\theta_S$ and $\theta_T$. In each panels the distribuions relative to the 3 nearest neighbors pairs of the tetramer are shown.

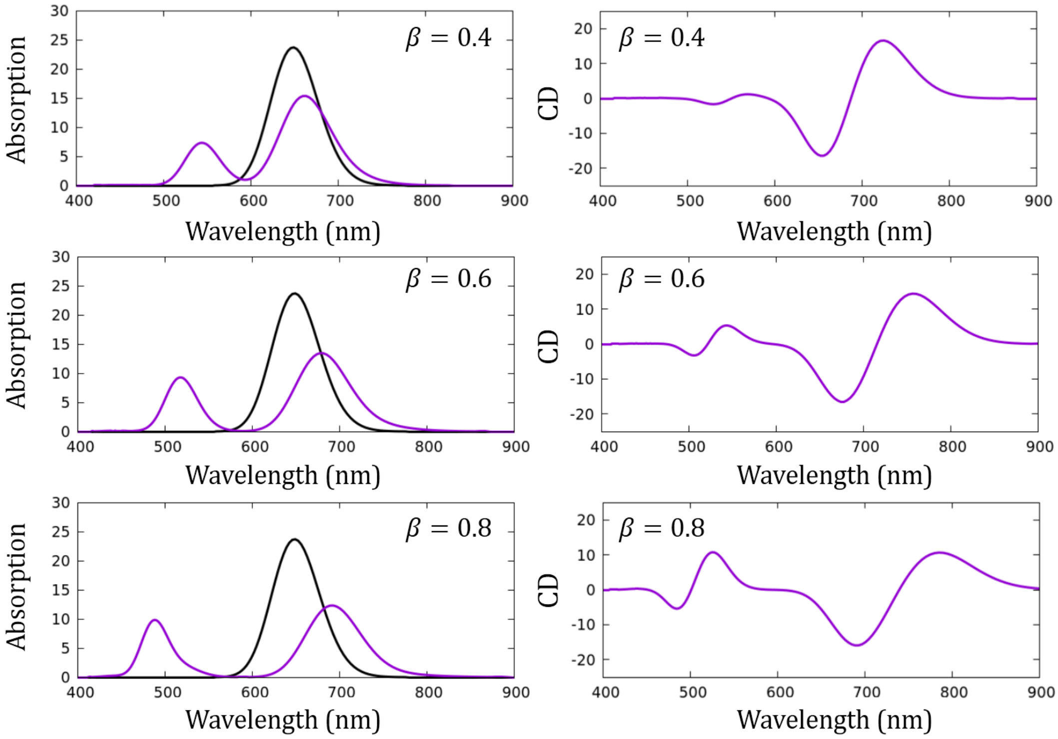

Figure 4.17: Dimer absorption (left) and CD spectra (right) calculated for different value of intermolecular Charge Transfer integral $\beta$.

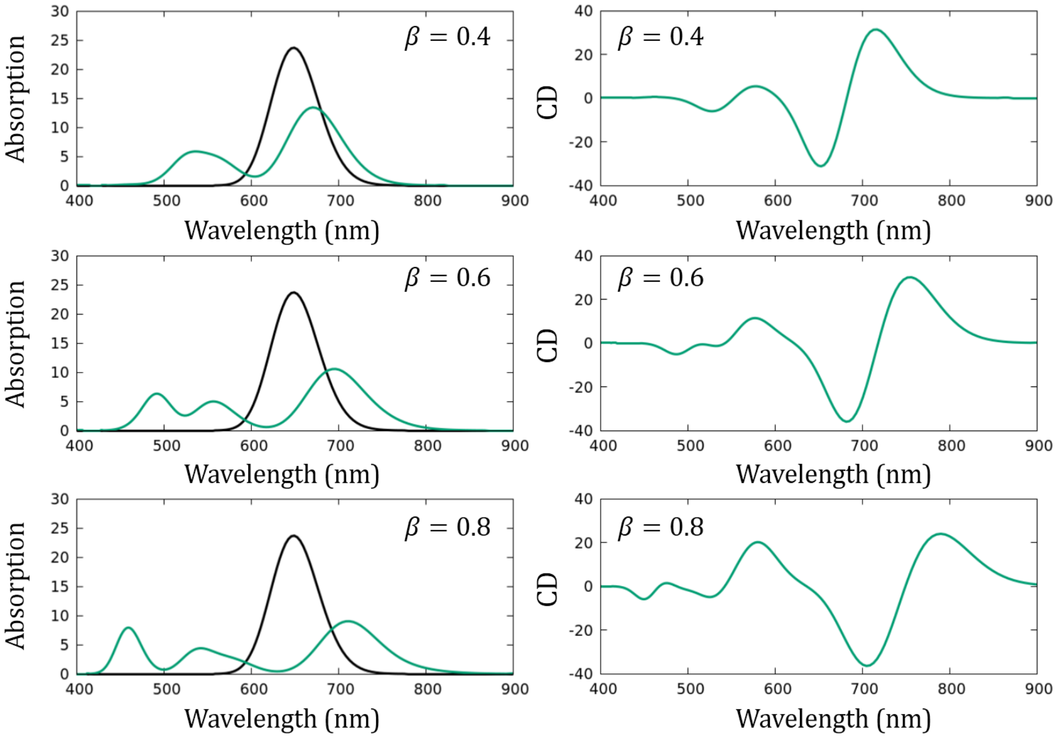

Figure 4.18: Trimer absorption (left) and CD spectra (right) calculated for different value of intermolecular Charge Transfer integral $\beta$.

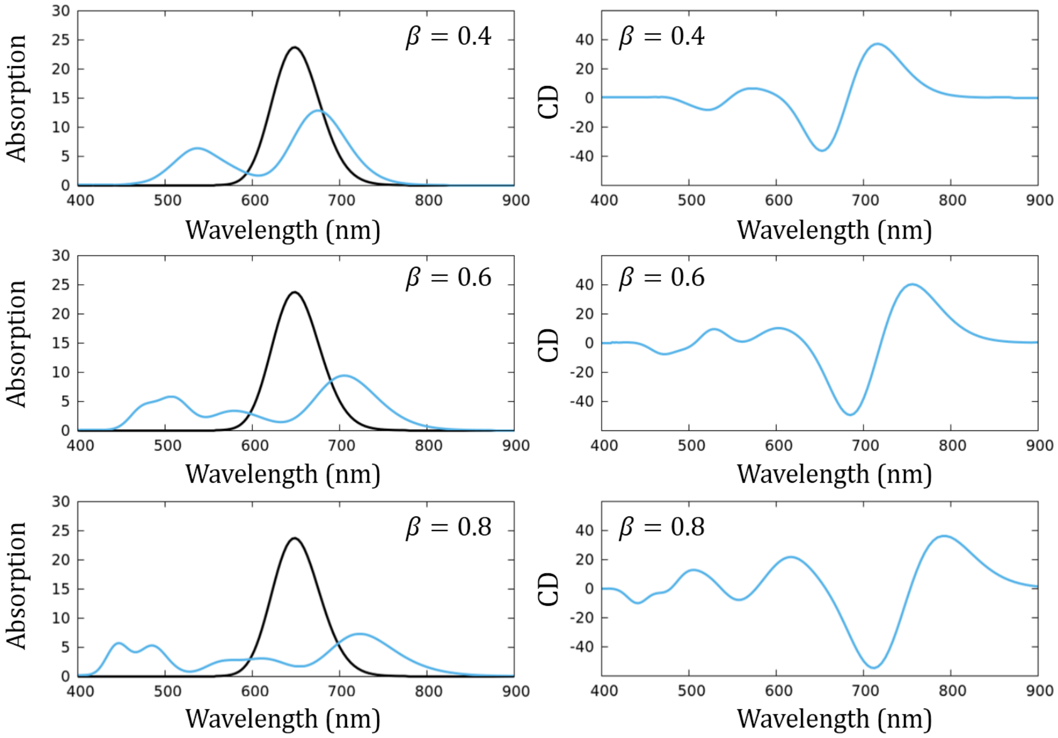

Figure 4.19: Tetramer absorption (left) and CD spectra (right) calculated for different value of intermolecular Charge Transfer integral $\beta$.

# Conclusions

In this Thesis we extensively discussed intermolecular electrostatic interactions with special emphasis on molecular aggregates and FRET. The presented theoretical work provides a series of tools with the purpose of improving the description of complex supramolecular systems. Specifically, we demonstrated how the combined use of MD, exciton and essential state models can provide interesting results and a reliable description of optical properties of a variety of systems.

In the first part of the dissertation we investigated, for a selected pair of chromophores, the relations between energy transfer efficiencies and slow degrees of freedom connected to conformational motion and solvation. To this aim we proposed a new computational method for the calculation of the dynamics and RET quantum yields for a RET pair in two different solvents, highlighting the importance of conformational fluctuations. Our approach, combining equilibrium and non-equilibrium MD simulations with ab-initio results, offers a detailed description of all the processes that simultaneously affect the decay rates of our system. We validated the reliability of the protocol against an extensive set of available experimental results, with very good results. This work solved a major issue related to the characterization of RET rates in systems with high flexibility, emphasizing the importance of a dynamical approach to the description of complex decay mechanisms and opening new opportunities for their theoretical treatment.

The second part of the Thesis, focused on molecular aggregates, aims to extend the portfolio of relevant models and computational techniques. We conducted a detailed study on aggregates of polar and polarizable molecules, testing different approximation approaches and their limitations. Moreover, we proposed a simple yet accountable method for the calculation of optical spectra of bidimensional aggregates, whose description is usually very complex. With respect to chiral molecular aggregates, we extensively investigated spectroscopic and supramolecular features of two systems, where the subtle interplay between intermolecular electrostatic interactions and chiral supramolecular arrangements results in non-obvious outcomes. Specifically, we focused attention on aggregates of non-polar and quadrupolar chromophores. We suggested a novel approach for the characterization of a family of dicyanostilbenes derivatives (non-polar). The hybrid method proposed, based on the combination of MD simulations and exciton models, simulates well the chiroptical properties observed experimentally. As for aggregates of quadrupolar dyes, a group of squaraines chiral derivatives, showing unique absorption and circular dichroism spectra upon aggregation, have been investigated. Through accurate modelization, we were able to mimic the supramolecular arrangements of the molecular units by the use of molecular dynamics simulations, We then presented a new model, able to account for CT intermolecular interactions, that offers an accurate tool for the description of spectroscopic properties of squaraine aggregates in solution.

To conclude, this Thesis offers new theoretical approaches for the description of intermolecular electrostatic interactions that are of outstanding importance in the field of innovative molecular materials. Complex mechanisms, such as resonant energy transfer and charge transfer interactions, have been investigated in a completely different light, leading to a more profound understanding of their properties and opportunities.

# Appendix A

# Molecular Aggregates

## A.1 Oscillator Strength: sum rule

To relate the total oscillator strength of a system to a ground-state expectation value, we define the velocity dipole operator, $\hat{v}$:

$$i\hbar\hat{v} = [\hat{\mu}, \hat{H}], \tag{A.1}$$

where, to simplify the notation, we have suppressed the vector notation on both $\hat{v}$ and $\hat{\mu}$ operators. The oscillator strength associated with the $G \to E$ transition is:

$$f_{EG} = \frac{2}{3}\frac{m_e}{\hbar e^2}\omega_{EG}\langle G|\hat{\mu}|E\rangle\langle E|\hat{\mu}|G\rangle. \tag{A.2}$$

To eliminate the transition frequency from the above expression we use:

$$i\langle G|\hat{v}|E\rangle = \omega_{EG}\langle G|\hat{\mu}|E\rangle \tag{A.3}$$

and its complex conjugate, thus getting:

$$F = \sum_E f_{EG} = \frac{-im_e}{3\hbar e^2}\langle G|[\hat{\mu}, \hat{v}]|G\rangle, \tag{A.4}$$

thus proving Eq.2.28 in the main text. Furthermore, using Eqs.2.26 and 2.27 (main text) and remembering the Paulions algebra (see Eq. 2.15 in the main text), the commutator

$[\hat{\mu}, \hat{v}]$ can be easily calculated. In particular, we have:

$$\begin{aligned}
[\hat{\mu}, \hat{v}] &= \frac{1}{i\hbar}\Big[\hat{\mu}, [\hat{\mu}, \hat{H}]\Big], \\
&= \frac{1}{i\hbar}\mu_0^2 \sum_i [\hbar\omega_0 - \lambda(\hat{a}_i^\dagger + \hat{a}_i)](4\hat{n}_i - 2), \qquad \text{(A.5)}
\end{aligned}$$

that is Eq.2.30 in the main text.

## A.2 Aggregates of polar dyes: additional results

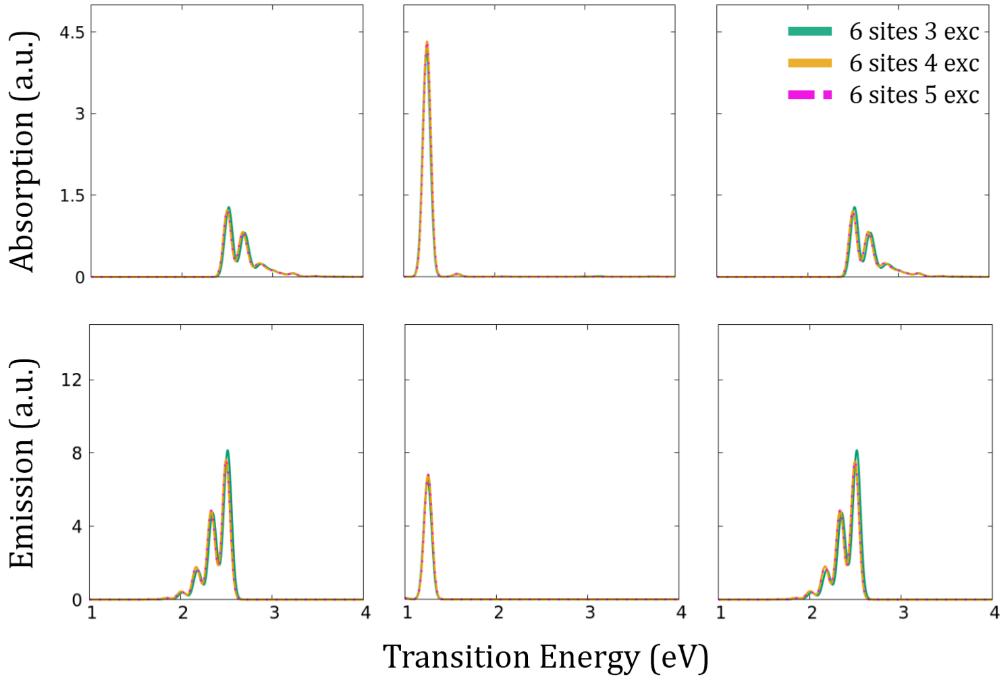

Figure A.1: The same esults as in Fig. 2.7, main text ($N = 6$), accounting for different value of $N_e$.

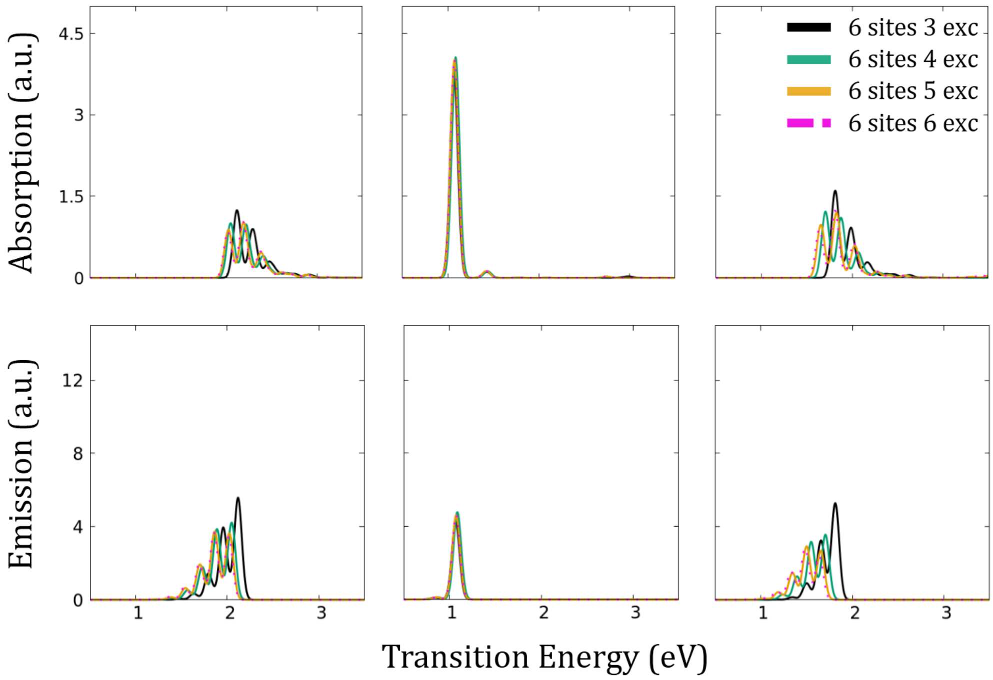

Figure A.2: The same results as in Fig. 2.8, main text ($N = 6$), accounting for different value of $N_e$.

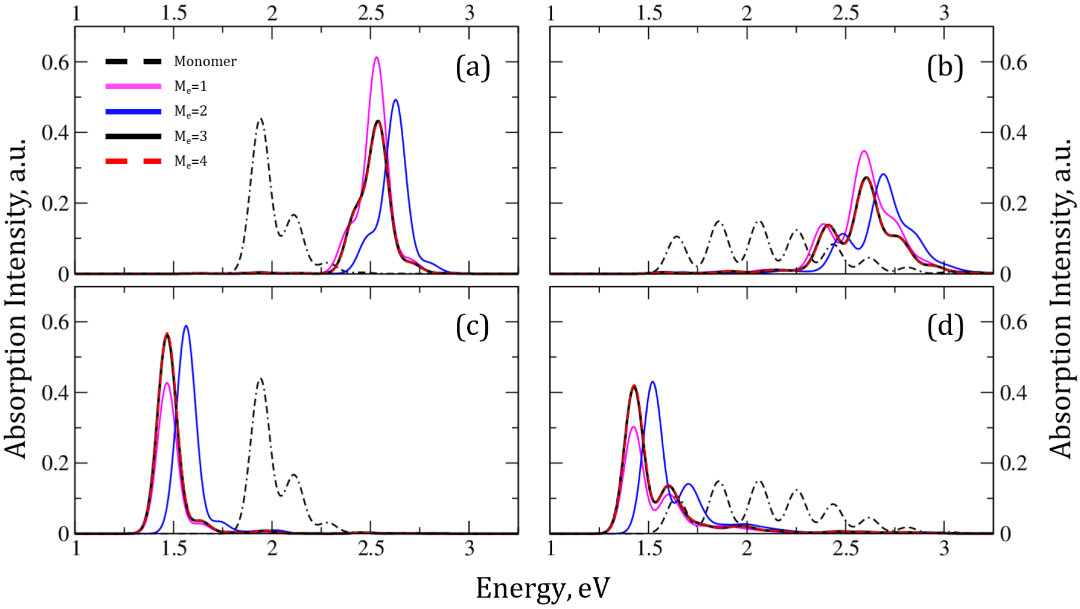

Figure A.3: The same results as in Fig. 2.11, main text, but for different electronvibration coupling strength. a) $J_1 = 0.255eV$, $\lambda = 0.10eV$; b) $J_1 = 0.255eV$,$\lambda = 0.22eV$; c) $J_1 = 0.255eV$, $\lambda = 0.10eV$; d) $J_1 = 0.255eV$, $\lambda = 0.22eV$.

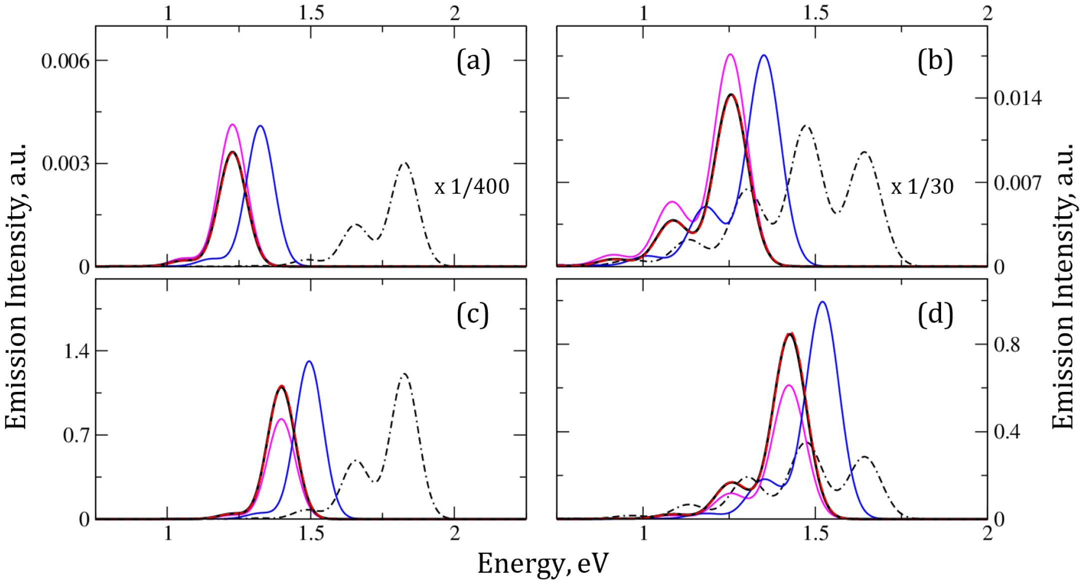

Figure A.4: The same results as in Fig. 2.11, main text, but for different electronvibration coupling strength. a) $J_1 = 0.255eV$, $\lambda = 0.10eV$; b) $J_1 = 0.255eV$,$\lambda = 0.22eV$; c) $J_1 = 0.255eV$, $\lambda = 0.10eV$; d) $J_1 = 0.255eV$, $\lambda = 0.22eV$.

# Appendix B

# Molecular dynamics

## B.1 Foundamental parameters

Classical Molecular Dynamics (MD) is a technique used to study structural and dynamical properties, including fluctuations and conformational changes in molecules and materials. It consists in a step-by-step numerical solution of classical mechanic equations, in which each atom is treated as a rigid sphere defined by a position $\vec{r_i}$, a mass $m_i$, and a fixed charge $q_i$.

$$\vec{f_i} = m_i \vec{a}_i$$

where $\vec{F}$ is the force exercised on particle $i$, and $\vec{a}_i$ is its acceleration. In MD, forces are usually derived from a potential energy $V(\vec{R})$ where $R$ run over all particles positions.

$$\vec{f_i} = \frac{\partial}{\partial \vec{r_i}} V(\vec{R})$$

The classical MD potential energy includes different terms, that can be divided into two main families depending on their nature: *bonded* and $non - bonded$, named here $V_b$ and $V_{nb}$. Bonded potential refers to all the intramolecular bonding interactions present, that are typically split into bonds, angles and dihedrals. The general expression for these kinds of potential is:

$$V_b^{\alpha} = \frac{1}{2} \sum_i k_i (\alpha_i - \alpha_0)^2$$

where the above equation represents a harmonic potential with force constant $k_i$, function of the displacement from equilibrium of the generic parameter $\alpha$ (function of 2, 3 or 4 atoms postitions depending on the nature of the variable). The above expression is used for bonds, and angles, and hence $i$ runs over all relevant terms. However for dihedral angles a periodic potential is generally implemented.

Non-bonded interactions describe interactions among particles that are not linked to each other. They are usually split into 1-,2-,..., N-body terms:

$$V_{nb} = \sum_i v'(\vec{r_i}) + \sum_{i<j} v''(\vec{r_i}, \vec{r_j}) + \dots$$

where usually three-body and higher terms are neglected, while the $v'$, a constant, is dropped. The remaining two-body potential, function of the distance $d$ between particles, is divided into a Coulombic term (depending on site charges $q_i$) and Lennard-Jones potential (depending on diameter $\sigma$ of the sphere associated to each particle):

$$v''(d) = v^C + v^{LJ} = \frac{q_1 q_2}{4\pi\varepsilon_0 d} + v_0^{LJ}\left[\left(\frac{\sigma}{d}\right)^{12} - \left(\frac{\sigma}{d}\right)^{6}\right]$$

The total energy, or Hamiltonian, of the system is $H = K + V$, where $V$ is the potential that we have just described, and $K$ is the kinetic energy. Kinetic energy can be written as $K = \sum_i |\vec{p_i}|^2/2m_i$, defining a linear momentum $\vec{p}$ for each particle. Making use of momenta, classical equations of motion can be rewritten as a system of coupled ordinary differential equations:

$$\frac{d}{dt}\vec{r_i} = \vec{p_i}/m_i \quad \frac{d}{dt}\vec{p_i} = \vec{f_i}$$

Aim of MD simulations is to generate a **trajectory**, a collection of $\vec{r_i}$ and $\vec{p_i}$ for each particle as functions of time, throughout a numerical integration of the equation of motion.

There are many ways to numerically solve equations of motion. We adopted the so-called “velocity-Verlet” (**md-vv**) method:

$$\begin{aligned}
\vec{p_i}(t + \tfrac{1}{2}\delta t) &= \vec{p_i}(t) + \tfrac{1}{2}\delta t \vec{f_i}(t) \\
\vec{r_i}(t + \delta t) &= \vec{r_i}(t) + \delta t \vec{p_i}(t + \tfrac{1}{2}\delta t)/m_i \\
\vec{p_i}(t + \delta t) &= \vec{p_i}(t + \tfrac{1}{2}\delta t) + \tfrac{1}{2}\delta t \vec{f_i}(t + \delta t)
\end{aligned}$$

where $\delta t$ is the time step of the simulation. The error on position and velocity is $O(\delta t^2)$, which implies an inverse relation between accuracy and time step length.

## B.2 Force Fields

To describe interactions (bonded or non-bonded) between atoms in a simulation, and hence derive forces acting on each particle, a force field is needed. A force field is defined as a set of equations and tunable constants that are used to reproduce molecular geometry and properties in molecular dynamics.

While for preliminar tests GROMOS[126] and CHARMM[127] have been evaluated, GAFF[125] was the Force Field of choice for all simulations in this work, both in water and organic solvents.

The Generalized Amber Force Field is an extension of AMBER force field that applies well to organic molecules. GAFF can assign a particular atom-type to each atom composing the molecular backbone based on characteristic surrounding, taking into account for hybridization and conjugation. The energy between atoms is evaluated taking into account for bond lenghts, angles and dihedral potentials, as well as for Lennard-Jones and Coulombic interactions. All these contributions can be summed up as follows

$$\begin{aligned} E_{\mathrm{GAFF}} = & \sum_{bonds} K_r(r - r_{eq})^2 + \sum_{angles} K_\theta(\theta - \theta_{eq})^2 + \sum_{torsions} \sum_{n=0}^{5} C_n(cos(\psi)^n) \\ & + \sum_{impropers} K_d(1 + cos(n_d\omega - \omega_d)) + \sum_{i>j}^{N} \left[ 4\epsilon_{ij} \left( (\frac{\sigma_{ij}}{r_{ij}})^{12} - (\frac{\sigma_{ij}}{r_{ij}})^{6} \right) + \frac{1}{4\pi\varepsilon_0} \frac{q_i q_j}{r_{ij}} \right] \end{aligned} \tag{B.1}$$

where *bonds*, *angles* and *dihedrals* run on groups of respectively 2,3 and 4 atoms connected through covalent bonds.

## B.3 Ensembles

Each MD system can be described using an ensemble, meant as an infinite set of copies of the system itself, representing all possible arrangement reachable by the real system.

There are various ensembles used to setting up MD simulations that differ by the degree of separation of the system from the surroundings, in other words which variables are kept constant throughout the dynamics. Three of the most commonly used, and the ones used during this essay are:

- Microcanonical (NVE)
- Canonical (NVT)
- Isothermal-isobaric (NPT)

In a **NVE** ensemble the number of molecules ($N$), as well as the volume ($V$) and total energy ($E$), are kept constant. In this kind of ensemble, since total energy is conserved, forces can be calculated as the negative gradient of the potential energy.

The Canonical Ensemble (**NVT**) is similar to the previous one, except that energy can be transfered through system boudaries. The system can be visualized as immersed in a big heat bath, acting as a thermostat. The function of the external thermostat is to add or remove energy from the system, as to reach a target temperature through equilibrium and prevent temperature's drifts. The thermostat used in the dynamics is the modified Berendsen thermostat, also called **V-rescale**. Since in MD simulations temperature is expressed as a function of all particles velocities ($v_{i,\alpha}$), and, using equipartition theorem, can be expressed as:

$$\frac{1}{2}k_bT = \left\langle \frac{mv_{i,\alpha}^2}{2} \right\rangle$$

where $k_b$ is Boltzmann constant, the velocity rescaling algorithm adjusts every velocity in the system, to constraint temperature to a fixed value $T_0$:

$$v'_{i,\alpha} = \sqrt{\frac{T_0}{T}}v_{i,\alpha}$$

In the last ensemble, **NPT**, number of molecules, temperature and pressure are conserved. In addition to the aforementioned thermostat, a barostat is required to control pressure. In our simulations **Parrinello-Rahman** (in water) and **Berendsen isotropic** coupling (in water, chloroform, DMSO and methanol) are adopted. In the Parrinello-Rahman thermostat the volume $V$ is defined as:

$$V = det\hat{B} = \vec{a} \cdot (\vec{b} \times \vec{c})$$

where $\hat{B} = \{\vec{a}, \vec{b}, \vec{c}\}$ is the matrix formed by vectors composing the simulation box. The position $\vec{r}_i$ of each particle can be rewritten using a scaling factor $\vec{s}_i$:

$$\vec{r}_i = \hat{B}\vec{s}_i$$

and following, the squared distance between particle $i$ and $j$ is:

$$r_{ij}^2 = \vec{s}_{ij}^T \hat{G} \vec{s}_{ij} \quad \text{with} \quad \hat{G} = \hat{B}^T \hat{B}$$

In this notation, the equations of motion read:

$$\frac{\partial^2 \vec{s}_i}{\partial t^2} = \frac{\hat{B}^{-1}\vec{f}_i}{m} - \hat{G}^{-1}\frac{\partial \hat{G}}{\partial t}\frac{\partial \vec{s}}{\partial t} \qquad \frac{\partial^2 \hat{B}}{\partial t^2} = \frac{(\hat{P} - P_0\hat{I}_3)V(\hat{H}^{-1})^T}{Q}$$

The simpler Berendsen barostat acts, given a time constant $\tau_p$ and a reference isothermal compressibility $\kappa_T$, as a volume modulator, to mantain pressure close to the reference value $P_0$. The box scaling factor $\mu$ reads (for a cubic box):

$$\mu = 1 - \frac{\kappa_T \Delta t}{3\tau_p}(P_0 - P)$$

## B.4 Enhanced Sampling Techniques

### B.4.1 Umbrella Sampling

The purpose of molecular dynamics simulation is to sample all possible states in which the system of interest may exist. Very often, high potential barriers separates different minima, making it extremely unlikely for a conventional MD simulation to walk through all molecular states and hence explore the whole configurational space. Umbrella sampling (US) is adopted to accelerate the sampling via an artificial *flattening* of the potential surface. This is achieved adding quadratic potentials built to effectively annihilate the real barriers. The sampling of a system is considered complete when, for a chosen variable, its different values are visited several times. The equation for the potential reads:

$$V_{US}(r) = \frac{1}{2}k_{US}(r - r_0) \tag{B.2}$$

where $k_{US}$ is the force constant and $r_0$ is the constant value at which the restraint is applied. A complete free-energy profile is obtained by multiple simulations along different $r_0$ value to cover the entire coordinate subspace. Each simulation provides a biased distribution of $r$. Correct free energy is obtained by unbiasing the potential in Eq.B.2[128]:

$$\tilde{F}(r) = -k_b T ln(N(r) - V_{US}(r) \tag{B.3}$$

where $N(r)$ is the distribution of the visited configurations, $V_{US}(r)$ is the applied bias potential, $k_b$ is the Boltzmann constant and $T$ is the temperature.

At the end, all the unbiased free-energy profiles obtained for different values of $r$ are combined together using weighted histogram analysis method[129] to get the whole free-energy profile.

### B.4.2 Hamiltonian Replica Exchange

Replica exchange involves running constant temperature simulations for a certain number of time steps in parallel on a set of replica systems, each at a different temperature ($T_0$,$T_1$,. . . , $T_N$, where the temperatures are ordered from the lowest to the highest. At the end of this period, an attempt is made to exchange the configurations of a pair of neighboring replicas, and this exchange is accepted with a probability satisfying detailed balance. The process is then repeated. The highest temperature, $T_N$, is chosen so that its replica can rapidly cross the potential energy barriers. Because configurations sampled at the high temperatures can eventually exchange with the low-temperature replicas, the low-temperature systems will experience jumps between potential basins separated by highpoe barriers, something they would not be able to do easily in ordinary room temperature simulations.

## B.5 Simulation conditions

### B.5.1 Chapter 1

**Water**

Simulations in water are performed following the scheme in Table B.1

| Step | Ensemble | Time | Thermostat | Barostat |
|---|---|---|---|---|
| Minimization | - | - | - | - |
| 1 | NVE | 1 ns | - | - |
| 2 | NPT | 1 ns | V-rescale | Parrinello-Rahman |
| 3 | NVT | 10 ns | V-rescale | - |
| 4 | NVT | 100 ns | V-rescale | - |

Table B.1: MD protocol used for the simulations of free NBD and NR in water.

**Minimization** is set with steepest descend algorithm and a maximum force threshold of 400.0 KJ $\mathrm{mol}^{-1}$ $\mathrm{nm}^{-1}$. **NVE**, **NPT** and **NVT** are all performed with **lincs** constraint algorithm where all bond lengths are fixed, with a time step of 1 fs.

**Organic solvents**

Simulations in chloroform and DMSO are performed using pre-equilibrated boxes of plain solvents. The protocol is shown in Table B.2.

| Step | Ensemble | Time | Thermostat | Barostat |
|---|---|---|---|---|
| 1 | NPT | 1 ns | V-rescale | Berendsen |
| 2 | NVT | 10 ns | V-rescale | - |
| 3 | NVT | $>$ 500 ns | V-rescale | - |

Table B.2: MD protocol used for the simulations of free NBD and NR as well as for clx-DA and clx-D*A in chloroform and DMSO.

**NPT** and **NVT** simulations are performed with a 1 fs and 0.5 fs time step respectively. In all simulations **lincs** constraint algorithm with all bond lenght fixed is used.

### B.5.2 Chapter 3

Simulations are performed in plain water following the scheme in Table B.3 **Minimization** is set with steepest descend algorithm and a maximum force threshold of 400.0 KJ mol$^{-1}$ nm$^{-1}$. **NPT** simulations are performed with **lincs** constraint algorithm where all bond lengths are fixed, with a time step of 1 fs.

| **Step** | **Ensemble** | **Time** | **Thermostat** | **Barostat** |
|---:|:---:|:---:|:---:|:---:|
| Minimization | - | - | - | - |
| 1 | NPT | 5 ns | Berendsen | Berendsen |
| 2 | NPT | >100 ns | Berendsen | Berendsen |

Table B.3: MD protocol used for the simulations of DCSB derivatives in water.

### B.5.3 Chapter 4

Simulations are performed in plain methanol and methanol/water mixture in a 60/40 ratio following the scheme in Table B.4 **Minimization** is set with steepest descend algorithm and a maximum force threshold of 400.0 KJ mol$^{-1}$ nm$^{-1}$. **NPT** simulations

| **Step** | **Ensemble** | **Time** | **Thermostat** | **Barostat** |
|---:|:---:|:---:|:---:|:---:|
| Minimization | - | - | - | - |
| 1 | NPT | 5 ns | Berendsen | Berendsen |
| 2 | NPT (hrexMD) | 30 ns | Berendsen | Berendsen |
| 2 | NPT | 50 ns | Berendsen | Berendsen |

Table B.4: MD protocol used for the simulations of ProSQ chiral derivatives in methanol and methanol/water mixture.

are performed with **lincs** constraint algorithm where all bond lengths are fixed, with a time step of 1 fs.

# Acknowledgements

I want to thank all people that supported me during this jurney. I would like to express my gratitude to my thesis supervisor Prof. Anna Painelli. It was a pleasure having such a lively and enthusiastic guide, always present when I needed her prop. I was lucky to join her bright research group, with somebody always well disposed to share knowledge and good advices. It gets hard to thank them all. I believe the presence of so many curious and “excited” scientists had a great impact on the result achieved in this work about “excited” state interactions. A good workplace is essential to achieve something great!

It’s a pleasure to thank all the coworkers who assisted me in this nice tenure: Prof. Francesca Terenziani, Prof. Matteo Masino, Dr. Cristina Sissa, Dr. Francesco Di Maiolo, Brunella, Swathi, Rama and Sangeeth.

I want to thank my family, my mom and dad, that sustained me from the very beginning with their unconditioned love. A special thank goes to my girlfriend, Costanza, my faithful best friend, for putting up with me in the worst of times and for sharing the best moments.

Last but not least, I want to extend my gratitude to two people I had the honor to collaborate with during my stays in Trieste and Zagreb: Ali Hassanali, from ICTP and Luca Grisanti, from IRB. All I know about Molecular Dynamics it is definitely thanks to them.

This project received funding from the European Union Horizon 2020 research and innovation programme under grant agreement no. 812872 (TADFlife), and benefited from the equipment and support of the COMP-HUB Initiative, funded by the “Departments of Excellence” program of the Italian Ministry for Education, University and Research (MIUR, 2018â2022).

We acknowledge the support from the HPC (High Performance Computing) facility of the University of Parma, Italy.

# Bibliography

[1] CA Coulomb. *Premier memoire sur l'electricité et le magnetism Histoire de l'Academie Royale des Sciences*. 1785.

[2] Rodrigo A. Urzúa-Leiva et al. "Thermal Fluctuations on Förster Resonance Energy Transfer in Dyadic Solar Cell Sensitizers: A Combined Ab Initio Molecular Dynamics and TDDFT Investigation." In: *Journal of Physical Chemistry C* 119.29 (2015), pp. 16490–16499.

[3] Fabio Silvestri et al. "Efficient squaraine-based solution processable bulk-heterojunction solar cells." In: *Journal of the American Chemical Society* 130.52 (2008), pp. 17640–17641.

[4] Guodan Wei et al. "Solvent-Annealed crystalline squaraine: PC70BM (1: 6) solar Cells." In: *Advanced Energy Materials* 1.2 (2011), pp. 184–187.

[5] Andrea Zampetti, Alessandro Minotto, and Franco Cacialli. "Near-Infrared (NIR) Organic Light-Emitting Diodes (OLEDs): Challenges and Opportunities." In: *Advanced Functional Materials* 29.21 (2019), p. 1807623.

[6] Jing Huang et al. "Largely blue-shifted emission through minor structural modifications: molecular design, synthesis, aggregation-induced emission and deep-blue OLED application." In: *Chemical Communications* 50.17 (2014), pp. 2136–2138.

[7] Jingjing Guo, Zujin Zhao, and Ben Zhong Tang. "Purely organic materials with aggregation-induced delayed fluorescence for efficient nondoped OLEDs." In: *Advanced Optical Materials* 6.15 (2018), p. 1800264.

[8] Arthur R Grossman et al. “Light-harvesting complexes in oxygenic photosynthesis: diversity, control, and evolution.” In: *Annual review of genetics* 29.1 (1995), pp. 231–288.

[9] Xiaowei Pan et al. “Architecture and function of plant light-harvesting complexes II.” In: *Current opinion in structural biology* 23.4 (2013), pp. 515–525.

[10] Hiroshi Imahori. “Giant multiporphyrin arrays as artificial light-harvesting antennas.” In: *The Journal of Physical Chemistry B* 108.20 (2004), pp. 6130–6143.

[11] Wisnu Tantyo Hadmojo et al. “Artificial light-harvesting n-type porphyrin for panchromatic organic photovoltaic devices.” In: *Chemical science* 8.7 (2017), pp. 5095–5100.

[12] Myung-Seok Choi et al. “Bioinspired molecular design of light-harvesting multiporphyrin arrays.” In: *Angewandte Chemie International Edition* 43.2 (2004), pp. 150–158.

[13] Tomohiro Miyatake et al. “Self-Assembly of Synthetic Zinc Chlorins in Aqueous Microheterogeneous Media to an Artificial Supramolecular Light-Harvesting Device.” In: *Helvetica chimica acta* 82.6 (1999), pp. 797–810.

[14] Nicholas J Hestand et al. “Confirmation of the origins of panchromatic spectra in squaraine thin films targeted for organic photovoltaic devices.” In: *The Journal of Physical Chemistry C* 119.33 (2015), pp. 18964–18974.

[15] Zhengquan Yan et al. “A Convenient Organic–Inorganic Hybrid Approach Toward Highly Stable Squaraine Dyes with Reduced H-Aggregation.” In: *Advanced Functional Materials* 22.2 (2012), pp. 345–352.

[16] Guo Chen et al. “J-aggregation of a squaraine dye and its application in organic photovoltaic cells.” In: *Journal of Materials Chemistry C* 1.40 (2013), pp. 6547–6552.

[17] Th. Förster. “Zwischenmolekulare Energiewanderung und Fluoreszenz.” In: *Ann. Phys.* 1-2 (1948), pp. 55–75.

[18] Kim F. Wong, Biman Bagchi, and Peter J. Rossky. “Distance and Orientation Dependence of Excitation Transfer Rates in Conjugated Systems:â Beyond the Förster Theory.” In: *The Journal of Physical Chemistry A* 108.27 (2004), pp. 5752–5763.

[19] Gregory D. Scholes, Xanthipe J. Jordanides, and Graham R. Fleming. “Adapting the Förster theory of energy transfer for modeling dynamics in aggregated molecular assemblies.” In: *Journal of Physical Chemistry B* 105.8 (2001), pp. 1640–1651.

[20] David Beljonne et al. “Beyond Foörster Resonance Energy Transfer in Biological and Nanoscale Systems Förster Resonance Energy Transfer in Biological and Nanoscale Systems.” In: *Journal of Physical Chemistry B* 113.19 (2009), pp. 6583–6599.

[21] C. Sissa et al. “Beyond the Förster formulation for resonance energy transfer: the role of dark states.” In: *Phys. Chem. Chem. Phys.* 13 (28 2011), pp. 12734–12744.

[22] Brent P. Krueger, Gregory D. Scholes, and Graham R. Fleming. “Calculation of Couplings and Energy-Transfer Pathways between the Pigments of LH2 by the ab Initio Transition Density Cube Method.” In: *The Journal of Physical Chemistry B* 102.27 (1998), pp. 5378–5386.

[23] Alexander A. Voityuk. “Fragment transition density method to calculate electronic coupling for excitation energy transfer.” In: *The Journal of Chemical Physics* ().

[24] Zhi-Qiang You and Chao-Ping Hsu. “Theory and calculation for the electronic coupling in excitation energy transfer.” In: *International Journal of Quantum Chemistry* 114.2 (2014), pp. 102–115.

[25] Lakowicz, J. R. *Principles of Fluorescence Spectroscopy.* Springer US, 1999, p. 698.

[26] Massa J. Shoura et al. “Contribution of fluorophore dynamics and solvation to resonant energy transfer in protein-DNA complexes: A molecular-dynamics study.” In: *Biophysical Journal* 107.3 (2014), pp. 700–710.

[27] S. Calero, S. Lago, and B. Garzón. “Classical molecular dynamics simulation of kappa squared factor in resonance energy transfer for linear dipole models.” In: *Molecular Simulation* 29.8 (2003), pp. 519–525.

[28] Ines Reinartz et al. “Simulation of FRET dyes allows quantitative comparison against experimental data.” In: *Journal of Chemical Physics* 148.12 (2018).

[29] L Stryer, D D Thomas, and C F Meares. “Diffusion-Enhanced Fluorescence Energy Transfer.” In: *Annual Review of Biophysics and Bioengineering* (1982).

[30] Bram Wallace and Paul J. Atzberger. “Förster resonance energy transfer: Role of diffusion of fluorophore orientation and separation in observed shifts of FRET efficiency.” In: *PLOS ONE* ().

[31] F. Di Maiolo and A. Painelli. “Dynamical disorder and resonance energy transfer: a novel quantum-classical approach.” In: *Phys. Chem. Chem. Phys.* 22 (3 2020), pp. 1061–1068.

[32] Martin Hoefling et al. “Structural heterogeneity and quantitative FRET efficiency distributions of polyprolines through a hybrid atomistic simulation and monte carlo approach.” In: *PLoS ONE* 6.5 (2011).

[33] Martin Hoefling and Helmut Grubmüller. “In silico FRET from simulated dye dynamics.” In: *Computer Physics Communications* 184.3 (2013), pp. 841–852.

[34] Irene Tosi et al. “Excitation Dynamics in Hetero-bichromophoric Calixarene Systems.” In: *ChemPhysChem* 17.11 (2016), pp. 1686–1706.

[35] Benôit Roux. “The calculation of the potential of mean force using computer simulations.” In: *Computer physics communications* 91.1-3 (1995), pp. 275–282.

[36] Mulliken, R. S. “Molecular Compounds and their Spectra. II.” In: *J. Am. Chem. Soc.* 74.3 (1952), pp. 811–824.

[37] Soos, Z. G. and Klein, D. J. “Molecular Association: Including Molecular Complexes, Vol. 1.” In: Academic Press, New York, 1975.

[38] Rice, M. J. “Organic Linear Conductors as Systems for the Study of Electron-Phonon Interactions in the Organic Solid State.” In: *Phys. Rev. Lett.* 37 (1 1976), pp. 36–39.

[39] Painelli, A. and Girlando,A. “Electron-molecular vibration (e-mv) coupling in charge-transfer compounds and its consequences on the optical spectra: A theoretical framework.” In: *J. Chem. Phys.* 84.10 (1986), pp. 5655–5671.

[40] Del Freo, L. and Painelli, A. and Soos, Z. G. “Giant Infrared Intensity of the Peierls Mode at the Neutral-Ionic Phase Transition.” In: *Phys. Rev. Lett.* 89 (2 2002), p. 027402.

[41] D’Avino, G. and Masino, M. and Girlando, A. and Painelli, A. “Correlated electrons in soft lattices: Raman scattering evidence of the nonequilibrium dielectric divergence at the neutral-ionic phase transition.” In: *Phys. Rev. B* 83 (16 2011), p. 161105.

[42] Scholes, G. D. “Long-Range Resonance Energy Transfer In Molecular Systems.” In: *Annu. Rev. Phys. Chem.* 54.1 (2003), pp. 57–87.

[43] Di Maiolo, F. and Painelli, A. “Intermolecular Energy Transfer in Real Time.” In: *J. Chem. Theory Comput.* 14.10 (2018), pp. 5339–5349.

[44] Mattia Anzola et al. “Understanding Förster Energy Transfer through the Lens of Molecular Dynamics.” In: *Journal of Chemical Theory and Computation* 16.12 (2020), pp. 7281–7288.

[45] Knoester, J. “Optical properties of molecular aggregates.” In: *Organic Nanostructures: Science and applications.* Ed. by G. C. La Rocca V. M. Agranovich. Vol. 149. Amsterdam: IOS Press, 2002, pp. 149–186.

[46] Spano, F. C. “The Spectral Signatures of Frenkel Polarons in H- and J-Aggregates.” In: *Acc. Chem. Res.* 43.3 (2010), pp. 429–439.

[47] Hestand, N. J. and Spano, F. C. “Expanded Theory of H- and J-Molecular Aggregates: The Effects of Vibronic Coupling and Intermolecular Charge Transfer.” In: *Chem. Rev.* 118 (2018), pp. 7069–7163.

[48] Craig, D. P. and Walmsley, S. H. *Excitons in Molecular Crystals.* Benjamin, 1968.

[49] Davidov, A. S. *Theory of Molecular Excitons.* Plenum Press, 1971.

[50] Agranovich, V. M. and Galanin, M. D. *Excitons in Molecular Crystals.* North-Holland, 1982.

[51] Jelley, E. E. “Absorption and Fluorescence Spectra of Dyes in the molecular state.” In: *Nature* 138 (1936), pp. 1009–1010.

[52] Kasha, M. “Energy Transfer Mechanism and the Molecular Exciton Model for Molecular Aggregates.” In: *Radiat. Res.* 3 (1964), pp. 317–331.

[53] Terenziani, F. and Painelli, A. “Supramolecular interactions in clusters of polar and polarizable molecules.” In: *Phys. Rev. B* 68 (16 2003), p. 165405.

[54] Terenziani, F. and D’Avino, G. and Painelli A. “Multichromophores for Nonlinear Optics: Designing the Material Properties by Electrostatic Interactions.” In: *ChemPhysChem* 8 (2007), pp. 2433–2444.

[55] Sanyal, S. and Sissa, C. and Terenziani, F. and Pati, S. K. and Painelli, A. “Superlinear amplification of the first hyperpolarizability of linear aggregates of DANS molecules.” In: *Phys. Chem. Chem. Phys.* 19 (36 2017), pp. 24979–24984.

[56] D’Avino, G. and Terenziani, F. and Painelli, A. “Aggregates of Quadrupolar Dyes: Giant Two-Photon Absorption from Biexciton States.” In: *ChemPhysChem* 8 (2007), pp. 2433–2444.

[57] Sanyal, S. and Painelli, A. and Pati, S. K. and Terenziani, F. and Sissa, C. “Aggregates of quadrupolar dyes for two-photon absorption: the role of intermolecular interactions.” In: *Phys. Chem. Chem. Phys.* 18 (40 2016), pp. 28198–28208.

[58] Bardi, B. and Dall'Agnese, C. and Tassé, M. and Ladeira, S. and Painelli, A. and Moineau-Chane Ching,K. I. and Terenziani, F. "Multistimuli Responsive Materials from Benzothiadiazole Based Charge Transfer Chromophores: Interdependence of Optical Properties and Aggregation." In: *ChemPhotoChem* 2 (2018), pp. 1027–1037.

[59] Zheng, C. and Zhong, C. and Collison, C. J. and Spano, F. C. "Non-Kasha Behavior in Quadrupolar Dye Aggregates: The Red-Shifted H-Aggregate." In: *J. Phys. Chem. C* 123 (2019), pp. 3203–3215.

[60] Paganelli, S. and Ciuchi, S. "Tunnelling system coupled to a harmonic oscillator: an analytical treatment." In: *J. Phys. Condens. Matter* 18 (2006), pp. 7669–7685.

[61] Paganelli, S. and Ciuchi, S. "Charge transfer and coherence dynamics of a tunnelling system coupled to an harmonic oscillator." In: *J. Phys. Condens. Matter* 20 (2008), p. 235203.

[62] Anna Painelli and Francesca Terenziani. "Multielectron Transfer in Clusters of Polar-Polarizable Chromophores." In: *Journal of the American Chemical Society* 125.19 (2003), pp. 5624–5625.

[63] Barbara Panunzi et al. "A new donor-acceptor crosslinkable l-shape chromophore for NLO applications." In: *Journal of Molecular Structure* 1189 (2019), pp. 21–27.

[64] Mykola Kondratenko, Andrey G Moiseev, and Dmitrii F Perepichka. "New stable donor–acceptor dyads for molecular electronics." In: *Journal of Materials Chemistry* 21.5 (2011), pp. 1470–1478.

[65] Barry P Rand et al. "Mixed donor-acceptor molecular heterojunctions for photovoltaic applications. I. Material properties." In: *Journal of Applied Physics* 98.12 (2005), p. 124902.

[66] Chuwei Zhong, David Bialas, and Frank C. Spano. "Unusual Non-Kasha Photophysical Behavior of Aggregates of Push-Pull Donor-Acceptor Chromophores." In: *The Journal of Physical Chemistry C* 124.3 (2020), pp. 2146–2159.

[67] A. Girlando and A. Painelli. “Regular-dimerized stack and neutral-ionic interfaces in mixed-stack organic charge-transfer crystals.” In: *Physical Review B* 34.4 (1986), pp. 2131–2139.

[68] Painelli, A. “Vibronic contribution to static NLO properties: exact results for the DA dimer.” In: *Chemical Physics Letters* 285.5 (1998), pp. 352–358.

[69] Francesca Terenziani and Anna Painelli. “Supramolecular interactions in clusters of polar and polarizable molecules.” In: *Physical Review B* 68.16 (2003), p. 165405.

[70] Agranovich, V. M. and Toshich, B. S. “Collective Properties Of Frenkel Excitons.” In: *Soviet Physics JETP* 26.1 (1968), pp. 149–162.

[71] Zoltán G Soos and Anna Painelli. “Metastable domains and potential energy surfaces in organic charge-transfer salts with neutral-ionic phase transitions.” In: *Physical Review B* 75.15 (2007), p. 155119.

[72] Gabriele D’Avino et al. “Bistability in Fc-PTM Crystals: The Role of Intermolecular Electrostatic Interactions.” In: *Journal of the American Chemical Society* 130.36 (2008), pp. 12064–12072.

[73] Gabriele D’Avino et al. “Cooperativity from electrostatic interactions: understanding bistability in molecular crystals.” In: *CrystEngComm* 11.10 (2009), pp. 2040–2047.

[74] Anna Painelli and Francesca Terenziani. “A non-perturbative approach to solvatochromic shifts of push–pull chromophores.” In: *Chemical physics letters* 312.2-4 (1999), pp. 211–220.

[75] M. Anzola, F. Di Maiolo, and A. Painelli. “Optical spectra of molecular aggregates and crystals: testing approximation schemes.” In: *Physical Chemistry Chemical Physics* 21.36 (2019), pp. 19816–19824.

[76] Sissa, C. and Painelli, A. and Blanchard-Desce, M. and Terenziani, F. “Fluorescence Anisotropy Spectra Disclose the Role of Disorder in Optical Spectra of Branched Intramolecular-Charge-Transfer Molecules.” In: *J. Phys. Chem. B* 115 (2011), pp. 7009–7020.

[77] Judith Guasch et al. “Bistability of Fc-PTM-Based Dyads: The Role of the Donor Strength.” In: *Chemistry of Materials* 25.5 (2013), pp. 808–814.

[78] Painelli, A. and Terenziani, F. “Optical Spectra of Push-Pull Chromophores in Solution: A Simple Model.” In: *The Journal of Physical Chemistry A* 104.47 (2000), pp. 11041–11048.

[79] Boldrini, B. and Cavalli, E. and Painelli, A. and Terenziani, F. “Polar Dyes in Solution: A Joint Experimental and Theoretical Study of Absorption and Emission Band Shapes.” In: *The Journal of Physical Chemistry A* 106.26 (2002), pp. 6286–6294.

[80] Terenziani, F. and D’Avino, G. and Painelli A. “Multichromophores for Nonlinear Optics: Designing the Material Properties by Electrostatic Interactions.” In: *ChemPhysChem* 8 (2007), pp. 2433–2444.

[81] Terenziani, F. and Painelli, A. and Girlando, A. and Metzger, R. M. “From Solution to LangmuirâBlodgett Films:â Spectroscopic Study of a Zwitterionic Dye.” In: *The Journal of Physical Chemistry B* 108.30 (2004), pp. 10743–10750.

[82] K Swathi et al. “Supramolecular chirality: a caveat in assigning the handedness of chiral aggregates.” In: *Chemical Communications* 56.59 (2020), pp. 8281–8284.

[83] Philpott, M. R. “Theory of the Coupling of Electronic and Vibrational Excitations in Molecular Crystals and Helical Polymers.” In: *J. Chem. Phys.* 55.5 (1971), pp. 2039–2054.

[84] Hoffmann, M. and Soos, Z. G. “Optical absorption spectra of the Holstein molecular crystal for weak and intermediate electronic coupling.” In: *Phys. Rev. B* 66 (2 2002), p. 024305.

[85] Paulius Baronas et al. “Enhanced Energy Transfer in Doped Bifluorene Single Crystals: Prospects for Organic Lasers.” In: *Advanced Optical Materials* 8.4 (2020), p. 1901670.

[86] William Moffitt. “Optical rotatory dispersion of helical polymers.” In: *The Journal of Chemical Physics* 25.3 (1956), pp. 467–478.

[87] William Moffitt and Jen Tsi Yang. “The optical rotatory dispersion of simple polypeptides. I.” In: *Proceedings of the National Academy of Sciences of the United States of America* 42.9 (1956), p. 596.

[88] Jen Tsi Yang, Chuen-Shang C Wu, and Hugo M Martinez. “[11] Calculation of protein conformation from circular dichroism.” In: *Methods in enzymology* 130 (1986), pp. 208–269.

[89] Sharon M Kelly and Nicholas C Price. “The use of circular dichroism in the investigation of protein structure and function.” In: *Current protein and peptide science* 1.4 (2000), pp. 349–384.

[90] Molecular Quantum Electrodynamics. *An Introduction to Radiation Molecule Interactions.* 1998.

[91] E. U. Condon. “Theories of Optical Rotatory Power.” In: *Reviews of Modern Physics* 9.4 (1937), pp. 432–457.

[92] Albert Moscowitz. “Theoretical aspects of optical activity part one: small molecules.” In: *Advances in Chemical Physics* 4 (1962), pp. 67–112.

[93] Jürgen Kästel et al. “Tunable negative refraction without absorption via electromagnetically induced chirality.” In: *Physical review letters* 99.7 (2007), p. 073602.

[94] AN Bogdanov and UK Rößler. “Chiral symmetry breaking in magnetic thin films and multilayers.” In: *Physical review letters* 87.3 (2001), p. 037203.

[95] Alexandre Martinez, Laure Guy, and Jean-Pierre Dutasta. “Reversible, solvent-induced chirality switch in atrane structure: control of the unidirectional motion

of the molecular propeller." In: *Journal of the American Chemical Society* 132.47 (2010), pp. 16733–16734.

[96] Iris Destoop et al. "Solvent-induced homochirality in surface-confined low-density nanoporous molecular networks." In: *Journal of the American Chemical Society* 134.48 (2012), pp. 19568–19571.

[97] Yin Zhao et al. "Supramolecular chirality in achiral polyfluorene: chiral gelation, memory of chirality, and chiral sensing property." In: *Macromolecules* 49.9 (2016), pp. 3214–3221.

[98] Miguel A Mateos-Timoneda, Mercedes Crego-Calama, and David N Reinhoudt. "Supramolecular chirality of self-assembled systems in solution." In: *Chemical Society Reviews* 33.6 (2004), pp. 363–372.

[99] Seong-Jun Yoon et al. "Multistimuli two-color luminescence switching via different slip-stacking of highly fluorescent molecular sheets." In: *Journal of the American Chemical Society* 132.39 (2010), pp. 13675–13683.

[100] Shinto Varghese et al. "Orthogonal Resonator Modes and Low Lasing Threshold in Highly Emissive Distyrylbenzene-Based Molecular Crystals." In: *Advanced Optical Materials* 2.6 (2014), pp. 542–548.

[101] Shinto Varghese et al. "Polymorphism and Amplified Spontaneous Emission in a Dicyano-Distyrylbenzene Derivative with Multiple Trifluoromethyl Substituents: Intermolecular Interactions in Play." In: *Advanced Functional Materials* 26.14 (2016), pp. 2349–2356.

[102] Nobuyuki Harada, Motoaki Ohashi, and Koji Nakanishi. "The benzoate sector rule, a method for determining the absolute configurations of cyclic secondary alcohols." In: *Journal of the American Chemical Society* 90.26 (1968), pp. 7349–7351.

[103] Nobuyuki Harada, Sow-Mei Lai Chen, and Koji Nakanishi. "Quantitative definition of exciton chirality and the distant effect in the exciton chirality method." In: *Journal of the American Chemical Society* 97.19 (1975), pp. 5345–5352.

[104] Prasad L Polavarapu. *Chiroptical spectroscopy: fundamentals and applications.* Crc Press, 2016.

[105] M. J. Frisch et al. *GaussianË16 Revision C.01.* Gaussian Inc. Wallingford CT. 2016.

[106] J Wang et al. “Automatic atom type and bond type perception in molecular mechanical calculations.” In: *Journal of Molecular Graphics and Modelling* 25 (2006), p. 247260.

[107] J Wang et al. “Development and testing of a general AMBER force field.” In: *Journal of Computational Chemistry* 25 (2004), pp. 1157–1174.

[108] Rachel Crespo-Otero, Quansong Li, and Lluis Blancafort. “Exploring Potential Energy Surfaces for Aggregation-Induced EmissionâFrom Solution to Crystal.” In: *Chemistry–An Asian Journal* 14.6 (2019), pp. 700–714.

[109] Cheng Chen et al. “A squaraine-based colorimetric and âturn onâ fluorescent sensor for selective detection of Hg2+ in an aqueous medium.” In: *Organic letters* 13.5 (2011), pp. 1162–1165.

[110] Brian T Makowski et al. “A melt-processable squaraine-based organic glass for nonlinear optics.” In: *Journal of Materials Chemistry* 22.7 (2012), pp. 2848–2850.

[111] Matthias Schulz et al. “Giant intrinsic circular dichroism of prolinol-derived squaraine thin films.” In: *Nature communications* 9.1 (2018), pp. 1–10.

[112] Kuthanapillil Jyothish, Mahesh Hariharan, and Danaboyina Ramaiah. “Chiral supramolecular assemblies of a squaraine dye in solution and thin films: Concentration-, temperature-, and solvent-induced chirality inversion.” In: *Chemistry–A European Journal* 13.20 (2007), pp. 5944–5951.

[113] Kaja C Deing et al. “Aggregation-dependent photovoltaic properties of squaraine/PC 61 BM bulk heterojunctions.” In: *Physical Chemistry Chemical Physics* 14.23 (2012), pp. 8328–8334.

[114] Matthias Schulz et al. “Organic photodiodes from homochiral L-proline derived squaraine compounds with strong circular dichroism.” In: *Physical Chemistry Chemical Physics* 19.10 (2017), pp. 6996–7008.

[115] Ragnar S Stoll et al. “Synthesis of a Novel Chiral Squaraine Dye and Its Unique Aggregation Behavior in Solution and in Self-Assembled Monolayers.” In: *Advanced Materials* 18.10 (2006), pp. 1271–1275.

[116] Francesca Terenziani et al. “Charge instability in quadrupolar chromophores: Symmetry breaking and solvatochromism.” In: *Journal of the American Chemical Society* 128.49 (2006), pp. 15742–15755.

[117] Francesca Terenziani et al. “Charge instability in quadrupolar chromophores: Symmetry breaking and solvatochromism.” In: *Journal of the American Chemical Society* 128.49 (2006), pp. 15742–15755.

[118] D’Avino, G. and Terenziani, F. and Painelli, A. “Aggregates of Quadrupolar Dyes: Giant Two-Photon Absorption from Biexciton States.” In: 8 (2007), pp. 2433–2444.

[119] Cristina Sissa et al. “Dimers of Quadrupolar Chromophores in Solution: Electrostatic Interactions and Optical Spectra.” In: *The Journal of Physical Chemistry B* 114.2 (2010), pp. 882–893.

[120] S Sanyal et al. “Aggregates of quadrupolar dyes for two-photon absorption: the role of intermolecular interactions.” In: *Physical Chemistry Chemical Physics* 18.40 (2016), pp. 28198–28208.

[121] B. Bardi et al. “Spectroscopic Investigation and Theoretical Modeling of Benzothiadiazole-Based Charge-Transfer Chromophores: From Solution to Nanoaggregates.” In: *J. Phys. Chem. C* 121 (2017), pp. 17466–17478.

[122] Chenyu Zheng et al. “Non-kasha behavior in quadrupolar dye aggregates: The red-shifted h-aggregate.” In: *The Journal of Physical Chemistry C* 123.5 (2019), pp. 3203–3215.

[123] Alberto Girlando and Anna Painelli. “Regular-dimerized stack vs neutral-ionic instability in mixed stack CT crystals.” In: *Physica B+ C* 143.1-3 (1986), pp. 559–561.

[124] S Ramasesha and Z Soos. *Valence bond theory (ed.) DL Cooper*. 2002.

[125] Junmei Wang et al. “Development and testing of a general amber force field.” In: *Journal of Computational Chemistry* 25.9 (2004), pp. 1157–1174.

[126] Nathan Schmid et al. “Definition and testing of the GROMOS force-field versions 54A7 and 54B7.” In: *European biophysics journal* 40.7 (2011), pp. 843–856.

[127] Bernard R Brooks et al. “CHARMM: a program for macromolecular energy, minimization, and dynamics calculations.” In: *Journal of computational chemistry* 4.2 (1983), pp. 187–217.

[128] Massimiliano Bonomi, Alessandro Barducci, and Michele Parrinello. “Reconstructing the equilibrium Boltzmann distribution from well-tempered metadynamics.” In: *Journal of computational chemistry* 30.11 (2009), pp. 1615–1621.

[129] Shankar Kumar et al. “The weighted histogram analysis method for free-energy calculations on biomolecules. I. The method.” In: *Journal of computational chemistry* 13.8 (1992), pp. 1011–1021.

# List of Publications

M. Anzola, C. Sissa, A. Painelli, A. Hassanali, L. Grisanti *Optical spectra of molecular aggregates and crystals: testing approximation schemes*, Physical Chemistry Chemical Physics, 21 (2019) 19816–19824

M. Anzola, F. Di Maiolo, A. Painelli, *Understanding Förster Energy Transfer through the Lens of Molecular Dynamics*, Journal of Chemical Theory and Computation, 16 (2020) 7281-7288